Grand Valley State University
ScholarWorks@GVSU

12-2018

The Design, Analysis, Development, and Test of a High-Energy Trauma Prevention Safety Device

Samuel B. Schaefer
Grand Valley State University

Follow this and additional works at: https://scholarworks.gvsu.edu/theses

Part of the Engineering Commons

Recommended Citation

The Design, Analysis, Development, and Test of a High-Energy Trauma Prevention Safety Device

Samuel Brooks Schaefer

A Thesis Submitted to the Graduate Faculty of

Grand Valley State University

in

Partial Fulfillment of the Requirements

For the Degree of

Master of Science in Engineering

School of Engineering

December 2018

Acknowledgments

Special thanks are in order for my entire thesis committee. Their support and patience were invaluable to the completion of this thesis. In particular, Dr. Brent Nowak for his inspiration, guidance, and understanding throughout the entirety of this work, Dr. Blake Ashby for his comprehensive knowledge of impact biomechanics, and Dr. Wendy Reffeor for her extensive experience with material science. I would also like to thank Packaging Compliance Labs for providing their facility during the experimental testing process and Midway Machining for their assistance during prototype fabrication.

Abstract

The continued development of modern-day vehicles has allowed innovators to shape their design to meet the consumer's requirements. Vehicles have become faster and larger to accommodate more passengers and their belongings. The increased popularity of Light Trucks or Vans (LTVs) and Sports Utility Vehicles (SUVs) elevated their sales to approximately 50% of all vehicles sold in the United States by 1999 [1]. These advancements have created a high-energy world, which poses a serious threat to the ever-growing population. Unprotected pedestrians come in all too frequent contact with these vehicles creating the potential for high-energy blunt force trauma. This thesis aims to prevent the deadly result of pedestrians suffering LTV impact from the rear through the design, analysis, development, and test of a protective wearable device. The metrics of evaluation of the impact scenario were average acceleration and spinal hyperextension.

This work employed analytical analysis, finite element analysis, and experimental testing methods to develop the device. Elements of the design and its association with advanced materials gave the proposed device novelty. Experimental testing was accomplished through a drop test series using a mock human model. Full height testing simulated a vehicular collision at 20 miles per hour. Data were collected through acceleration measurements and high-speed video analysis. Statistical analysis of the impacting event showed an appreciable decrease in acceleration and a significant reduction in dynamic hyperextension. The average acceleration during initial impact was decreased by 14% and hyperextension was reduced by 81%.

The resulting peak acceleration surpassed the NHTSA's Thoracic Injury Criteria (TIC) criteria of 60 G's but not the suggested Thoracic Trauma Index (TTI) level of 85 G's [2] [3]. These criteria are identified as exceeding the set level for a time interval longer than 3 ms. Reducing peak acceleration to within these limits was found in literature to reduce the probability of severe internal damage [3]. The significant decrease in hyperextension reduced the deflection to an acceptable range of the human spine and would prevent the pedestrian's head from impacting the hood of the vehicle. These results combined with an ergonomic functional design supports the proposed device as a feasible and capable protective measure against high-energy blunt force trauma.

Table of Contents

List of Figures

11

List of Tables

List of Appendix Tables

List of Abbreviations

LTV   Light Truck or Van

SUV   Sports Utility Vehicle

NHTSA   National Highway Traffic Safety Administration

AIS   Abbreviated Injury Scale

TIC   Thoracic Injury Criteria

TTI   Thoracic Trauma Index

PCDS   Pedestrian Crash Data Study

CDS   Crashworthiness Data System

NASS   National Automotive Sampling System

THUMS   Total Human Model for Safety

HUMOS   Human Model for Safety

GHBMC   Global Human Body Models Consortium

MADYMO   Mathematical Dynamic Model

FEA   Finite Element Analysis

EVA   Ethylene Vinyl Acetate

STF   Shear Thickening Fluid

CAD   Computer-aided Design

CNC   Computer Numerical Control

GVSU   Grand Valley State University

ANSI   American National Standards Institute

1 Introduction

1.1 Introduction/Background

Ever since the development of the first car, innovators have driven to make vehicles faster and more appealing to the consumer. Vehicles have become larger to accommodate more passengers and their belongings. The increased popularity of Light Trucks or Vans (LTVs) and Sports Utility Vehicles (SUVs) elevated their sales to approximately 50% of all vehicles sold in the United States by 1999 [1]. The growing number of LTVs on the road provides the opportunity for deadly collisions with unprotected people traveling by other means of transportation. Technological advancements introduce people to situations that can result in high-energy trauma. In these scenarios, it is vital to protect the human body from severe injury and even death. One prominent situation that requires the protection of the body in today's high-energy world is a vehicular collision.

Vehicle collisions are responsible for high-energy blunt force trauma. The danger to passengers has been well documented, and companies continue to improve interior safety methods. Unfortunately, bicyclists and pedestrians are exposed and have minimal protective safety equipment during a vehicular collision. For bicyclists, the standard safety equipment includes a foam-lined helmet and knee or elbow pads. Several other devices have been developed but are not as widely utilized or enforced. These products include airbag helmets, airbag jackets or vests, and impact absorbing protective armor [12] [13] [14]. Companies have also begun developing exterior airbags for smaller passenger cars and implementing pedestrian collision sensors on a wide range of vehicles [15]. These advancements are only the beginning

of extensive research and development. Immediate innovation is required to protect the human body from the increasing number of vehicle-to-person collisions.

A 19% increase of pedalcyclist fatalities between 2010 and 2013 in the United States was a clear indication of an opportunity for improvement in pedalcyclist safety equipment [16]. A pedalcyclist is defined, by the National Highway Traffic Safety Administration (NHTSA), as any non-motorized vehicle consisting of one, two, or three wheels powered solely by pedals [16]. In 2013, 743 pedalcyclists were killed and approximately 48,000 others injured in motor vehicle accidents [16]. Pedalcyclist fatalities and injuries accounted for 2% of total motor vehicle traffic deaths and 2% of all traffic collision injuries [16]. In that same year, vehicle-to-pedestrian collisions accounted for 14% of total traffic fatalities and 3% of all traffic collision injuries [17]. The number of pedestrians killed and injured reached 4,735 and approximately 66,000, respectively [17]. The larger quantity of fatalities and injuries to pedestrians, compared to pedalcyclists, can be hypothesized to be directly related to a larger number of pedestrians on the road and the observation that pedestrians do not wear any protective equipment. However, the lack of protective gear was not the only variable directly related to severe injury.

Although small cars can cause serious injuries at high speeds, the probability of severe injury is lower at speeds under 15 miles per hour [18]. Cars tend to cause immediate damage to a pedestrian's legs because the bumper and hood are so low to the ground. On the other hand, larger vehicles, LTVs, are higher off the ground and have a higher probability of causing severe injury at speeds below 15 miles per hour [18]. Approximating the height of a light truck's hood at 48 inches from the ground, it will strike the 50th percentile male above their center of mass. The center of mass was calculated to be 38 inches from the ground using anthropometric data

for a 50th percentile male [5], see Appendix A. This type of collision created a direct impact with the pedestrian's lower and middle torso increasing the probability of a severe injury. In fact, in 2004 an evaluation of pedestrian crash cases collected by the Pedestrian Crash Data Study from 1994 to 1998 revealed that pedestrians are three times more likely to receive severe injuries when struck by a light truck than by a small car [19]. The identification of a severe injury is widely accepted as a level 4 on the Abbreviated Injury Scale (AIS), which applies the type of injury and its relative severity to a value between 0 and 9. An injury of AIS4 is described as the probability of death being between 5% and 50%. The increased probability of severe injury highlights a significant need that this research aimed to address.

This master's thesis focused on a wearable back protecting device to prevent injury during an LTV-to-pedestrian impact. This first work included the design, analysis, fabrication, and testing to support the developed concept. The resulting device is projected to be applicable to a wide range of uses. Other applications may include pedalcyclists, athletes, extreme sport enthusiasts, and military personnel. Although cyclists are more inclined to use protective equipment, the literature on vehicle-to-cyclist collisions are not comprehensive and the complexity of the impact dynamics exceeded the scope of this research. It is hoped that the development of this device will encourage future research into the aforementioned applications.

Relevant vehicle-to-bicyclist literature was only included to support the danger of larger vehicles to unprotected persons. Research revealed that for both types of collisions injuries inflicted upon a pedestrian or cyclist were due to a multitude of variables. These included but were not limited to the direction of impact, vehicle body type and mass, height and mass of the

20

person, and the relative velocity between the vehicle and person. These selected variables were the foundation of the impact scenario discussed in this work.

1.2 Technical Problem

Research and development have concentrated on a pedestrian being struck from behind by a light truck traveling at 20 mph. At this velocity the risk of severe injury, or AIS4, was approximately 25% [20]. Twenty miles per hour was selected because the resulting average acceleration exceeded the NHTSA's critical chest acceleration limit of 60 G's for the Thoracic Injury Criteria (TIC), which identifies the probability of serious injury (AIS3) or higher to be 85% [2]. Additional research identified the Thoracic Trauma Index (TTI) for pedestrians, which specified a tolerance level of 85 G's before severe injury is likely to occur [3]. This level was not to be exceeded for longer than 3 ms.

The LTV vehicle type and the direction of impact were selected because they result in a higher risk of severe injury at a lower speed [21] [22]. The direction of impact was assumed to apply a normal force to the pedestrian's back. It was deduced from published literature that the risk of a rear impact originated from direct contact with the patient's spine and the absence of time for a pedestrian to react to the oncoming vehicle. Initial impact by the LTV projected the person's body forward. The upper portion of his or her body, which was not contacted by the vehicle, began to arch backwards over the hood hyperextending the spine. In some cases, the person's head struck the hood of the vehicle [3]. The impact force by a vehicle traveling at 20 miles per hour can exceed 10,000 pounds distributed over a person's body, as calculated in Appendix B. As will be discussed, this applied force has the potential to severely injure a person's upper body in several ways.

Direct contact with a person's torso generates accelerated compression and therefore internal cavitation [23]. This cavitation has the potential to cause tissue and organ damage leading to internal bleeding [23]. Impact forces applied directly to the spine of this magnitude can be great enough to create vertebrae fractures [24]. In the event a person's head strikes the hood, there is a documented high probability of severe head trauma and possibility of death [22]. The lack of protective equipment leaves humans vulnerable to these types of severe injuries and many others.

It is proposed that a non-Newtonian impact absorbing material in combination with a biomimetic structure could protect pedestrians subject to a forward projecting collision with a large vehicle approaching from the rear. A device designed to endure a collision from the posterior to anterior direction of a pedestrian's spine relies heavily on its material properties. The materials must withstand the extremely high impact forces and attenuate the transmitted load. Additionally, the device must not be overly restrictive of the user's range of motion nor add excessive weight.

1.3 Assumptions

The pedestrian was assumed to be a 50th percentile male, which signifies the average of the male population. The 50th percentile male was a common assumption used by the NHTSA and researchers in this field. In general, physical testing was found to be conducted using the Hybrid III 50th percentile male crash test dummy. This model was comprised of segment weights and lengths to mimic a pedestrian. The limited available resources during this research required a human model to be improvised for experimental testing by utilized an 80 lb professional punching bag. During concept development, anthropometric data for the 50th percentile male

was used to calculate the body center of mass and impact forces applied to the lumbar and thoracic regions. For this work, the worst-case scenario was defined as a pedestrian standing motionless and facing away from the vehicle. This was justified as the spinal damage was maximized in this scenario.

The vehicle was a light truck moving at 20 mph, relative to the pedestrian, with a hood height of 48 inches. The weight of the vehicle was not considered because it was significantly larger than the pedestrian, supported by Mizuno and Kajzer whom identified the geometry of the vehicle as more significant [18] [19]. Additionally, the large mass difference meant impact with the pedestrian did not have any effect on the speed of the vehicle

As part of the worst-case scenario, no braking was assumed to have occurred before the impact. Consequently, the light truck struck the pedestrian at a peak velocity of 20 mph. This initial impact was assumed to cause the greatest amount of damage to the person and was the focus of this first work. Secondary impacts with the vehicle or the ground were beyond the scope of research. The impact time, for the pedestrian to reach 20 mph, was approximated as 15 milliseconds. The impact time did not include the pedestrian's rebound due to high variability. The impact interval was deduced from a 2012 study validating the use of a full body finite element model under lateral impact loading, which recorded similar impact times at similar speeds as compared to experimental cadaver testing [25].

A theoretical change in velocity of the pedestrian after collision was calculated to be approximately 24 mph, assuming their initial velocity was zero. This resulting velocity was calculated using a coefficient of restitution of 0.2 for the human body, see Appendix B for

calculations. This assumed restitution coefficient was also supported by the previously

mentioned full body modeling study. The full body model traveling at 20 mph rebounded at 3.8

mph resulting in a change in velocity of 23.8 mph [25]. The coefficient of restitution for the

total body was then calculated by the author to be 0.19, see in Appendix B. With a difference of

5% from the assumed value, the literature supported a coefficient of restitution equal to 0.2. A

larger coefficient also provided a worst-case scenario for the basis for product development.

2 Review of Literature

A review of previous studies was conducted to further understand the issue of vehicle-to-bicyclist and vehicle-to-pedestrian collisions. The focus during research was on collisions occurring with the pedestrian or cyclist facing away from the vehicle. Studies focusing on this direction of impact were fewer than lateral impact because the approach angle occurred less frequently. For this reason, it was necessary to include studies on lateral impacting to further understand characteristics of the pedestrians at risk of vehicular collisions.

2.1 Collision and Impact Biomechanics Studies

The most extensive study on vehicle-to-bicyclist collisions was conducted using data collected from 1990 to 1999 in Great Britain. The database consisted of over 30,000 standardized reports of one cyclist and one vehicle collisions that resulted in death or severe injury. It was recognized that Great Britain's vehicle type distribution differs from the United States, but the vehicle type was not discussed in this study. The evaluation of the data was represented by accident incidence rates and their associated fatality rates. The notable statistics were gender, age, speed limit, and first point of impact on the bicycle. The results are tabulated below [21].

Table 1: Reported statistics for vehicle-to-bicycle collisions [21].

		Accident Incidence Rates (%)	Associated Fatality Rates (%)
Gender	Male	80.8	5.0
	Female	19.2	4.3
Age	0-9	9.7	3.0
	10-19	32.7	3.6
	20-29	18.6	3.4
	30-39	13.3	4.5
	40-49	9.1	5.3
	50-59	7.1	8.2
	60-69	4.5	10.8
	70-79	2.8	14.6
	80-89	0.9	19.1
	90+	0.1	-
Speed Limit (mph)	30	76.0	3.0
	40	8.2	6.4
	50	0.9	13.0
	60	11.9	11.2
	70	2.8	19.6
Bicycle Impact	Front	52.1	2.9
	Back	13.7	10.0
	Right	19.1	7.0
	Left	11.2	4.4

The reported number of males in a severe accident was four times greater than women. Associated fatality rates for men and women were 5% and 4.3%, respectively. From the age distribution, it was evident that most incidences occurred with riders between the ages of 10 and 39 years and the risk of fatality increased with age. Accidents cross referenced with posted speed limits showed the majority occurring at a lower speed but a fatality rate that increased with velocity. This was observed across many studies and commonly referred to as the only constant and non-controversial parameter in collision analysis [26].

The posted speeds were much higher than those observed in vehicle-to-pedestrian collisions but still applicable to this research because of relative velocity. The average bicyclist was assumed to travel on level ground between 10 and 20 mph. If struck from behind by a vehicle traveling at 30 mph, the relative velocity between the two objects is between 10 mph and 20 mph. Although statistics showed the area of first impact on the bicycle was heavily weighted toward the front, the fatality rate revealed the ultimate danger of a bicyclist was in being rear ended. Of the collected data, only 3% of the front collisions resulted in a fatality while rear impacts reached 10%. These results support the choice in this study to model rear impacts with a relative speed of 20 mph.

In the United States, the NHTSA also recorded bicyclist injuries and fatalities but with less detail [16]. In 2013 there were 743 deaths and approximately 48,000 injuries inflicted on bicyclists from motor vehicle collisions [16]. Men accounted for 83% of the injured and 87% of those killed [16]. The high percentage of males involved in bicycle accidents supports the findings from the previous study in Great Britain and supports the choice to model a device for use by a 50th percentile male in the current study. The associated fatality rate for males and females was calculated to be 1.5% and 1.2%, respectively. This is consistent with the lower fatality rate for females previously reported in the Great Britain study. The elevated fatality rate found in Great Britain could be a result of data being 13 years older, the improvements of modern health care, or the emergency response time for rural versus urban location of incident. The final relative statistics supplied by the NHTSA were injuries and fatalities by age. It was shown that the majority of incidences occurred between the ages of 10 and 30 years, and

risk of fatality increased with age [16]. This review of pedalcyclist and motor vehicle collisions did not include any information about the vehicle.

The first study to analyze vehicle-to-pedestrian collisions for a more aerodynamic vehicle body style, similar to current model types, was the Pedestrian Crash Data Study (PCDS). It encompassed incidents that occurred in the United States from 1994 to 1998 [27]. The NHTSA thoroughly investigated 521 pedestrian crashes by gathering data through the Crashworthiness Data System (CDS), which is a part of the National Automotive Sampling System (NASS) [27]. In order for a collision to qualify for this study it had to meet several conditions including, the vehicle moving forward at time of impact, the vehicle had to have an exterior design consistent with those manufactured within the previous 5 years of the study, and the pedestrian must have been standing at time of impact [27]. The study accounted for 144 different variables to record a comprehensive report of each incident [27].

Regarding gender and age, the PCDS found that 51% involved males and 58% of all pedestrians were between the ages of 19 and 65 years [27]. A correlation between height and injury severity was also observed. The largest group was pedestrians between 60 inches and 66 inches, accounting for 39% of injuries [27]. Relative to this work, 33% of pedestrians were between 67 inches and 72 inches, and of this percentage 42% received a severe injury accounting for 44% of total severe injuries [27]. The height of the pedestrian was significant because injuries and severities were directly related to the geometry of the vehicle, which is discussed later in this section.

The distribution of vehicles in this study over represented passenger cars and underrepresented light pick-up trucks for the recorded type of injury inflicted by all vehicles on the road [27]. This discrepancy has become even larger with an increase of sales in light pick-up trucks and SUVs since this study [22]. Therefore, to represent the relationship of vehicle type to severe injury, the percentage of severe injuries per total injuries inflicted by vehicle type was calculated with the provided data. The result revealed 17% of injuries committed by a passenger car were severe compared to 24% by light pick-up truck. The final two observations relevant to this research were the orientation of the pedestrian upon impact and the velocity of the vehicle. It was recorded that only 10% of the pedestrians were facing away from the vehicle and approximately 45% of the vehicles were traveling between 9 mph and 28 mph. The low percentage of pedestrian rear-end collisions was consistent with other papers.

The Pedestrian Crash Data Study was the basis for a majority of current vehicle-to-pedestrian collision studies. A Field Data Analysis of Risk Factors Affecting the Injury Risks in Vehicle-to-Pedestrian Crashes by Zhang et al. [2008] focused more directly on the likelihood of sustaining severe injury by analyzing 312 cases from the PCDS data [26]. The study excluded people under the age of 14 years and shorter than 59 inches in stature [26]. They emphasized the geometry and speed of the vehicle to influence the severity of injury to the head, torso, and lower extremities. In specific interest to this thesis, it was mentioned that in pedestrian collisions with light trucks or vans, the torso was the second most commonly injured area [26]. This supports the assumption and focus on a larger vehicle and the need for increased protection of the torso region. Their findings revealed a statistically significant correlation

between hood heights above 39.75 inches and severe torso injury [26]. Unfortunately, this study did not account for the direction of impact.

The vulnerability and frequency of cyclist and pedestrian fatalities required an examination of impact biomechanics to reveal the source of injury. "Fatal Vehicle-to-Bicyclist Crashes in Sweden – an In-Depth Study of Injuries and Vehicle Sources" was conducted in 2012 to help understand the injuries inflicted onto cyclists by vehicles [28]. This study analyzed all fatal vehicle-to-bicyclist collisions in Sweden involving a passenger car's front end between 2002 and 2008. The permissible vehicle types were passenger cars, sports-utility vehicles or multipurpose vehicles. A total of 48 cases were admitted and 50 were excluded due to vehicle type or direction of impact. The gender and age of persons involved, and vehicle speeds were consistent with previous studies. The percentages of total pedestrian deaths associated with impact direction were 75%, 23% and 2% from the side, rear, and front, respectively [28]. This study also compared bicyclist data to pedestrian data analyzed by Oman et al in 2012. The corresponding pedestrian fatalities were 67%, 25% and 7% from the side, rear, and front, respectively [28]. The similarity between bicyclist and pedestrian fatalities was consistent throughout the study and therefore, only the bicyclist data will be mentioned.

The majority of deaths were attributed to head injuries (65%), with 27% from thorax injuries, and 21% from neck injuries [28]. The study did not limit the attribution of a person's death by injury to just one area of the body, resulting in a percentage greater than 100%. It was consistently found that the victim's head was typically the location of critical injury. The area of fatal injury was then related to four segments of the vehicle, see table below [28].

Table 2: Distribution of body region with fatal injury by vehicle segment [28].

	Windshield Area (%)	Hood (%)	Hood Edge (%)	Front (%)
Head/Neck	67	9	3	0
Thorax	18	9	3	0
Pelvis	0	0	3	0
Lower Ex.	0	0	3	0

This distribution indicates a person's head as the most vulnerable body region in relation to the least forgiving segment of a car, the frame surrounding the windshield. For the head to reach the windshield area, the vehicle's hood must be low to the ground. It was reported that in 7 cases the bicyclist was struck from behind and their head impacted the frame above the windshield [28]. A larger vehicle, the focus of this research, would prevent the head from surpassing the hood. The author speculated that the fatalities from the head or thorax striking the hood or hood edge may have been inflicted by a SUV. The 9% of head impacts to the hood represent the injuries examined in this study.

Rear impacts, in vehicle-to-pedestrian collisions, were found to be not as common as lateral impacts [27]. However, due to the associated high risk, they were a sufficient basis for the development of a novel protective body armor against high-energy non-penetrating trauma.

2.2 Vehicle-to-Pedestrian Modeling and Testing

Modeling the impact between a vehicle and pedestrian for injury prediction was extremely complex and required extensive computing capabilities. The two most commonly used full body models are the Total Human Model for Safety (THUMS) and the Human Model for Safety (HUMOS) [25]. A third, more comprehensive model, called the Global Human Body

Models Consortium (GHBMC) was developed for the 50th percentile male in the seated position [25]. The complexity of these models exceeded the scope of this thesis and is an area of future work.

Han et al. analyzed two THUMS pedestrian models colliding with four different vehicles with different front-end geometries [29]. This previously validated model provided impact forces, velocities and stresses for the entire musculoskeletal system. The model was solely used to analyze lateral impact loading and neglected to include results for the thoracic region. The only result provided for the chest was deflection of the ribcage, which was not particularly relevant to this research from the direction of impact. Regardless, this method of modeling vehicle-to-pedestrian collisions was noted for future research.

Vavalle et al. described the validation of the GHBMC 50th percentile male during lateral impact by comparing results from experimental testing with cadavers [25]. The model in this study was in a seated position with force plates placed along the left side, illustrated in Figure 1. Although the model represented a person driving a vehicle, it also mimicked a person being struck by a large vehicle with a large grill. The three different configurations Vavalle et al. modelled were referred to as Sled A by Pintar et al. [30], Sled B by Cavanaugh et al. [31], and lateral drop tests by Stalnaker et al [32]. Sled A was tested at 15 mph and 19.9 mph, Sled B at 15 mph, and the drop tests from a height of 39.4 inches. The GHBMC model results supported the experimental results with exception to the pelvic region. The model predicted an impact force with the pelvis that was significantly larger than recorded from cadaver testing.
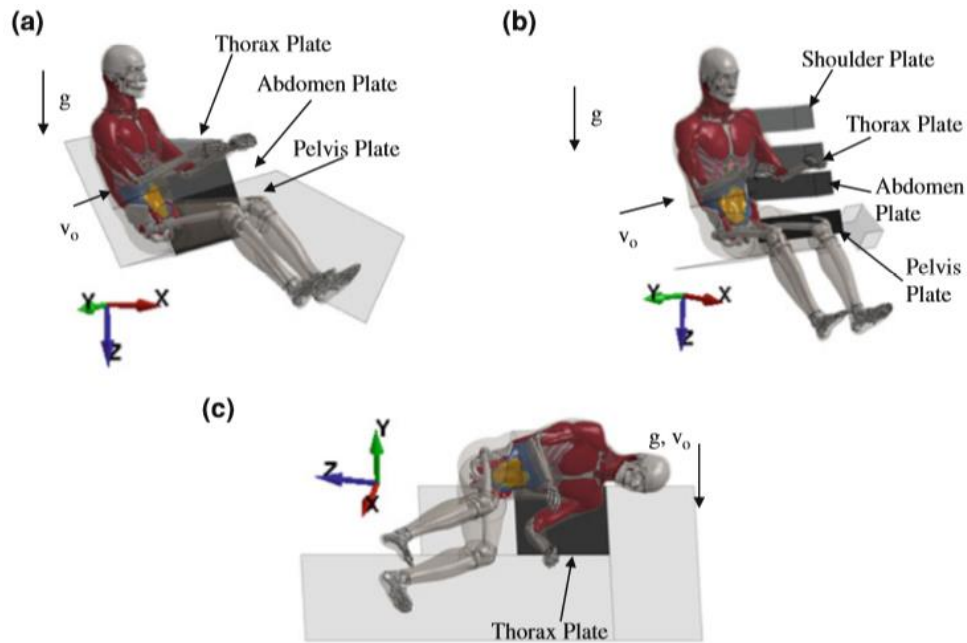
FIGURE 2. Set-up for (a) Sled A tests, (b) Sled B tests, and (c) drop test with gravity (*g*) and initial velocity (*v*ₒ) indicated.

Figure 1: Three different set-ups to validate the model with lateral impact [25].

Sachin Narkhede, from Wichita State University, used the MADYMO (Mathematical Dynamic Model) pedestrian total human body models to analyze truck-to-pedestrian impacts in 2007 [3]. He selected impact speeds of 12.4 mph, 15.5 mph, 18.6 mph, 21.7 mph, and 24.9 mph. All impacts occurred with the front of the vehicle and from the front, side, or rear of the pedestrian. The rear impact with a 50th percentile male model at a speed of 21.7 mph resulted in a high risk of injury to the head and chest regions [3]. Damage to the head was reported to be 2 to 3 times larger than the biomechanical limit and considered fatal [3]. Rear impact at the same velocity also resulted in the chest region reaching an acceleration almost twice that of the biomechanical limit, nearly 120 G's [3].

Bass et al. developed a model to determine thoracic and lumbar spinal impact tolerances by using cadaveric porcine subjects [24]. Their method involved dropping various

masses directly onto the animal's spine from a height of 39.4 inches. They measured the drop velocity, impact force, and deceleration of the mass upon contact with different vertebrae. The pigs were then examined for fractures and other resulting injuries. The forces and risks of injuries were then scaled to human values using anthropometric parameters. The use of porcine subjects was beyond the scope of this project but could be useful in future research.

A simplified method of modeling vehicle impact was conducted using drop test procedures. Yucheng Liu compared the impact forces generated by dropping a cylindrical rod onto an automotive bumper using a physical model and finite element model [33]. Dynamic load transducers were used for experimental testing and a transient analysis was used in ANSYS for Finite Element Analysis (FEA). The resulting forces were within a 3% error and therefore supported the computer modeling method. The simplicity of the modelling and drop testing method was leveraged to develop a similar setup later in this work.

2.3 Impact Absorbing Materials

Ding et al. reviewed the properties of shear thickening fluids (STF) and their applications [34]. STF materials are considered non-Newtonian because they are strain rate dependent. This means that how they react to applied loads is dependent on how fast they are struck. These fluids are initially in a liquid state. However, when the fluid is impacted above its critical shear rate, it becomes momentarily rigid. The critical shear rate and the area of rigidity are dependent on the material's particle concentration, size, shape, size distribution and inter-particle interactions [34]. The addition of a STF to an open cell polyurethane (Poron XRD) or formation by polymer blending (D3O) creates a soft pad or gel with superior impact absorbing properties [34].

Tyler and Venkatraman reviewed the use of impact resistant materials to protect athletes during sporting events [14]. These materials were used to protect the head, back, chest, and other various body parts. The mentioned materials were GPhlex, D3O, Poron XRD, EVA foam, and leather. The first four materials were commercially available, with Poron XRD and D3O as market leaders, and leather was used as a baseline [14]. Testing of material force attenuation consisted of dropping a 1.97 inch diameter ball and striking the material with 3.688 ft lb of energy. Materials were tested at a range of thicknesses. At 0.197 inches thick, D3O out preformed all other products, but as thicknesses increased, Poron XRD began attenuating more force. All four commercially available products were similar in force attenuation at 0.59 inches thick. Since, the tested energy impact in this study was substantially lower as experienced in a vehicle-to-pedestrian impact, these functional properties were not validated but rather demonstrated viable materials.

2.4 Current Devices and Patents

Jing Ma published a master's thesis in 2012 called, "Back Protection Concept Design Research" [35]. The work focused on a physical ergonomic design to minimize the restriction on a person's range of motion. The conceptual phase went through several stages of ideation. Initially he proposed a few designs that covered the entire back using hard shell plates and soft padding in different arrangements. After a shift in focus, the ideation process concentrated on positioning the design as close to the human body as possible and only along the spine. Possible materials were only mentioned, and the design was not fabricated beyond paper or foam models. Although Ma discussed many different configurations, all of them utilized a single impact absorbing material adhered to an undergarment.

Countless patents have been filed covering many different designs and materials for protective devices. Jason Berns patented a spinal and back protecting system in 2004 [36].This system utilized an energy absorbing material in combination with a semi rigid support structure. The absorbing material was suggested to be two layers with the inner layer a low-density foam and the outer a high-density foam. The rigid structure was a series of winged joints that allow the user to flex laterally, see Figure 2. Additionally, the segments were connected using circular discs that slid along score lines along the longitudinal axis. The winged design provided the user with sufficient lateral bending, but the joints restricted rotation and anterior bending of the spine.
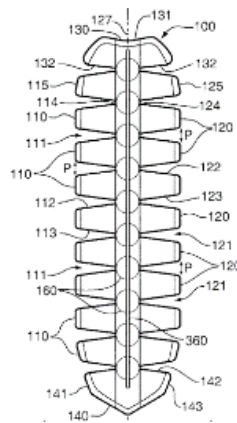
Figure 2: Spinal and back protecting system patented 2004 [36].

Lino Dainese received a patent in 2005 for a back protecting device for motorcyclists, see Figure 3 [37]. The device included two sections of segmented plates and an inner layer of expanded foam. The user's entire spine and part of the glutei were protected. The lower plate was connected to the upper plate at approximately the middle of the lumbar region using a pinned joint. The single joint provided lateral bending. The segments of each plate were slightly

overlapped to allow anterior bending. However, the device did not allow the user to rotate

freely.
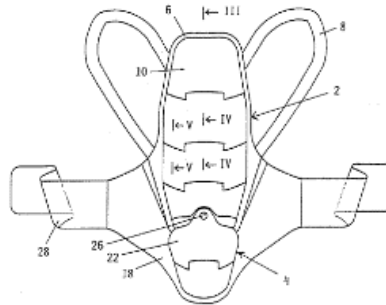
Figure 3: Back protector for motorcyclists patented 2005 [37].

Another device utilizing plates was patented by Giovanni Mazzarolo in 2008 [38]. The

device consisted of a series of overlapping hinged plates stretching from the base of the cervical

spine to the coccyx, see Figure 4. The hinges only allowed for anterior bending and not lateral

bending or rotation. Furthermore, the material was specified as plastic and geared toward

protection during sporting events rather than high energy vehicular impacts.
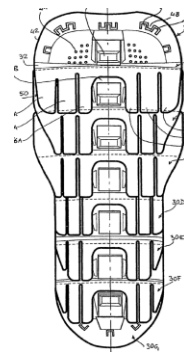
Figure 4: Back protecting arrangement against bumps patented 2008 [38].

Bowlus et al. patented a wearable spinal protective apparatus in 2011 [39]. The

apparatus protected the entire cervical spine to the lumbosacral vertebrae. It was specifically

designed for high velocity activities and protected against hyperextension, spinal compression and blunt force trauma. It had two segments that were connected by a pinned joint, allowing lateral bending similar to Lino Dainese's device, see Figure 5. The hinged segments contained a series of overlapping "Z" shaped plates. They allowed for anterior bending and prevented hyperextension. However, the design was intended to prevent the user's back from rotating, limiting its degrees of freedom.
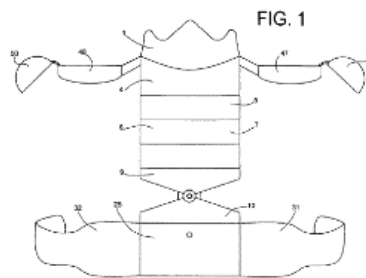
Figure 5: Wearable spinal protective apparatus patented in 2011 [39].

A multitude of patents for soft protective body armor were examined. The products were intended only for energy absorption and provided little to no rigid support. For example, Gavin Reay patented a flexible protective body armor for sports activities in 2012 [40]. The protective gear was a honeycomb like pattern or network of beam and spring elements to absorb direct impact. It was stated to be capable of forming to fit any part of the body.

The two energy absorbing products mention in section 2.3 were found to be readily available in a usable pad form. The first pad, D3O Viper Pro Back Protector developed by D3O Lab, was a synthetic elastomeric polymer. The advantage of this material was its viscous and elastic material properties under deformation, which results in a time-dependent strain characteristic [41]. This pad is more specifically called a dilatant material, also known as a shear

38

thickening fluid [34]. Upon impact, a reaction occurs at a molecular level that locks the fluid particles together [41]. The rigidity of the material also extends past the impacted area because of this molecular reaction. The increase of area allows for a greater force attenuation. After impact, the particles separate, and the material returns to its free-flowing state. The innovative pad remains soft and flexible until impact and then returns to that state after the load is removed [42]. Open cell polyurethane foams also exhibit rate dependent characteristics [43].

The second product, PORON XRD B-Guard, is an extreme impact protecting foam designed by Rogers Corporation. This open cell polyurethane foam behaves similarly to dilatant materials. The open cell structure allows the pad to compress and dissipate the energy. The pad is stated to absorb 90% of the transferred energy [44]. After impact the foam returns to a flexible state and expands to its original thickness.

The energy absorbing capability of back protective armor is tested to EN 1621 standards [45]. These standards cover motorcyclist's protective clothing against mechanical impact at two levels. The test procedure involves dropping a 11 lb flat faced impactor, which strikes the material at 10 mph reaching an impact energy of 37 ft lb [45]. The material is resting on a hemispherical anvil with a radius of 1.97 inches [45]. The transmitted forces determine if the material is Level 1 or Level 2. PORON XRD B-Guard scored at Level 1, indicating the mean transmitted force was below 4,047 lb [44] with no single strike exceeding 5,395 lb. D3O Viper Pro scored a Level 2, indicating the mean transmitted force was below 2,023 lb [46] with no single strike exceeding 2,698 lb.

A similar type of impact absorbing material was present in most of the previously

mentioned patents. The force attenuating qualities of these materials are required for all

impact scenarios and will be included as a single component in this work. Research literature, a

patent review, and an industry survey of existing devices confirmed a need for better

pedestrian and pedalcyclist wearable protection against larger vehicles on the road. This thesis

focuses on the development of a novel design for the rigid component and produces monitored

test results from a real-world high-energy impact scenario to demonstrate the protective

capability of a wearable back device.

3 Methodology

3.1 Methods

Complementary methods were applied throughout this work to complete the design, analysis, development, and test of an innovative safety device. These methods included analytical analysis, finite element analysis, and experimental testing. Tools used included three-dimensional (3D) modeling, manufacturing, and data collection, which will be discussed in their respective sections.

Analytical analyses were used throughout the entire project. First, theoretical impact force calculations were conducted using anthropometric data during concept development, shown in Appendix B. Next, structural analysis was used during the modeling phase. Simple beam calculations were completed using a simplified model of the device to support the material selection, see Appendix B. Analytical methods were also used during data analysis. Raw accelerometer data were collected during testing to better understand the impact scenario and determine the significance in placing different materials between the human model and the vehicle model, discussed and graphically displayed in section 4.2. No similar data nor analysis methods were found during research at the time of publication. This required a thorough inspection and understanding of the results through graphical analysis and comparison to concurrently captured video footage. Data were analyzed using several methods including calculating averages, trapezoidal approximation for area under a curve, and calculating vector magnitudes.

The finite element method was employed during the product design phase using the computer program ANSYS Workbench. FEA allowed for a structural integrity evaluation of the device based on its material properties and geometry during the impact loading scenario. The proprietary material properties and complex nature of the impact absorbing pad limited the FEA model to only the rigid structure. A final analysis of the device demonstrated the expected stresses, strains, and deformations as a result of impact loading. A detailed evaluation will be discussed in the finite element modeling section 3.5.

Lastly, the experimental method included a pilot study and full scale drop testing. The pilot study applied a mock impact scenario to verify the data collection method and video capture arrangement. This study also established a baseline for several unknown variables and revealed the impact mechanics between the human model and vehicle model. Final drop tests were conducted at the target velocity of 20 mph to validate the completed device.

3.2 Material Selection

The proposed device was envisioned as a combination of a rigid exoskeletal structure and an impact absorbing material. The rigid structure was conceptualized as a series of specialized joints acting as an external Support Column to Allow Rotation and Anterior Bending of the Spine (ScarabSpine). The ScarabSpine was the primary focus of product development. However, a force attenuating element was required to act as a barrier between the human body and a rigid device. The ScarabSpine materials were selected as a high-grade aluminum alloy supported by stainless steel. The majority of material was aluminum to achieve minimal weight, but stainless steel was necessary because of its greater shear strength.

Rigid materials were selected to be light weight, corrosion resistant, machinable, affordable, and withstand high impact forces. For example, two suitable aluminums were 6061-T6, for general purposes, and 7075-T651, a readily available higher-grade alloy with a slight increase in price. A general purpose 304 stainless steel was selected for affordability and superior shear strength. Ultimate tensile strength, machinability, and shear strength are compared in Table 3. A full table of material properties is provided in Appendix A. 7075 aluminum was far superior to 6061 and was better suited for the required characteristics. In particular, 7075 demonstrated ultimate tensile and shear strengths that are respectively 1.8 and 1.6 times stronger than 6061. These parameters were relevant during FEA because the material was able to withstand a higher stress without catastrophic failure. The higher machinability percentage was also an advantage during prototype fabrication.

Table 3: Aluminum alloy and stainless steel material properties [9] [8] [7] [47].

	6061-T6	7075-T651	304
Modulus of Elasticity (ksi)	10,000	10,400	29,000
Ultimate Tensile Strength (psi)	45,000	83,000	97,000
Machinability (%)	50	70	-
Shear Strength (psi)	30,000	48,000	72,750

The impact absorbing material was selected from the two advanced force attenuating pads discussed in section 2.4. Based off the EN 1621 standard, the D3O Viper Pro attenuated impact forces superior to the PORON XRD B-Guard and was selected as the impact absorbing element required for this work.

3.3 Concept Development

After the selection of the D3O Viper Pro functional requirements were generated for the ScarabSpine and device as a whole. The Viper Pro attenuated impact forces on its own but could only act across the area of the back that was directly contacted by the vehicle. Therefore, the addition of the ScarabSpine extended the distribution of force up along the length of the user's back. The large Viper Pro, which was designed for the 50% male, was pre-manufactured to 17.5 inches long and limited the length of the ScarabSpine. This design constraint limited the device to extending from the top of the thoracic region (T1) to approximately the middle of the lumbar region (L3), illustrated in Figure 6.
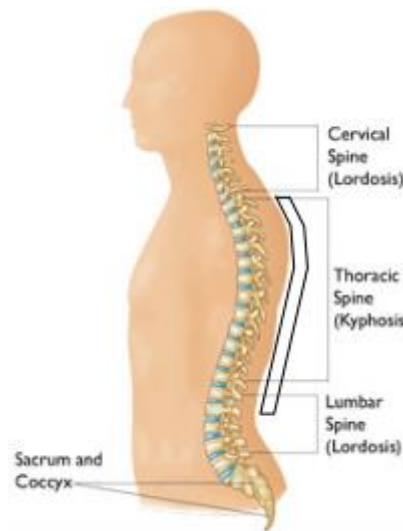
Figure 6: Segment of male spine indicating placement of the ScarabSpine [48].

The selected range placed the hood of the vehicle directly in the center of the ScarabSpine. The lower half of the device would be in direct contact with the vehicle requiring only the top half to support the forces applied by the upper portion of the user's body. Additionally, extension to the L3 vertebra simplified the ScarabSpine design because it ended

44

just before the body's natural recurve at the hips. Ideal coverage would extend the device further down to include the coccyx and up to include the cervical spine. However, those extensions were beyond the scope of this first work. The design of the rigid structure prevented the patient's thoracic spine from hyperextension, while a series of joints did not overly restrict anterior flexion, lateral movement, or rotation. The ScarabSpine would distribute the impact force up and the Viper Pro spread the force across the patient's back. Additional functional requirements for the ScarabSpine included light weight, simple assembly, modular, detachable from Viper Pro, corrosion resistant, and ergonomic.

Having defined the protected region, initial force calculations were performed using anthropometric data. The assumed hood height was directly between the middle torso and upper torso regions. The corresponding segment weights were 24 lb and 41 lb, respectively, found in Table A.1 in the Appendix. Based on their respective segment lengths, the bottom half of the device supports the total impact force of the middle torso and the top half supports the total impact force of the upper torso, assuming the device covers the entire surface area of the respective segments. Having used a constant acceleration of 60.7 G's from Equation B.2 and Newton's second law, Equation B.3, the bottom half and top half received a constant 1,466 lb and 2,487 lb, respectively. The largest calculated force set the limit for allowable average force and acceleration transmitted by the device. Peak accelerations for the chest region were found in literature to not exceed 85 G's for a time interval longer than 3 ms [3]. A list of detailed specifications was developed for the ScarabSpine, D3O Viper Pro, and total device, see Table 4.

Table 4: Specifications for ScarabSpine, Viper Pro, and Total Device.

No.	Specification	ScarabSpine	D3O Viper Pro [46]	Total Device
1	Weight	≤ 3 lb	1 lb	≤ 4 lb
2	Length	≤ 17.5 in	17.5 in	≤ 17.5 in
3	Width	≤ 6 in	10.8 in	≤ 10.8 in
4	Thickness	≤ 1 in	0.7 in	< 1.75 in
5	Posterior Static Extension	≤ 0.25 in	Not Restricted	≤ 0.25 in
6	Posterior Dynamic Extension	≤ 1.6 in	Not Restricted	≤ 1.6 in
7	Anterior Flexion	> 45° +/- 5°	Not Restricted	> 45° +/- 5°
8	Rotation	> 180° +/- 5°	Not Restricted	> 180° +/- 5°
9	Transmitted Average Force	-	-	< 2,500 lb
10	Transmitted Average Acceleration	-	-	< 60 G's
11	Peak Acceleration Time Interval	-	-	< 3 ms

The weight of the total device was baselined from current products on the market. A high-end airbag jacket for motorcyclists contains an impact absorbing pad and inflation system that has a weight of approximately 3.3 lb [49]. With this starting point, the target maximum weight was set at 4 lb limiting the ScarabSpine's metallic components to only 3 lb.

The length of the ScarabSpine was limited by the length of the Viper Pro resulting in a maximum dimension of 17.5 inches. Likewise, the width of the ScarabSpine was constrained to 6 inches due to the smallest width of the Viper Pro, not including the tapered edges of the pad, see Figure 7. The combined thickness of the pad and metal segments was selected as less than 1.75 inches providing more than 1 inch for the ScarabSpine, in other words the device will not protrude from the user's back further than 1.75 inches. This dimension was determined during the design phase because it was highly dependent on the metal's material properties.
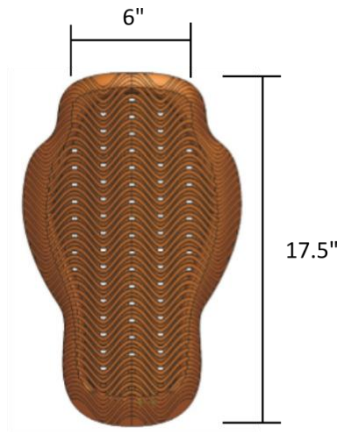
Figure 7: Usable dimensions for the Viper Pro pad.

The permitted movement between the ScarabSpine's segments controlled how far the user could bend backward (posterior extension), bend forward (anterior flexion), or rotate about the vertical axis. Posterior extension was measured without a load (static) and with a load (dynamic). A maximum posterior static extension of 0.25 inches over the entire length of the ScarabSpine was designated to account for manufacturing tolerances and clearances between segments, see Figure 8. This posterior extension is equivalent to an angle less than 1 degree.
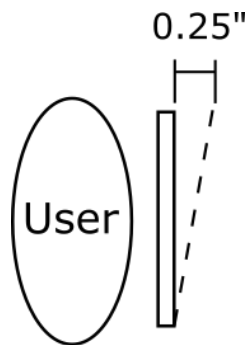
Figure 8: ScarabSpine static extension.

A posterior dynamic extension, or deflection under impact, was selected based on the allowable range of motion of the human spine. Maximum deflection between two thoracic vertebrae was, on average, approximately 1.5 degrees [50] [51]. The hood of the vehicle approximately impacts the T8 vertebra resulting in a deflection of 10.5 degrees, due to 7 intervertebral discs, from the highest point of impact, i.e. hood height. On the other hand, anterior flexion was highly desirable to allow forward bending.

The thoracic spine provided approximately 20 degrees of bend, and the upper portion of the lumbar spine approximately 25 degrees [51]. Therefore, the total permitted anterior bending was 45 degrees. The novelty of this design was from the unrestricted rotation of the user. The total device was to allow 180 degrees of rotation about the vertical axis, 90 degrees from center in either direction of rotation. To accomplish the selected range of motion and other functional requirements, the ScarabSpine incorporated unique geometry and complex joint design.

The general shape of the ScarabSpine was a triangular column. This geometry provided a large wide flat surface to sit flush against the Viper Pro pad while maintaining the 1 inch thick constraint, unlike for example a circular column. Additionally, a triangular cross section was selected because it requires less material than a rectangular cross section without compromising structural integrity of the column. Simple cantilever beam calculations comparing deflections for each cross section are provided in Appendix B. The shape minimized weight and maximized the impact surface by effectively halving the area while keeping the full cross-sectional width, illustrated in Figure 9. The figure also shows rounded corners to eliminate sharp edges with the potential to puncture the user or Viper Pro pad during impact.
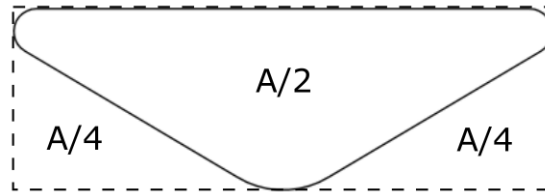
Figure 9: Approximate area reduction between a rectangle and triangle.

The column was divided into segments to satisfy the modular aspect and provide mobility. Joints were expected to have 360-degree rotational freedom about the vertical axis. This was accomplished using a ball in socket model. A ball stud protruded from one segment and rested in a spherical pocket provided by the adjacent segment, illustrated in section 3.4. Appropriate clearance in the joint allowed free rotation between segments, discussed further in the next section. This design required two parts to each segment, not including the ball stud. There was the base, which contained the bulk of the material, and the base cap. Each part supplied a half sphere and groove to contain the ball stud's shaft and spherical end. The cap was secured using two screws providing easy assembly.

Finally, flexion and extension were limited by the groove's geometry. The base's groove was angled to allow anterior flexion between each segment. Conversely, the base cap's groove was straight to prevent hyperextension of the spine. These details were the foundation for the ScarabSpine design.

3.4 ScarabSpine Design and CAD

The ScarabSpine concept had a general shape but lacked dimensions. An initial length, width, and thickness, for the triangular column were selected as 16 inches, 3 inches, and 1 inch, respectively, see Figure 10. A length of 16 inches provided 0.75 inches of clearance on either

end when placed at the center of the Viper Pro pad. This clearance reduced the probability of the metallic components contacting the user during impact. The width of the device was designed to activate the largest possible surface area of the Viper Pro during impact without adding excess weight. Additionally, maximizing the width ensured the impact forces were spread across the largest possible width of the user's back. For example, if it were thinner than that of the average lumbar vertebrae, which was researched to be on average 1.87 ± 0.20 inches [24], it is possible that the total transmitted impact force could be directed into the user's spine causing catastrophic damage. Finally, the thickness and ball stud dimensions were determined concurrently.
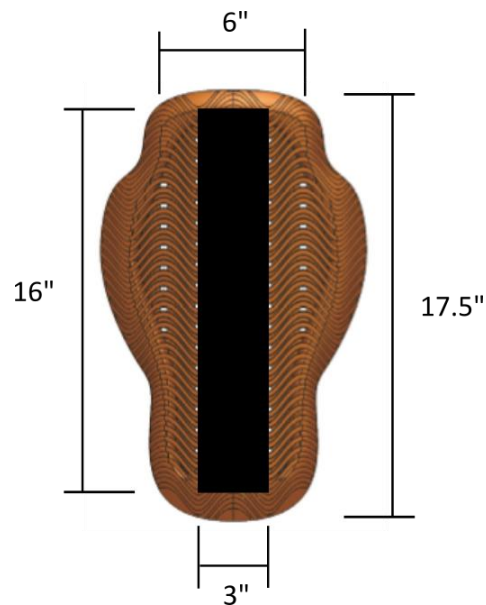
Figure 10: Length and width of ScarabSpine relative to Viper Pro pad.

The ball stud shaft diameter was designed to be as large as possible based on its expectation as a high stress member. It was the only connection between segments and would experience extremely high shear forces. The shaft diameter was chosen as 0.45 inches and

designed from 304 stainless steel. Supporting calculations in Appendix B show the developed

shear force across a circular cross section with the selected diameter would exceed the shear

strength of aluminum but not the ultimate shear strength of 304 stainless. Extending from the

shaft was a spherical end with a diameter of 0.625 inches. A segment thickness of 1 inch

provided an aluminum wall thickness of 0.188 inches that fully enclosed the ball joint. The shaft

diameter and length were highly dependent on the number of segments. Before determining

the division of segments, simplified beam calculations were performed to support the geometry

and material of the column.

Structural analysis was performed using a cantilever beam model supporting a

concentrated load at the end, see Figure 11. The application of this model to the structural

design of the ScarabSpine provided a preliminary analysis based off the beam's cross section,

material properties, length, and applied force. The method of solving this base model was

modified to incorporate impact loading and allow calculation of a maximum dynamic

deflection. The impact scenario was evaluated assuming the pedestrian was dropped from a

height resulting in a 20 mph impact. In a drop test model, this was equivalent to releasing the

object from approximately 160" above the target, see Appendix B.
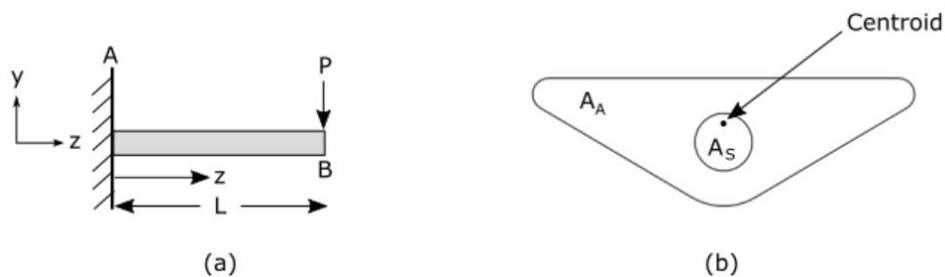
Figure 11: (a) Cantilever beam diagram with concentrated load and (b) cross-sectional area.

The maximum deflection was then obtained by equating the potential energy loss of the

pedestrian to the maximum strain energy absorbed by the beam. This equation was applicable

through the principle of Conservation of Energy as developed in the *Mechanics of Materials (7th*

Edition) textbook [52]. The strain energy method was an over approximation for impact

conditions because of its many assumptions. Assumptions included the beam responded with a

linear elastic behavior, its shape during deflection was the same regardless of dynamic or static

loading, and there were no energy losses [52]. These were noted for comparison with the

simulated environment during FEA. For example, during finite element modeling it was

recognized that the deflection shape was different for uniformly applied static loading versus

dynamic loading. This reaction was due to the rigid fixation method of a cantilever beam model

and was circumvented by selecting a concentrated point load rather than a uniformly

distributed load. The disregard of energy loss was also a large simplification because a

pedestrian impact has appreciable energy loss from the body's compression. This simplified

approximation method revealed a worst-case maximum deflection and maximum impact force.

Calculation of the maximum deflection and impact force required the column's cross-

sectional moment of inertia. This was found by generating the column in SolidWorks™. The first

part was a triangular aluminum column of 8 inches in length with a 0.45 inch diameter hole

extruded through its center. Then, a 0.45 inch diameter stainless steel rod of equal length was

created and placed into an assembly with the aluminum column, see Figure 12. These parts

were 8 inches long to satisfy the designed length to extend above the vehicle's hood and

support the pedestrian's chest region. SolidWorks™ revealed the cross-sectional moment of

inertia for both parts with respect to the centroid. The maximum deflection and maximum

impact force were calculated to be 0.934 inches and 7,070 lb, respectively. Full calculations are shown in Appendix B, and resulting values were used to support the ANSYS model in the FEA section. The deflection was below the specified dynamic extension by 0.66 inches and adequately supported the column's design before applying the joints.
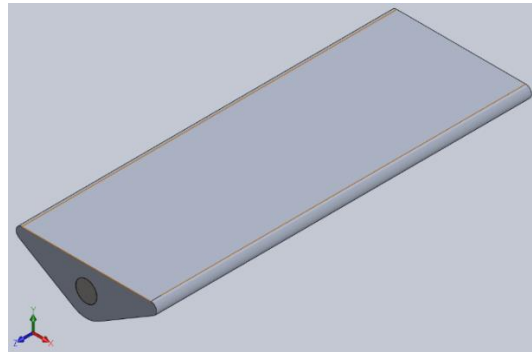
Figure 12: Triangular aluminum column and SS rod assembly for cantilever beam calculations.

The full column was divided into 10 segment assemblies utilizing 9 ball and socket joints. Figure 13 shows the complete ScarabSpine model attached to the Viper Pro pad in different orientations. There was a total of three unique segment assemblies with the middle eight being identical. Each joint provided 10 degrees of forward bending for a total of 90 degrees (Figure 13c).

(a)   (b)   (c)
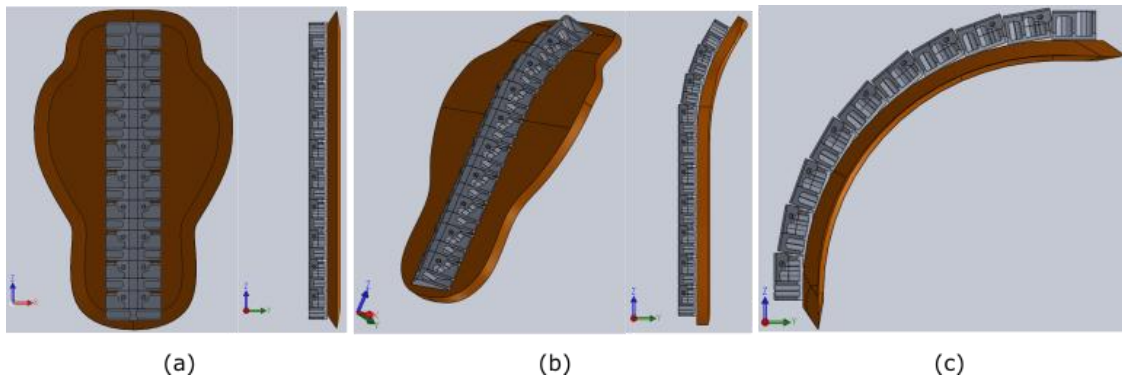
Figure 13: ScarabSpine and Viper Pro models in (a) straight, (b) natural spine, and (c) maximum forward bend forms.

The natural resting curvature of the upper thoracic spine matches the ScarabSpine with the top three joints all angled at 10 degrees (Figure 13b). In this form, Figure 14 shows its placement on a human model.
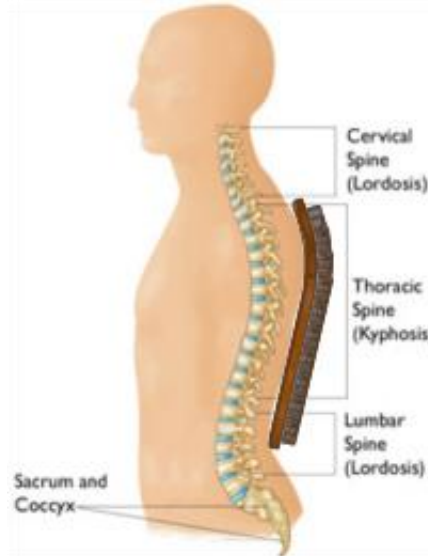
Figure 14: ScarabSpine and Viper Pro model in natural spine form on pedestrian.

The complete ScarabSpine model consisted of five unique parts and one unique socket head cap screw. Parts included one top segment, eight middle segment bases, one bottom segment base, nine base caps, and nine ball studs. Two screws were required to assemble each joint resulting in a quantity of 18 components. The top segment did not require any screws because it was the first part and was designed from a single block of aluminum. The top segment assembly and parts are shown in Figure 15. Large slots were cut into the top segment (Figure 15a) to remove the maximum amount of material without compromising structural integrity. This operation was also applied to the middle and bottom segments. A flat bottom blind hole was placed at the column's thickness center and connected to the shank of the ball stud using an interference fit. Allowance for this fit was selected as a Class FN 5 force fit

specified by the American National Standards Institute (ANSI) [53]. This class is suitable for high

stressed parts [53] and will prevent the assembly from failing during high loads and torques.

The depth of the hole was design as greater than 1.25 times the diameter of the shaft. To

ensure adequate interference and hole depth, the radial interference pressure and coefficient

of friction were used to calculate the axial force required to remove the shaft. The pull force

was calculated to be more than twice the previously calculated impact force indicating the

probability of the shaft being pulled from the segments during the high impact force scenario

was minimal. The ball stud protruded from the bottom of the segment into the first of the

middle segment assemblies.

(a)   (b)   (c)
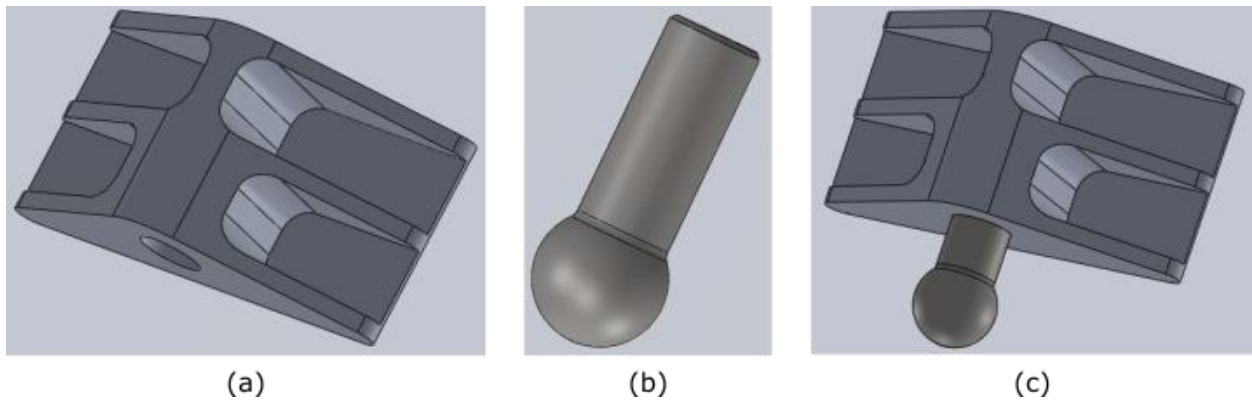
Figure 15: SolidWorks™ models of (a) top segment, (b) ball stud, and (c) top segment assembly.

The middle segment assemblies included the middle segment base, base cap, ball stud,

and two screws. The base, base cap, and full assembly are shown in Figure 16. The middle

segment base (Figure 16a) was designed similarly to the top segment but included a step that

housed the ball stud. The base cap (Figure 16b) enclosed the ball and socket joint and was fixed

using two ¼-28 stainless steel screws. The middle segment base provided two counter bores for

screw placement. The ball stud and slot allowances were selected as a clearance Class 2 free fit

specified by ANSI. This fit allowed the joint to rotate freely and compensate for minor

misalignments.
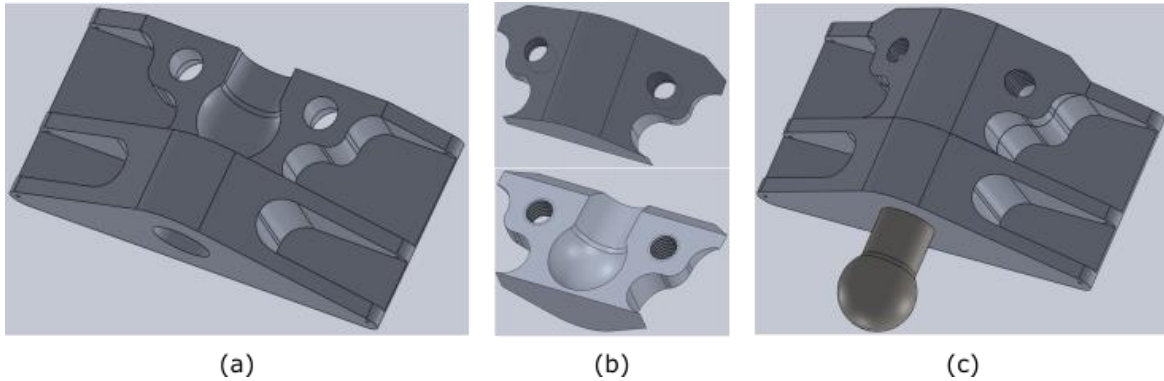
Figure 16: SolidWorks™ models of (a) middle segment base, (b) base cap, and (c) middle segment assembly.

The center of the sphere was placed at the center of the base's width and thickness and

0.5 inches from the top. As a result, the shaft extended approximately 5/16 of an inch into the

socket before reaching the spherical void. The material thickness was designed to provide

sufficient pull strength of the socket while minimizing the overall segment length. Strength of

the ball socket was determined using FEA and is discussed in section 3.5. The depth of the hole

for the ball stud shank and the placement of the spherical slot defined the base's length at a

minimum of 1.5 inches. The base cap was also designed to extend above the segment base by

1/8 of an inch, seen in Figure 16c. This prevented the segments from contacting each other

while bending forward. Figure 17 shows a closer view of the joint bent at 10 degrees. Eight of

these middle segment assemblies were connected in series until reaching the bottom segment

assembly.
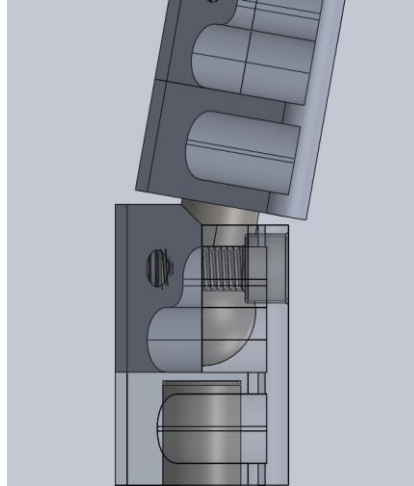
Figure 17: Closeup of joint angled at 10 degrees.

The bottom segment base was almost identical to the middle segment base. It differed by lacking the bottom hole for a ball stud shaft. Figure 18a shows the bottom segment base with the front visible and from the back view to show the counter bore holes. The lower two slots extended closer to the center to remove additional material.
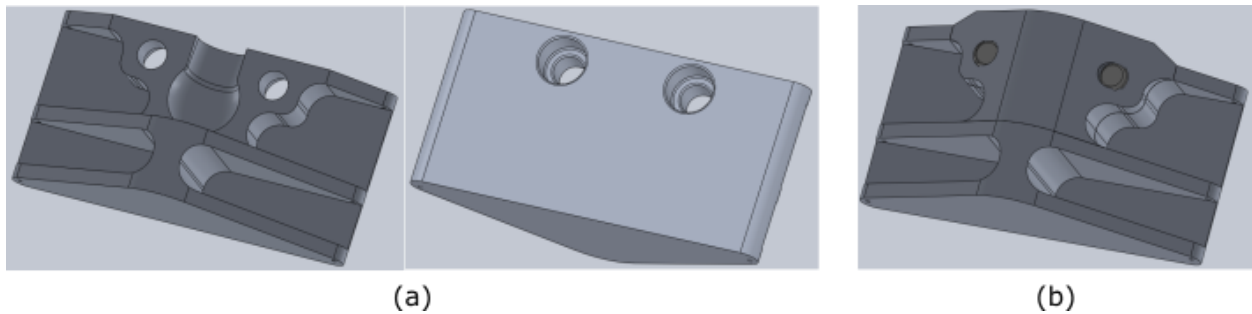
Figure 18: SolidWorks models of (a) bottom segment base and (b) bottom segment assembly.

The total length of the ScarabSpine was 16.125 inches, which included ten 1.5 inch base segments and nine 0.125 inch joint gaps. A final design element was added to fasten the ScarabSpine to the Viper Pro pad. This was accomplished by drilling two small vertical through

holes on the tips of the triangular column allowing the ScarabSpine to be sewn to the pad with high tensile string.

3.5 Finite Element Analysis

3.5.1 First Order FEA

The finite element method was used to evaluated two different models. The first model involved the solid beam shown previously in Figure 12. The second model was a complete assembly of the ScarabSpine with applied forces based on anthropometric data. The first model was simulated to compare hand calculations with the ANSYS Workbench analysis.

The first step was to select the analysis system. A previous work, found during research, used a "Transient Structural" model to simulate a similar simplified impact scenario. The model allowed forces to be applied with respect to time and was accepted for this early work. Next, material properties for 7075-T6 aluminum alloy and 304 stainless steel were added to the Engineering Data library. The model geometry was imported from a saved Parasolid file generated by SolidWorks™. Once imported, the model setup was edited to reflect similar assumptions during hand calculation. Figure 19 shows the bottom of the column labeled "A" was held fixed, the outer face of the column labeled "B" was restrained from moving in the "x" direction, and a weight of 20.5 lb was placed at the end of the beam at "C".
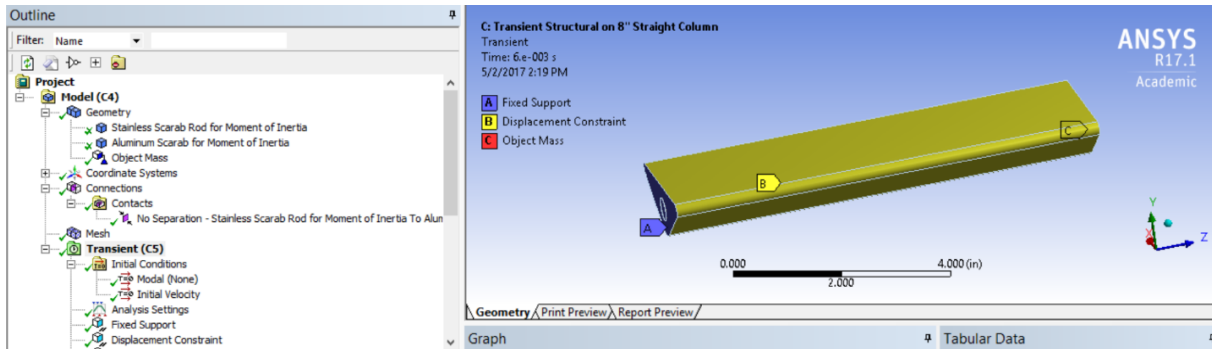
Figure 19: ANSYS setup for solid column FEA.

The energy of a falling mass was applied by adding an initial condition to the beam. This condition was an initial velocity of -352 in/s (-20 mph) along the y-axis. Hand calculation conditions specified that the beam was assumed to remain within the linear elastic range. Therefore, nonlinear effects for each material and the large deflection solver were turned off. Not all assumptions during hand calculations were repeatable in ANSYS Workbench. For example, the change in potential energy of the column could not be ignored and stresses in the column were not defined as uniform throughout the beam. These differences were not accountable due to the over simplification for hand calculations and the complex modeling capabilities of the software.

The results from ANSYS yielded a maximum deflection of 0.941 inches in the y-axis, only a 0.75% difference from hand calculations. This deflection occurred after 4.1 ms with a resolution of 0.1 ms. This time point also revealed a maximum reaction force of 6,578 lb. Direct comparison with a hand calculated load of 7,070 lb resulted in approximately 7% difference. A less than 10% difference was encouraging because several assumptions during hand calculations could not be replicated in the FEA model.

The y-axis component of the average reaction force on the fixed face was also measured. This force represents the constant impact force required to reach the same results with a constant acceleration. The resulting force was 4,960 lb. Newton's second law was then used to calculate the duration of this force resulting in a time of 3.9 ms. The percent difference between measured and calculated times was less than 5% and supports the use of an applied constant force.

Additionally, the constant point force was converted into a distributed force, using Equation B.19, and applied to the same FEA model for 4.1 ms (Figure 20). The resulting maximum deflection from a constant load of 9,920 lb acting only in the "y" direction was 0.941 inches, identical to the results from applying an initial velocity. The application of a distributed force was accepted and will be applied to the ScarabSpine model in the next section. Prior to simulating the full system, the ball socket was analyzed for axial pull strength.
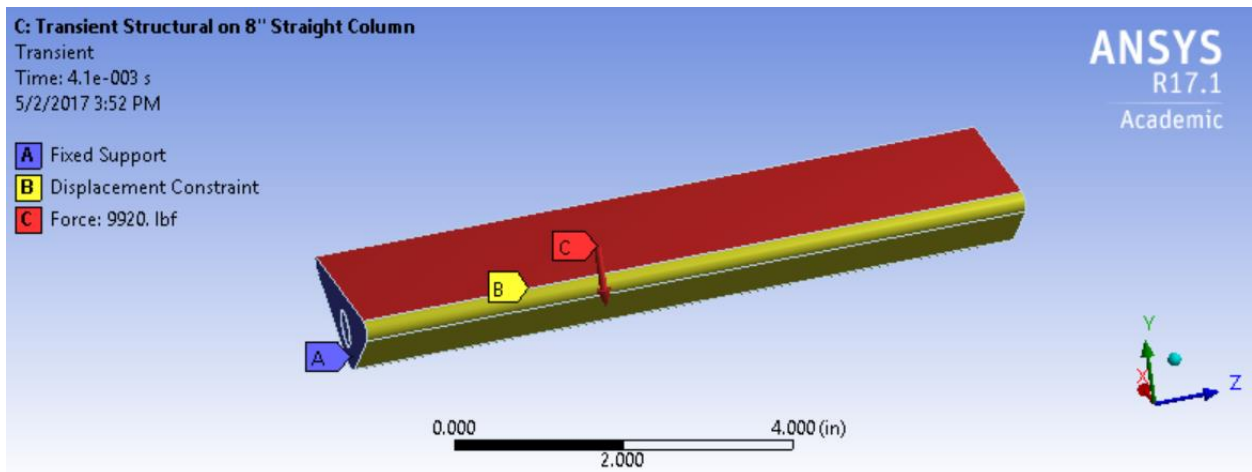
Figure 20: ANSYS setup for solid column FEA with constant distributed force.

A simplified model of the aluminum base and stainless steel ball stud assembly was placed into ANSYS Workbench. The static structural solver was selected to demonstrate the stability of the joint during an axially applied load. A fixed support labeled "A" was applied to an outside face of the aluminum base, and an axial force of 5,000 lb at "B" was set to pull on the ball stud shaft, see Figure 21a. The applied force was approximately half the calculated normal force. This load level was beyond the expected axial force because the majority of impact force will remain normal to the impacting face. Only a minimal amount of force could be transmitted to the z-axis during deflection. The resulting equivalent stress within the assembly did not exceed 35,000 psi, illustrated in Figure 21b. This value was below the tensile yield strength for both materials and supported the ball socket design. The final simulation required to justify the full ScarabSpine design was modeled using a transient structural formulation to facilitate the applied impact time.

(a)   (b)
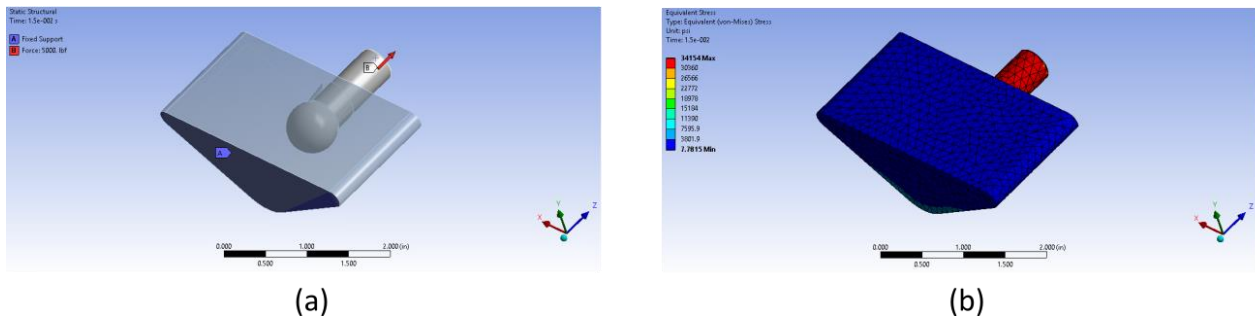
Figure 21: Ball stud pull strength FEA.

3.5.2 Transient FEA

The ANSYS setup parameters for the ScarabSpine simulation required alterations to accommodate a 15 ms impact time. A rectangular block was added to the assembly as a mock user. This block represented a mass undergoing a change in momentum in the specified time. It

provided a distributed force across the ScarabSpine that represented the mass area of the user

covered by the Viper Pro. The total chest area was approximated as 132 in^2 using

anthropometric data [5]. With a weight of 41 lb, the weight per unit area was calculated to be

0.311 psi. The upper half of the Viper Pro was measured to cover 65.6 in^2 resulting in a weight

of 20.4 lb.

A transient structural model was selected in ANSYS Workbench to analyze the

ScarabSpine. As before, the ScarabSpine geometry was saved as a Parasolid file from

SolidWorks™ and imported into ANSYS. 304 stainless steel and 7075-T6 material properties

were applied to their respective parts. To simplify the model, the lower four segments, ball

studs, and all screws were suppressed. The mock user block exactly matched the impact surface

on the remaining six segments and was designated the material properties of polyethylene

plastic, see Figure 22. This selection dimensionally stabilized the 1 inch thick block without

supplying significant rigidity. The block thickness was selected to be smaller than a person's

thoracic vertebral body, which ranges between 1.25 inches and 1.75 inches [24]. The density of

the block was changed to exactly place a weight of 20.4 lb across the top five segments.
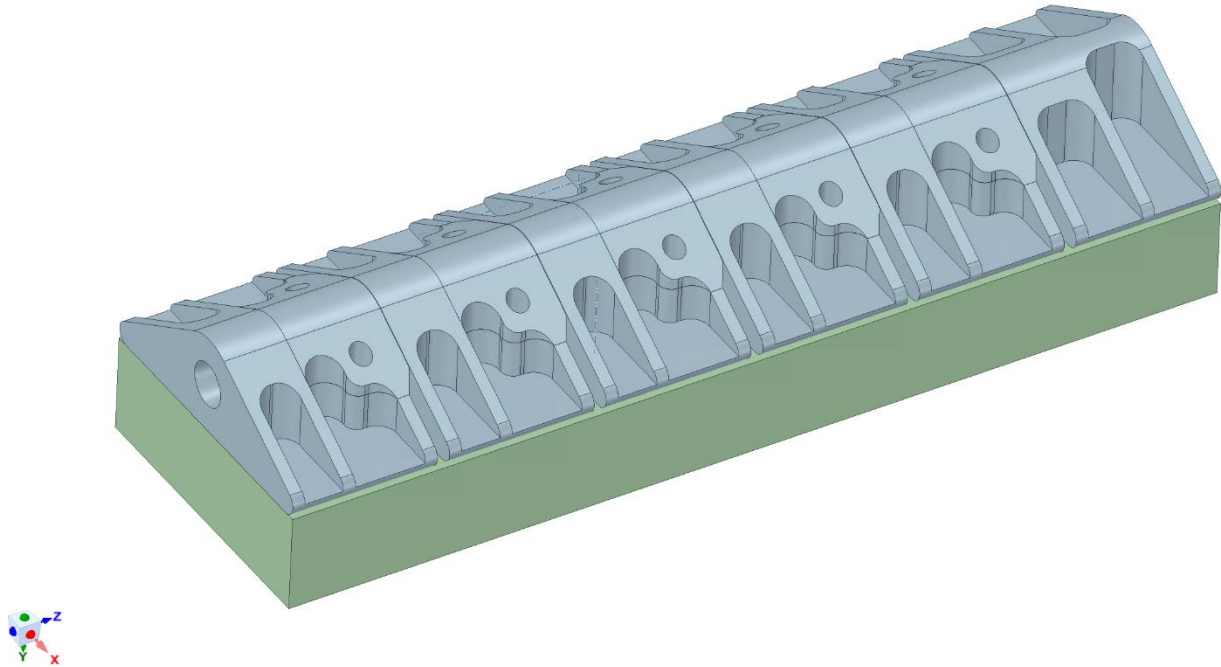
Figure 22: ScarabSpine transient FEA geometry.

Contacts between parts were selected based on assembly method and solution

convergence. The segment bases were defined as "bonded" to their base caps, and the ball

stud shafts were "bonded" to their aluminum base segments. A "no separation" contact was

applied to all ball in socket joints and at the surfaces between each aluminum segment. These

contact types aided in the convergence of a solution by allowing the software to treat the

contact zones as linear. The most notable difference between these contacts is "bonded"

surfaces are treated as adhered to each other and "no separation" surfaces are granted

frictionless sliding without separation. The "bonded" contact was also applied between the

bottom aluminum segment and the mock user block. The last type of contact used was called

"frictionless". It defined the surfaces between the top five segments and the mock user to

prevent the block from adding additional rigidity to the system.

Displacement constraints and velocity conditions were also applied to the system.

Several faces were limited to traveling only in the y-z plane to prevent rotation about the z-axis.

The bottom segment was selected to travel in the y-axis from 0 to 352 in/s in 15 ms. This

motion applied the weight of the mock user across the ScarabSpine as it accelerated to 20 mph

in the designated impact time. The displacement constraints and applied velocity are illustrated

in Figure 23.
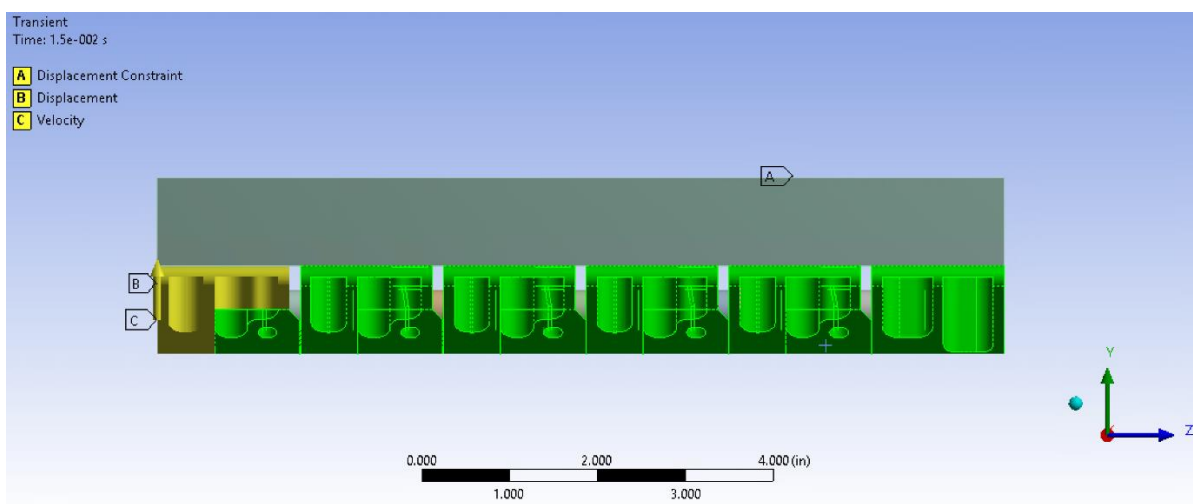
Figure 23: Transient Structural FEA setup for ScarabSpine model.

Unlike prior hand calculation comparison simulations, nonlinear effects for the material

properties and large deflection were turned on. This provided realistic stress development

throughout the beam and resulted in the most accurate deflection evaluation.

3.6 Experimental Testing

The ScarabSpine was fabricated to all specifications and functioned as expected

compared to the SolidWorks™ model. The completed assembly was prepared for experimental

testing, see Figure 24.

Figure 24: ScarabSpine assembly with ball sockets exposed, base caps installed, and sewn to Viper Pro pad.

Testing of the complete assembly was conducted in three phases. First, the device's range of motion was evaluated through physical manipulation. Second, a pilot study was developed to generate a baseline for the collected data and further clarify the impact scenario. The final phase was a full scale drop test to validate the ScarabSpine and Viper Pro's capabilities. An 80 lb professional punching bag was used to model a pedestrian in the second and third phases.

Flexibility of the device included rotation, anterior flexion, and posterior extension. Figure 25 demonstrates the device during these three tests. The ball and socket joints provided more than 90 degrees rotation to both the left and right. Anterior bending of at least 45 degrees was achieved as shown in Figure 25b. Finally, static extension was measured to be 0.2 inches, which was below the specified ¼ of an inch. Total measured weight was 3.75 lb.
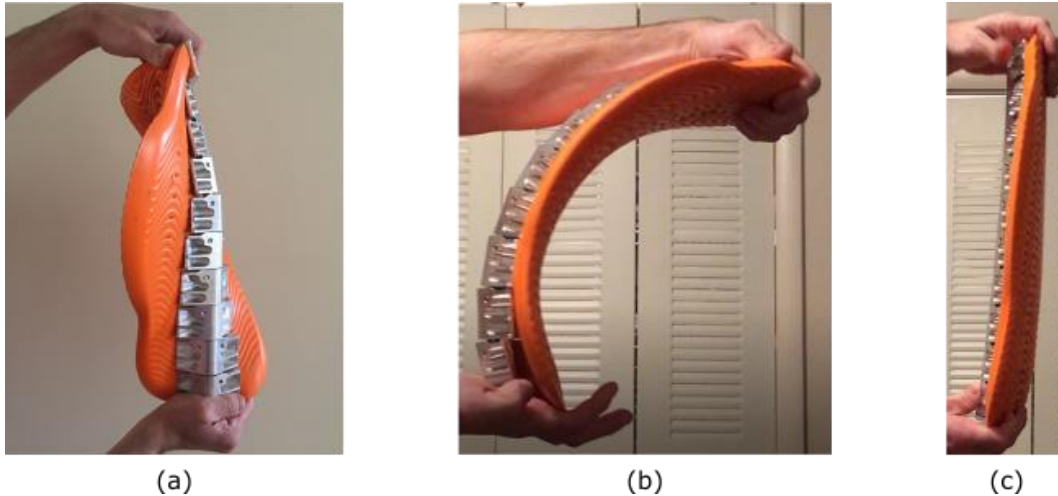
Figure 25: ScarabSpine and Viper Pro ROM during (a) rotation, (b) anterior flexion, and (c) posterior extension.

Phase two involved impact testing between the punching bag and a truck grill model constructed from wood. The pilot study validated the selected data collection methods by consistently generating comparable results under the same impact conditions. The selected testbed was critical for recording consistent data and was provided by Packaging Compliance Labs, LLC (Figure 26) [54].

An industrial grade pneumatically inclined sled (Figure 26a), manufactured by L.A.B. Equipment, Inc., was used to ensure a consistent impact velocity of 6.5 mph. The bag was placed on the sled and supported on either side using wooden struts. These supports only prevented the bag from tilting to either side. The sled was then lifted to a maximum angle of 10 degrees. A strap was tethered to the center of the bag allowing it to tilt to the same angle as the sled without falling forward, see Figure 26b. Upon release, the setup traveled down the ramp and impacted the grill model, which was fastened to a backboard that was perpendicular to the sled. The grill was oriented so that approximately 10 inches of the bag extended above

66

its top edge. This overhanging segment weighed approximately 20 lb and simulated the portion

of the pedestrian that would be protected by the Viper Pro pad as previously discussed in the

FEA section 3.5.
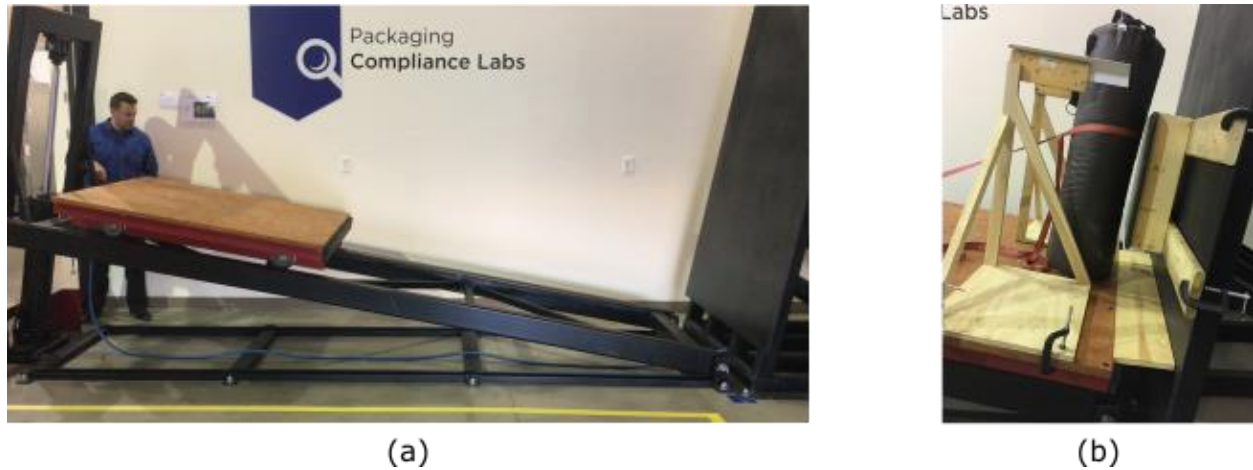
Figure 26: Pilot study testbed (a) sled and (b) setup.

The impact was evaluated using video photography and accelerometer data. A high-

speed camera and high-resolution cell phone recorded each test for comparison. A total of

three accelerometers were placed on the punching bag. Two of the sensors were identical and

capable of capturing accelerations up to 200 G's. These began recording at the moment of

impact.

The third sensor was part of a 10 degrees of freedom breakout board and only capable

of measuring accelerations up to 15 G's. This sensor and its accompanying components were

used to measure the bag's orientation and acceleration. Data from the breakout board was only

collected before the sled was released and up to 750 ms into its descent. One high-G sensor

and the breakout board were placed below the top edge of the grill. The remaining sensor was

placed above the top edge. All sensors were located on the opposite side of the bag from the

impacting face. An image of the sensors attached to the bag is provided below.
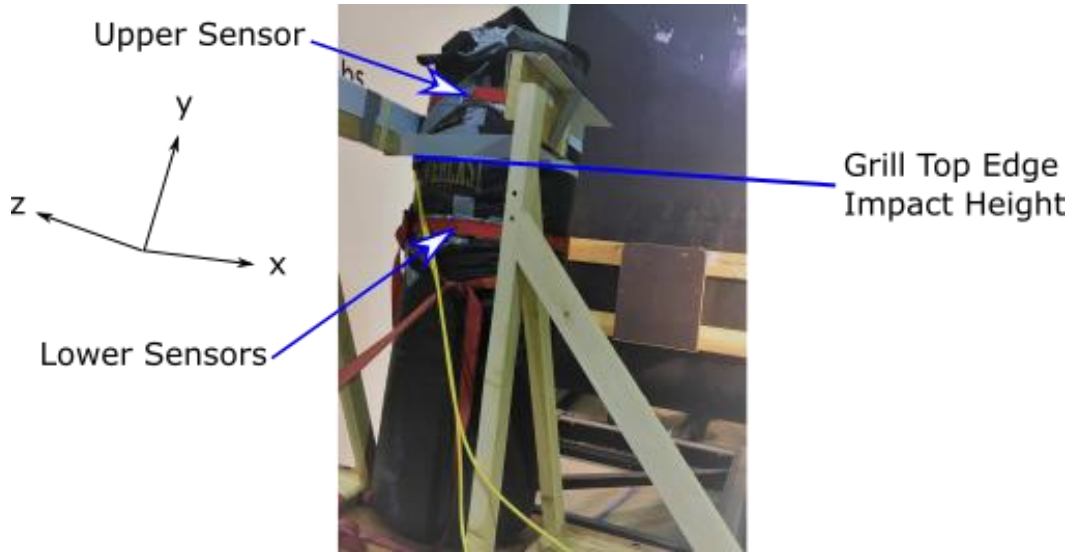
Figure 27: Sensor placement on punching bag.

The pilot study consisted of five different tests that were each run twice. The first test

was only the punching bag and established a reference for an unprotected pedestrian. For the

second test, a plank of wood was attached to the front of the bag and impacted the grill first.

The board was 3/8 of an inch thick by 3 inches wide by 16 inches long and expected to fail

under this impact scenario. The third test replaced the wood plank with a ¼ of an inch thick

6061 aluminum alloy plate. The material properties and geometry of the metallic plate were

expected to withstand the impact forces without surpassing the elastic region. The fourth test

utilized the same aluminum plate with the addition of an impact absorbing pad. The PORON

XRD pad was placed between the aluminum plate and punching bag. This test produced data

for direct comparison to test number three and was expected to reveal a significant decrease of

impact forces. The fifth test was performed using the ScarabSpine and Viper Pro device. This

final test was a preliminary assessment of the device's strength under impact. All results were evaluated and revealed consistent data between the two runs of each of the five tests. The results supported proceeding to testing at full target velocity.

Phase three was conducted at GVSU by constructing a drop test in a design bay with 30 ft ceilings. This test was designed to validate the ScarabSpine at the target impact velocity of 20 mph. Drop tests using only the bag, the bag and aluminum plate, and the bag and aluminum plate with the PORON XRD pad were completed before testing the ScarabSpine device. These initial tests were evaluated to ensure the sensors were capable of collecting the developed accelerations. Finally, the ScarabSpine and Viper Pro device was attached to the bag and dropped from 160 inches above the wooden grill.

Suspending the human model was achieved by fastening an eye bolt to an I-beam (Figure 28a) and placing it on the second floor balcony (Figure 28b) of the Keller Engineering Labs at GVSU. A long strap was run through the eye bolt and attached to a U-joint. Straps were attached to the bag and tied to a ring suspended above the bag's center of mass. A pin was slid through one side of the U joint into the ring and out the other side of the U joint (Figure 28c). The strap was then used to hoist the bag to the appropriate height. Quick removal of the pin released the bag initiating the drop test. The full test setup is depicted in Figure 28d. A forklift was used to secure the wood grill on the floor. Data was collected for a total of six tests. The three initial unique tests were performed first followed by three consecutive tests of the ScarabSpine.
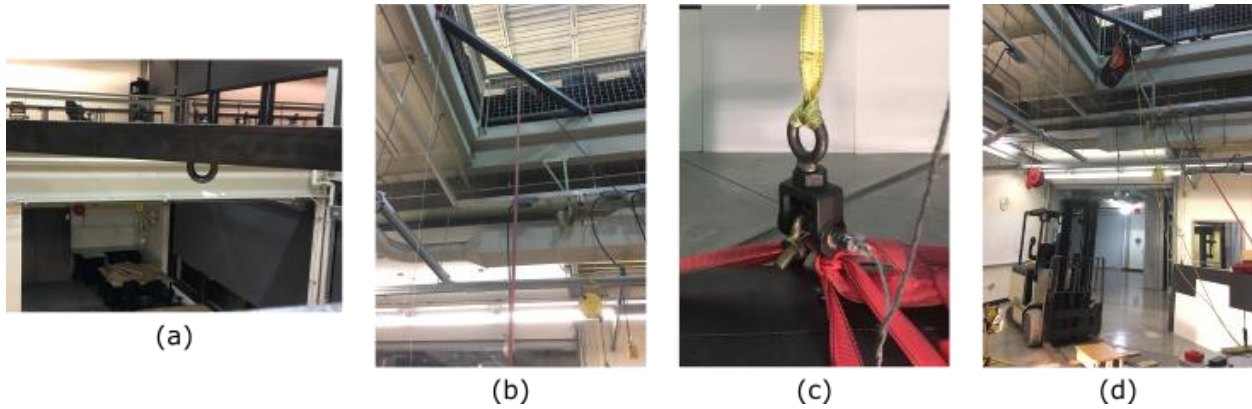
Figure 28: Drop test setup (a) eye bolt and I-beam, (b) hoisting strap, (c) quick disconnect, and (d) full setup.

3.7 Data Acquisition and Analysis

A total of three accelerometers and two video cameras were used to document each test. The sensors were driven by a single Arduino Mega microcontroller (Figure 29), which also recorded their measurements. All hardware specifications are provided in Appendix C. Of the three sensors, there were two unique models. The first was part of an Adafruit 10 degrees of freedom breakout board.
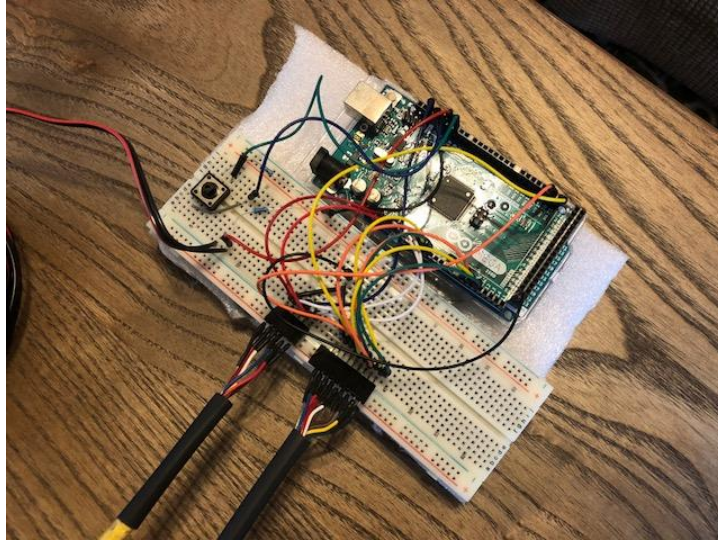
Figure 29: Arduino Mega wiring to sensors and LED.

The full breakout board included three devices, see Figure 30. The first was an accelerometer and magnetometer with model number LSM303DLHC. The second device was a gyroscope with model number L3GD20. The final device was a barometer with model number with BMP180. The accelerometer was only capable of measuring values from -15 G's to +15 G's. It was also limited to a sample rate of 200 Hz, i.e. 1 reading per 5 ms. The breakout board was placed on the punching bag to record its initial orientation and accelerations leading up to the impact. Orientation of the sensor was checked in real time before continuing with any test. The low sample rate and limited range required an additional sensor to capture the accelerations during physical contact.

Figure 30: Adafruit 10 DOF breakout board.

The second sensor used to monitor the impact scenario was an Adafruit 3-axis high-G

analog accelerometer with model number ADXL377, see Figure 31. It was rated for

accelerations ranging from -200 G's to +200 G's. The Arduino Mega collected and recorded

measurements from this sensor at 2,000 Hz. This rate produced a minimum of thirty samples in

a 15 ms time span, effectively capturing the accelerations developed during impact. The

Arduino was also wired with a red LED to indicate the moment recording began.

Figure 31: Adafruit ADXL377 accelerometer.

Illumination of the LED allowed video footage of individual tests to be paired with their respective acceleration data. Each test was filmed with a high-speed camera and iPhone with slow motion capabilities. The high-speed camera captured footage at 420 frames per second. This rate documented the motion of the human model with a time step of 2.38 ms, over six times faster than the assumed impact time. The high-speed camera was over 10 years old, which affected its capturing quality. Therefore, additional video was collected with the iPhone at 240 frames per second. This higher resolution footage supported the high-speed camera and clearly showed the illumination of the LED indicator.

The pilot study impact data was analyzed first. Accelerations for all three axes and the instantaneous time of each reading was recorded for the sensors below and above the top edge of the grill. The developed Arduino code to record this event is provided in Appendix C. The data for each test was imported into Microsoft Excel for evaluation. The vector magnitude of all three axes was calculated for each time point. In several cases the snapping of the restraining tape created noise in the x-axis. This interference and any additional noise within the cables contributed to a calculated percent error.

The video footage was linked up with the data to estimate the actual impact time for the model's velocity to reach zero, the point just before rebounding. The approximated time was used as a starting point to find the measured time and average acceleration. The measured time was found by calculating the area under the acceleration versus time curve. This area represented the change in velocity and was approximated using the trapezoidal rule numerical integration method. In this case, the velocity was directionless due to initially calculating the magnitude of the acceleration and resulted in an approximation using the scalar value of speed.

73

The time taken to reach a speed of zero was when the change in speed equaled the testbed's

calibrated impact velocity of 6.5 mph. This impact velocity neglected air resistance and was

assumed based off the testbed's geometry. The average and peak accelerations for this time

interval were recorded for comparison.

The pilot study also provided measurements necessary to understand the properties of

the punching bag and added protective plates for the complete impact scenario. The total

impact time was graphically determined using Microsoft Excel. The lower sensor impact time

was assumed complete once the z-axis values dropped below 1 G for longer than 10 ms. The

complete impact time for the upper sensor was considerably more complex and was

determined for individual tests. In general, the impacts were completed between 55 ms and

60 ms because of an extended "whiplash" effect. However, the sled also impacted the backstop

around the same time generating an excessive amount of noise. Once the times were selected,

the area under the curve method was used a second time to find the total change in speed.

The complete change in speed for each test configuration was used to calculate an

acting rebound coefficient. The resulting value for each test was not a traditional coefficient of

restitution because the direction of acceleration for each component was lost by calculating the

vector magnitude. Manipulating the equation for the coefficient of restitution resulted in an

equation for the rebound coefficient, see Equation B.20. This rebound coefficient was relatable

to the final drop tests and was used to calculate a theoretical average acceleration for each

configuration, including the ScarabSpine.

Evaluation of the drop test data was also completed using Excel. All acceleration values and time stamps were imported and graphed. The full vector magnitude for each time step was calculated and used for area approximation. The video footage and trapezoidal rule method were used again to approximate the impact time for each test to reach the pre-rebound pause, a change in speed of 20 mph. As before, the initial impact velocity neglected air resistance and was based off initial drop height calculations. The average acceleration for this time interval was calculated and compared across all drop tests. The average acceleration for the total impact time was also calculated and compared to theoretical values calculated using the pilot study acting rebound coefficients for respective tested configurations.

4 Results and Discussion

4.1 Transient FEA

Finite element analysis of the ScarabSpine system provided initial support for its

geometrical design and material selection. The first demonstration of its strength was

quantified through deflection. In the allotted 15 ms the bottom segment traveled 2.64 inches,

see Figure 32. The maximum deflection between the top and bottom segment was found to be

1.13 inches. This deflection was well within the previously specified dynamic range.
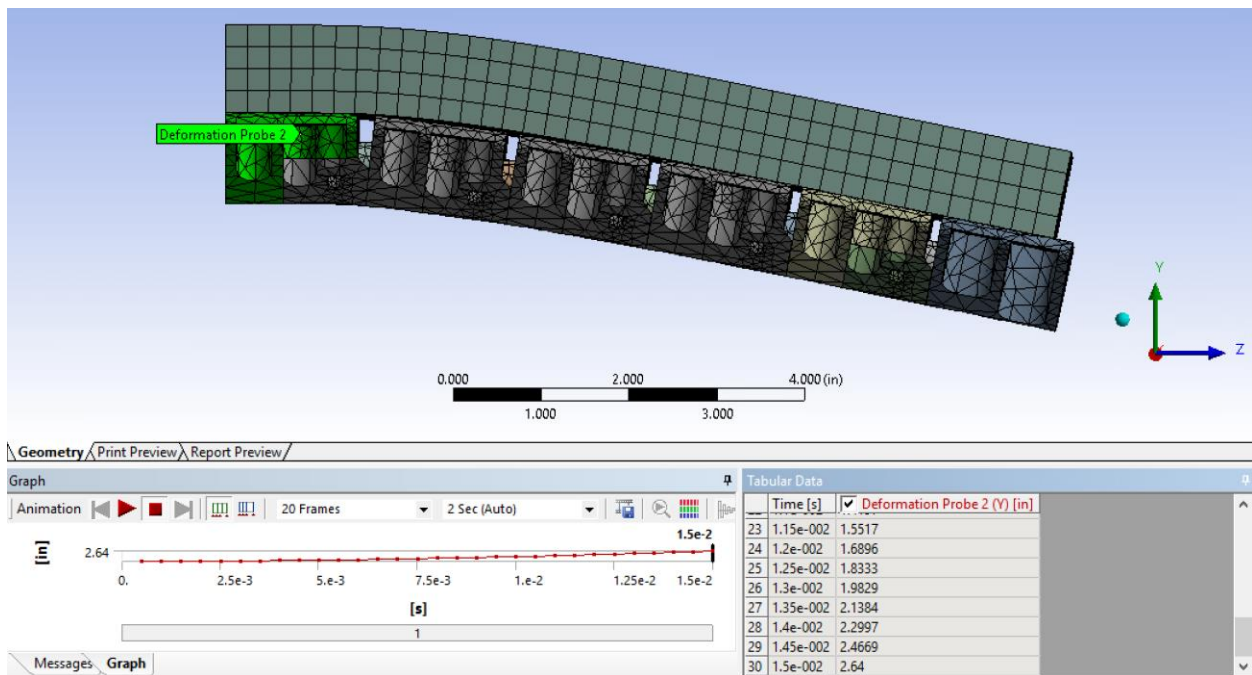
Figure 32: Distance travelled by the bottom aluminum segment.

The maximum equivalent stress developed within the ScarabSpine remained below the

ultimate tensile strength of both materials, see Figure 33. This stress was larger than the yield

strength indicating the materials will plastically deform but should not fail. Additionally, the

point of maximum stress occurred at a sharp edge which is indicative of a singularity and could

be alleviated by adding fillets.
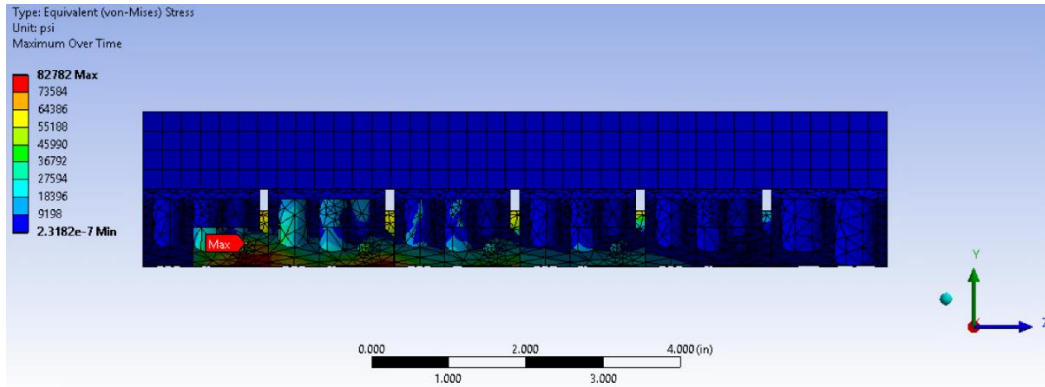
Figure 33: Maximum equivalent stress in ScarabSpine FEA.

The ball studs were identified as the most critical failure point being the only connection

between segments. They experienced a maximum equivalent stress of 79,244 psi (Figure 34)

resulting in a minimum safety factor of 1.22 with respect to the ultimate tensile strength of 304

stainless steel. Based on this analysis the ScarabSpine would deform with a deflection within

specification without catastrophic failure. The results supported the material selection and

geometrical design of the ScarabSpine and lead to the testing of a prototype.
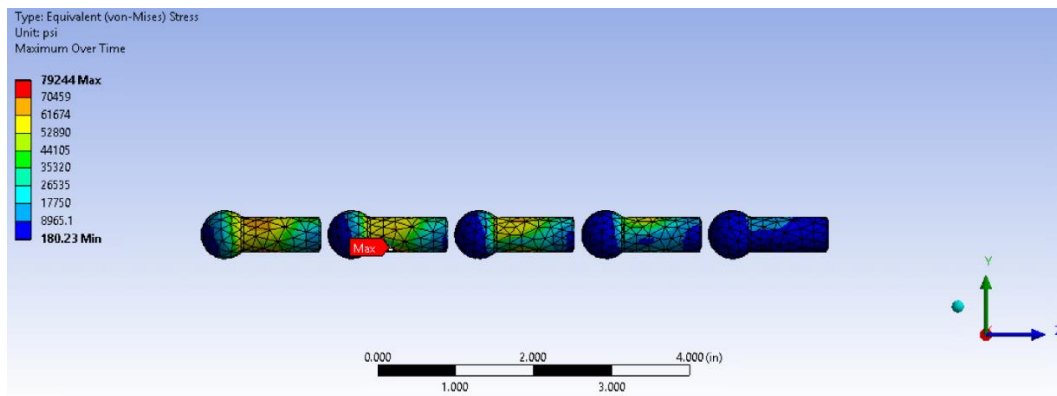
Figure 34: Maximum equivalent stress in ball studs during ScarabSpine FEA.

4.2 Pilot Study

The pilot study was divided into two rounds. Both rounds included a single test for the following human model configurations: model only, model with wooden plank, model with aluminum plate, model with aluminum plate and PORON XRD pad, and model with ScarabSpine and Viper Pro pad.

4.2.1 Human Model Only

The first and base test was the solitary human model shown in Figure 35.

Figure 35: Pilot study human model configuration setup.

The configuration was released from the depicted position and acceleration measurements were recorded during the impact. Lower sensor accelerometer measurements for both rounds of human model testing are graphically displayed in Figure 36.
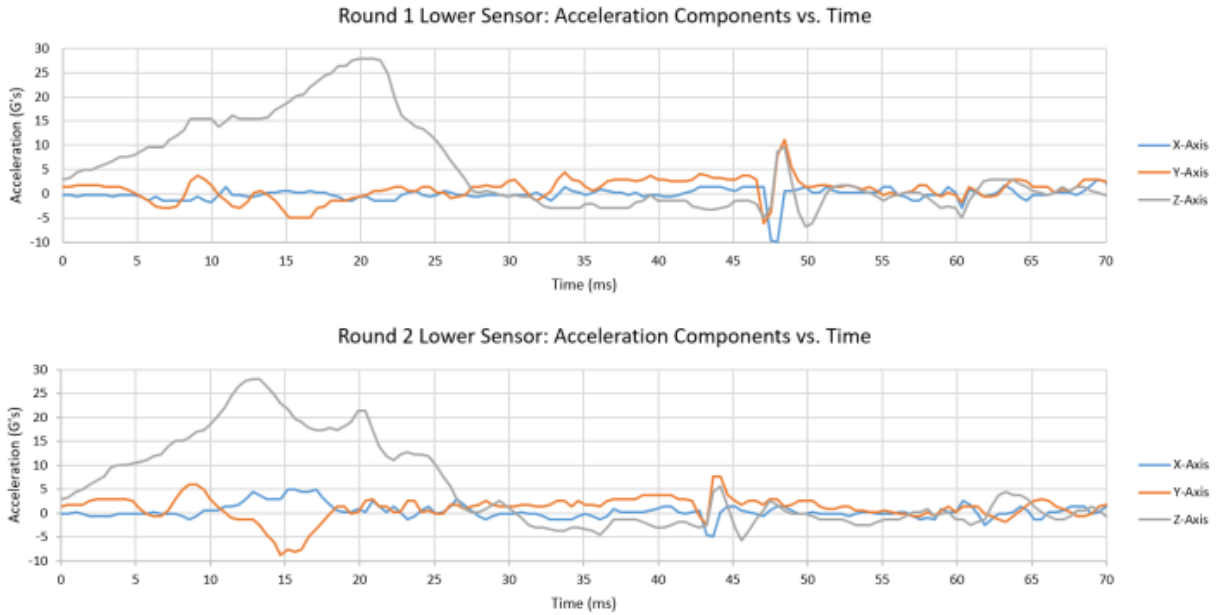
Figure 36: Pilot study lower sensor acceleration measurements for human model.

The z-axis was the largest contributing component because it was aligned with the direction of travel. The sharp peaks appearing in both graphs between 42 ms and 52 ms indicated the breaking of the restraining tape. In both rounds the rebound of the lower sensor was completed before the induced noise. Additional notable interference was recognized beginning around 57 ms in round 1 and 59 ms in round 2. This was due to the sled impacting the backstop of the testbed and was apparent in all pilot study tests.

The upper sensor also captured both interfering events. Due to a longer impact time, the sensor did not complete a rebound cycle until after the tape snapped. The developed accelerations resembled a whiplash affect and are graphically displayed in Figure 37.
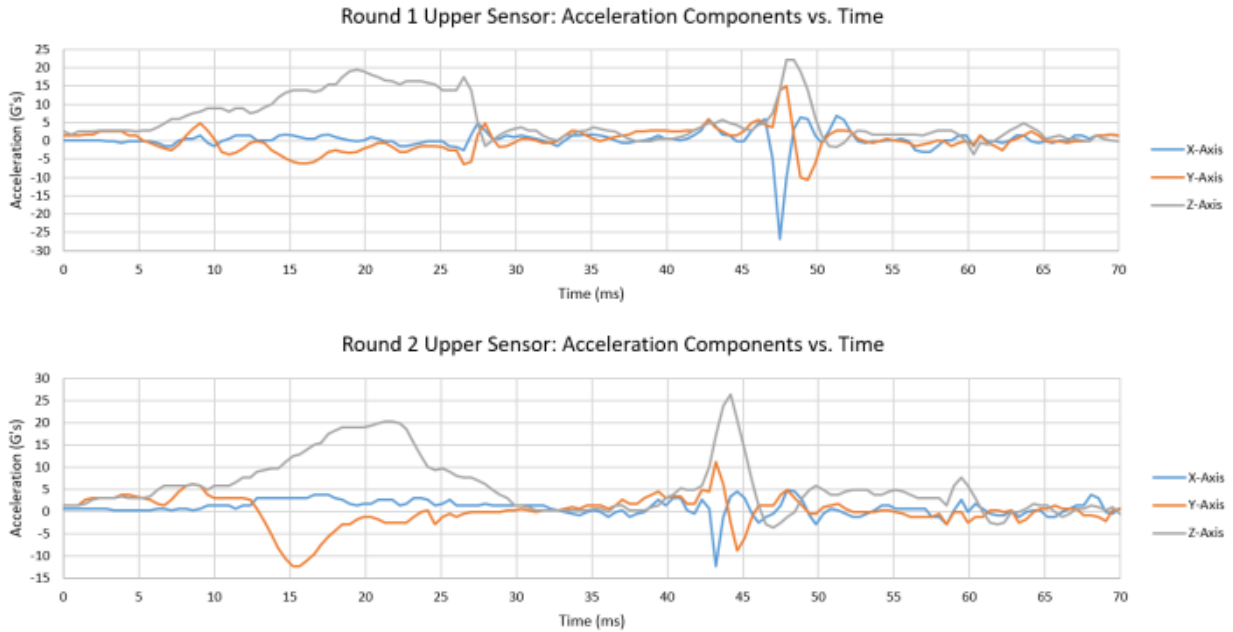
Figure 37: Pilot study upper sensor acceleration measurements for human model.

The lack of support for the top portion of the human model allowed the upper segment to fold over the top edge of the impacting grill (Figure 38). The upper sensor came to a stop, indicated by the prolonged nearly zero or slightly positive z-axis measurements, and then continued to accelerate in the positive direction. The restraining tape may have slightly prolonged the upper sensor's rebound. This model reflects the accelerations for an unsupported upper segment for the purposes of this pilot study.

Figure 38: Unsupported upper segment of human model folding on top of wooden grill.

The instantaneous vector magnitudes were calculated for both sensors using all three components to account for misalignments during setup. The resulting graphs are illustrated below.
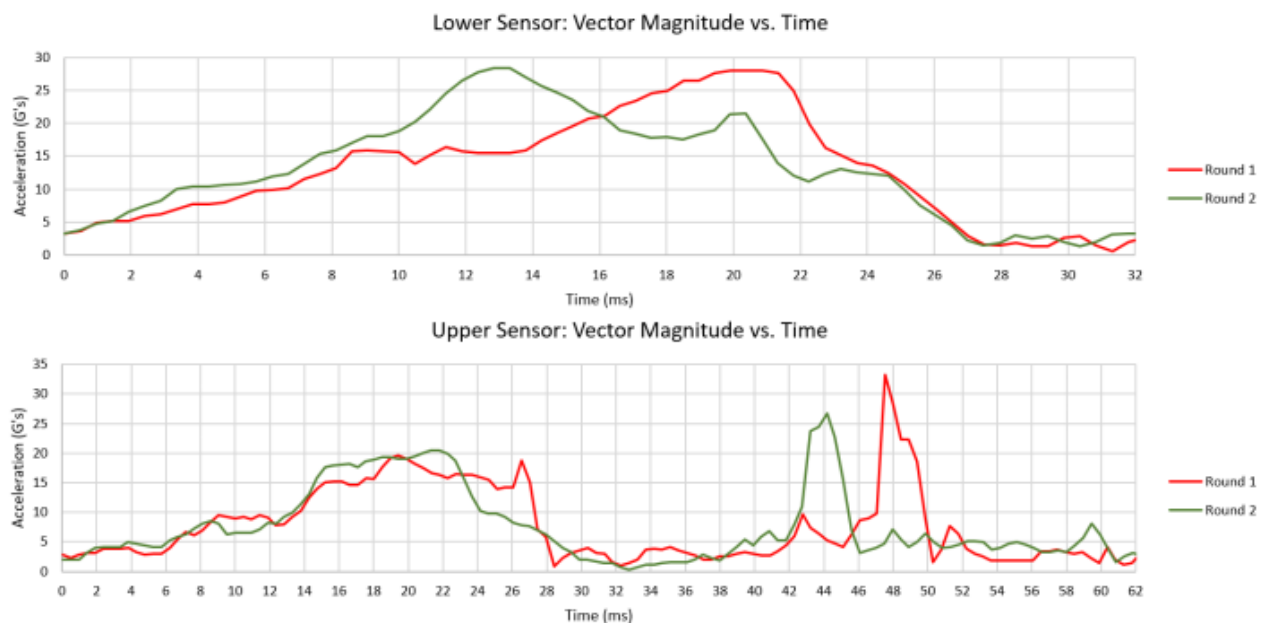
Figure 39: Pilot study vector magnitudes for both sensors during human model testing.

81

The lower segment's average times to reach zero speed and total rebound were 19 ms and 31 ms, respectively. Change in velocity in the z-axis was graphed to illustrate these times from the assumed initial impact of 6.5 mph (114 in/s), see Figure 40. The average of instantaneous acceleration magnitudes for these time periods were calculated to be 15.5 G's and 13.5 G's, respectively. The resulting lower segment rebound coefficient for both rounds equaled 0.43, as calculated using the process discussed in section 3.7. The upper sensor recorded appreciably longer impact times and smaller average accelerations.
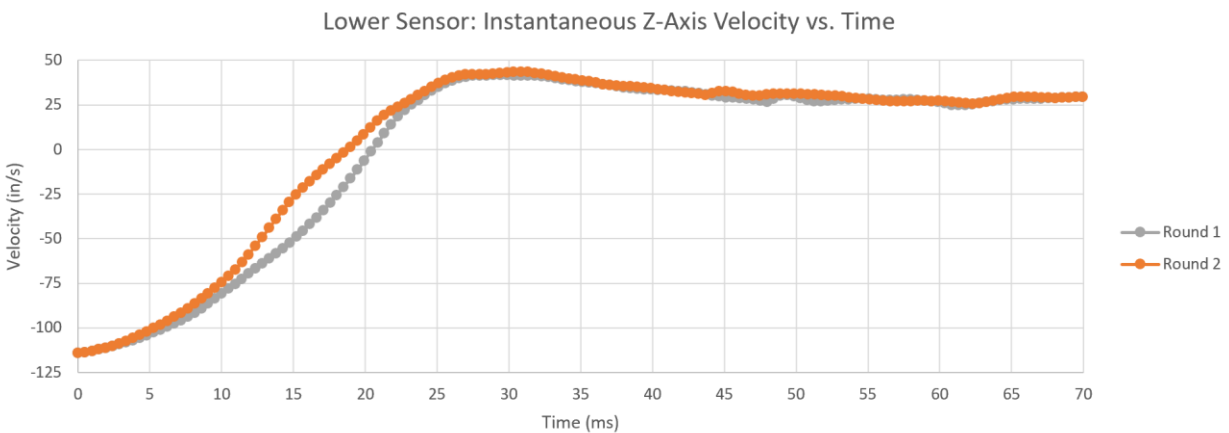
Figure 40: Pilot study instantaneous velocity of the lower segment.

The average measured time for the upper segment to reach the pre-rebound pause was 27 ms and the impact was complete by approximately 60 ms. The velocity response of the upper segment shows it reaching a zero velocity around the same time the lower segment has rebounded, see Figure 41. The average acceleration for each time interval was 10.7 G's and 7.8 G's, respectively. The average rebound coefficient was 0.61. Individual measurements and calculated values for each round are provided in Table 5 and in the Appendix.
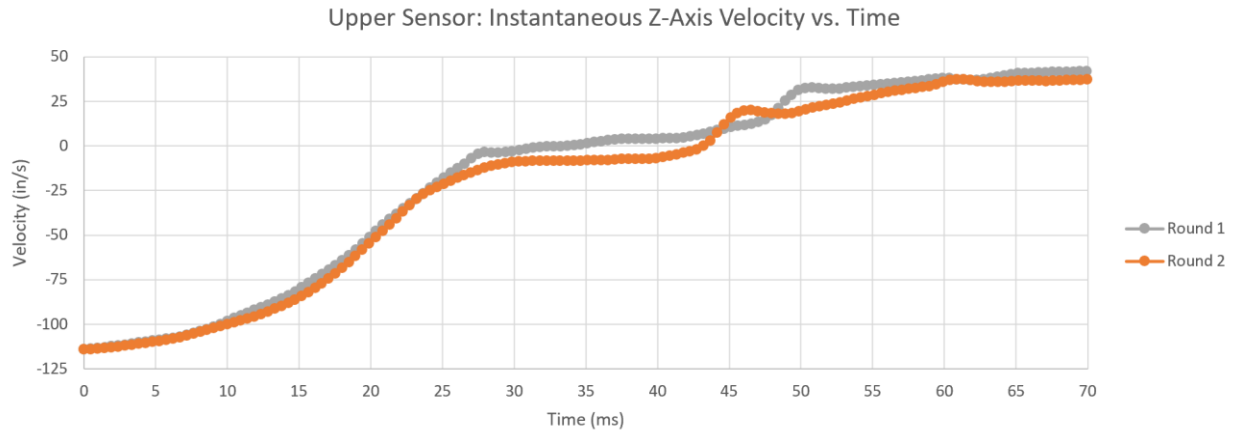
Figure 41: Pilot study instantaneous velocity of the upper segment.

Table 5: Pilot study human model only results.

	Round	Impact Time (ms)		Rebound Coefficient	Average G's		Peak G's
		V->0	Total		V->0	Total	Excluding Tape
Lower Segment	1	19.9	31.3	0.43	14.6	13.1	28.0
	2	18.0	30.3	0.43	16.4	13.8	28.4
Upper Segment	1	27.0	59.9	0.61	10.8	7.9	19.6
	2	27.5	60.9	0.60	10.6	7.7	20.5

The large discrepancy between upper and lower segment accelerations was attributed to the absence of support for the upper portion of the human model. The reaction demonstrated the hyperextension motion this research was determined to prevent. Ideal results would lower the average acceleration making the upper and lower segments comparable. Similar upper and lower readings would also indicate minimal deflection between the two segments. A wooden plank was the first material added to the human model to record its effect on the system.

4.2.2 Human Model with Wood Plank

The human model with wooden plank configuration was tested under the same

conditions. Each round was conducted with a new plank of equal dimensions and cut from the

same board. A picture of the configuration is shown in Figure 42.
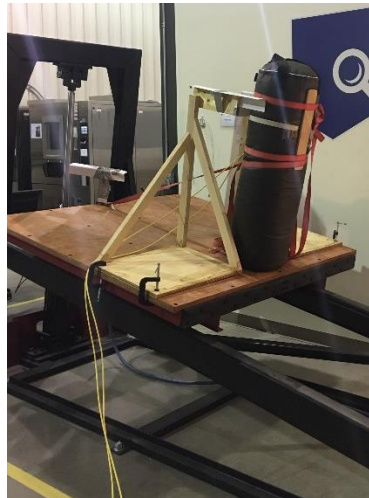
Figure 42: Pilot study human model with wood plank configuration setup.

The model was released from the illustrated position and impacted the same wooden

grill. During testing, the plank in round 1 cracked and the plank in round 2 was undamaged. The

designed repeatability between tests resulted in the assumption that the non-uniform structure

of the wood planks allowed different outcomes for the same test. The resulting lower segment

acceleration components for both rounds were graphed with respect to time (Figure 43).
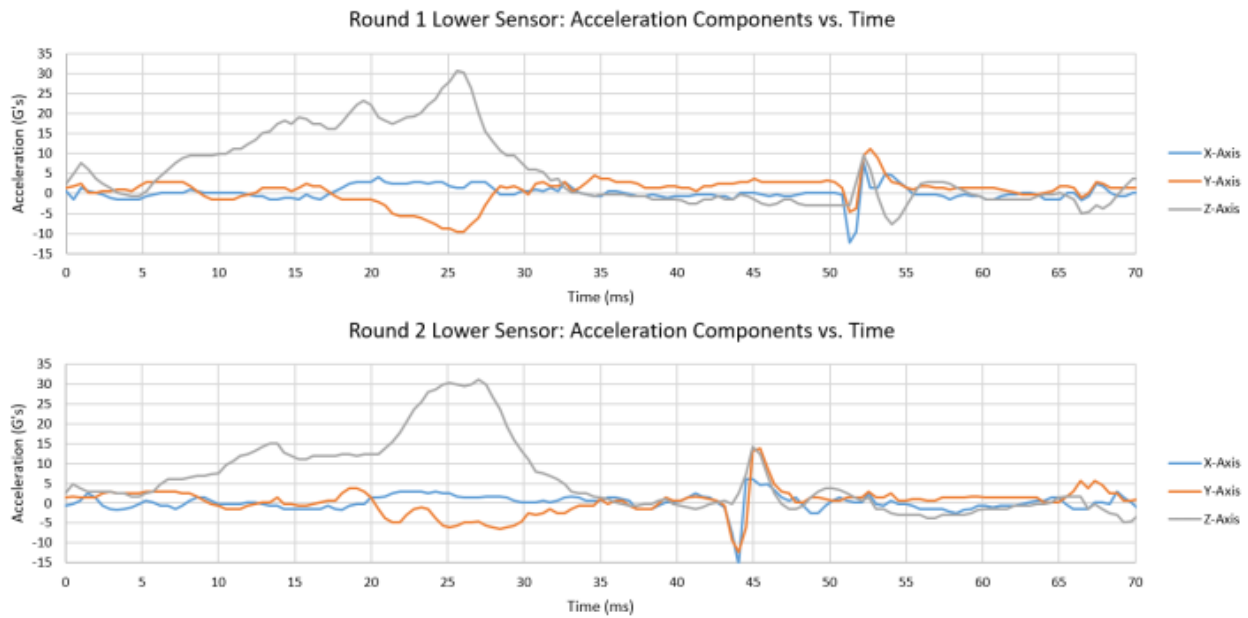
Figure 43: Pilot study lower sensor acceleration measurements for human model with wood plank.

The lower sensor's wave forms were comparable with minor dissimilarities surrounding the release of the restraining tape. The tape snapped later in round 1 because the plank broke during impact. This allowed the z-axis values to become negative for a period longer than 10 ms, completing the rebound cycle. Round 2 showed the tape snapping around 43 ms and the z-axis component remained below 1 G for approximately 8 ms. The rebound cycle was assumed complete despite being 2 ms below the predetermined criteria. The upper sensor graphs showed more distinct differences throughout the impact, see Figure 44.
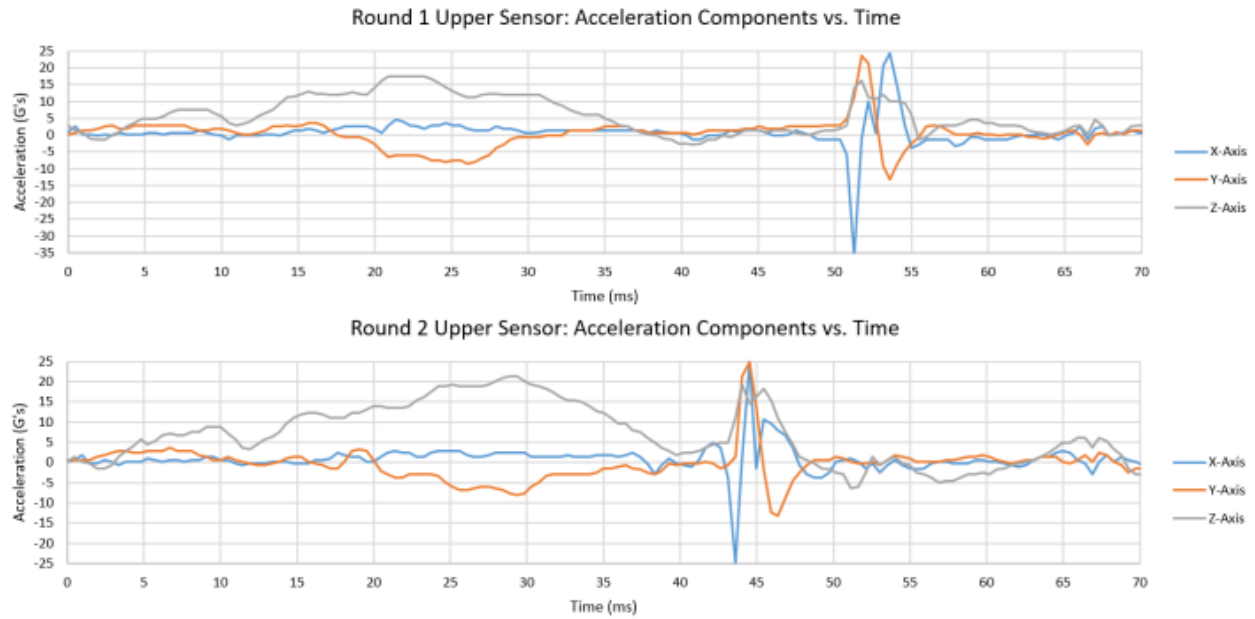
Figure 44: Pilot study upper sensor acceleration measurements for human model with wood plank.

Round 1 z-axis values dropped below 1 G after 37 ms until the tape released at 51 ms. The z-axis component then spiked positive followed by a shallow slope back to 0 G's around 64 ms. This wave form was similar to the solitary human model results but displayed a significantly longer impact time. Round 2 measured the tape snap before the initial impact dropped below 1 G. The spike was then followed by negative z-axis values lasting approximately 15 ms and a positive inflection for approximately 5 ms. The post-snap negative wave form was attributed to the "whiplash" period being impacted by an undampened deflecting plank. This unique difference was also observed in future configuration results. The instantaneous vector magnitudes were graphed for both sensors for further comparison, see Figure 45.
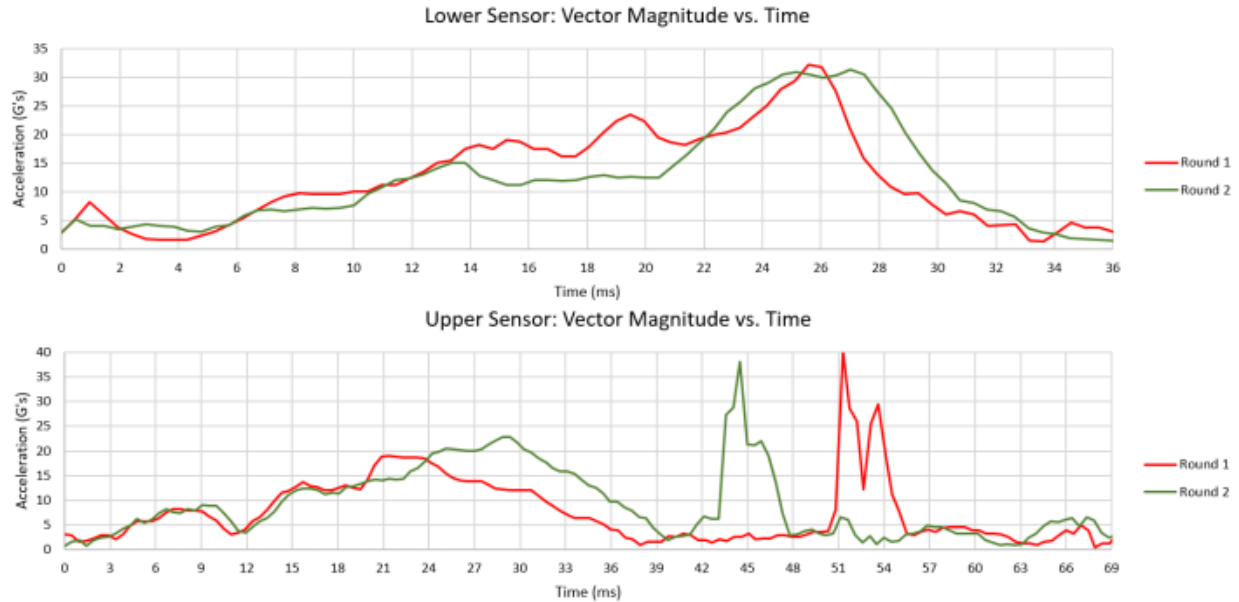
Figure 45: Pilot study vector magnitudes for both sensors during human model with wood plank testing.

The average times between rounds for the lower segment to reach zero velocity and total impact were 25 ms and 34 ms, respectively. The average acceleration for these time intervals were 12.2 G's and 12.8 G's, respectively. The resulting average rebound coefficient was 0.48. The impact times were slightly longer than the previous solitary human model tests resulting in lower average accelerations.

Upper segment results were only comparable to the moment the model's speed reached zero. This point occurred at 29 ms and 28 ms and resulted in an average acceleration of 10.1 G's and 10.5 G's for round 1 and 2, respectively. Round 1 total impact time and its respective average acceleration was 63 ms and 8.1 G's. Round 2 total impact time and its respective average acceleration was 69 ms and 9.2 G's. The rebound coefficients for the two rounds were 0.73 and 1.13, respectively. The inconsistent results and fragility of the wood plank

limited its testing to only the pilot study. Impact times and segment accelerations for each

round are provided in Table 6 and in the Appendix.

Table 6: Pilot study human model with wood plank results.

| | Round | Impact Time (ms) | | Rebound Coefficient | Average G's | | Peak G's |
		V->0	Total		V->0	Total	Excluding Tape
Lower Segment	1	23.7	33.1	0.49	12.5	13.1	32.2
	2	25.6	35.5	0.47	11.9	12.4	31.4
Upper Segment	1	29.3	63.1	0.73	10.1	8.1	19.0
	2	28.4	68.8	1.13	10.5	9.2	22.9

Compared to the human model only testing, adding the wood plank increased all impact

times and decreased the average acceleration for both segments to reach zero velocity. The

calculated rebound coefficient was larger for the wood plank indicating a larger change in

velocity. For this reason, average accelerations for the total impact time were similar to the

human model only testing. It was also noticed that the peak accelerations for the wood plank

were larger.

4.2.3 Human Model with Aluminum Plate

The wood plank from the previous model was replaced with an aluminum plate for the

third configuration. Each round of testing was conducted with the same 6061 aluminum plate

because it did not plastically deform during testing. The lower sensor components were

graphed for visual comparison between round 1 and round 2, see Figure 46.
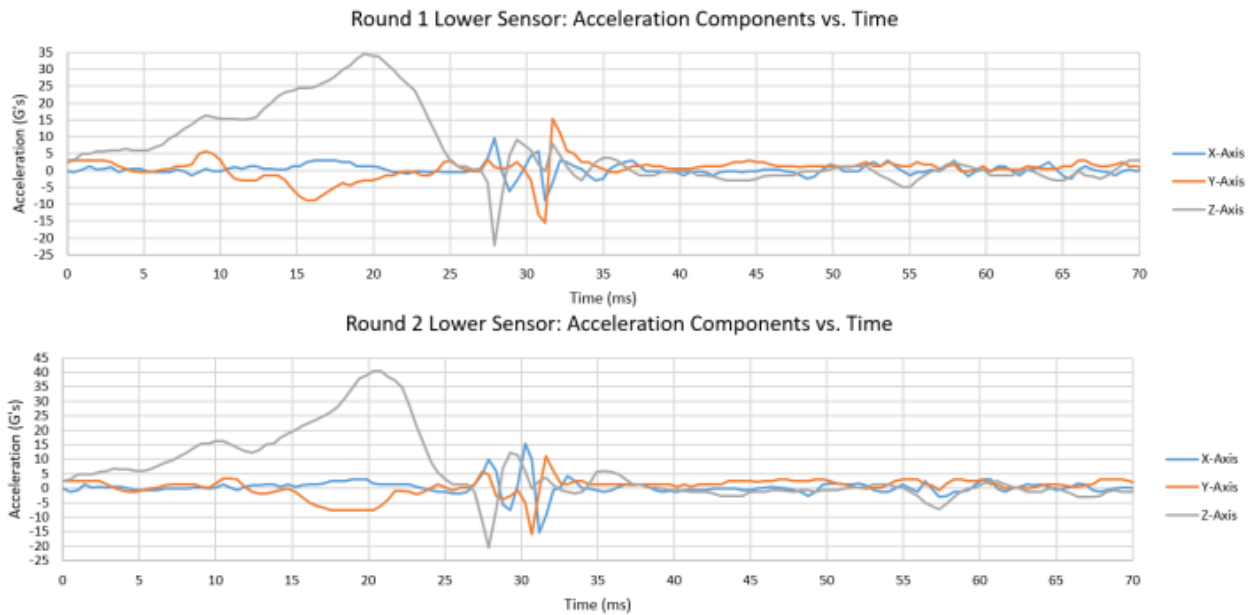
Figure 46: Pilot study lower sensor acceleration measurements for human model with aluminum plate.

Lower segment measurements from each round yielded similar waveforms. Noise from the restraining tape occurred directly after the initial rebound at approximately 27 ms in both rounds. Therefore, the total impact time included the snapping period. The earlier release was attributed to the added rigidity of the metallic plate. This reaction was also observed in the remaining two pilot study configurations. The upper sensor measurements for both rounds also included the developed noise, see Figure 47.
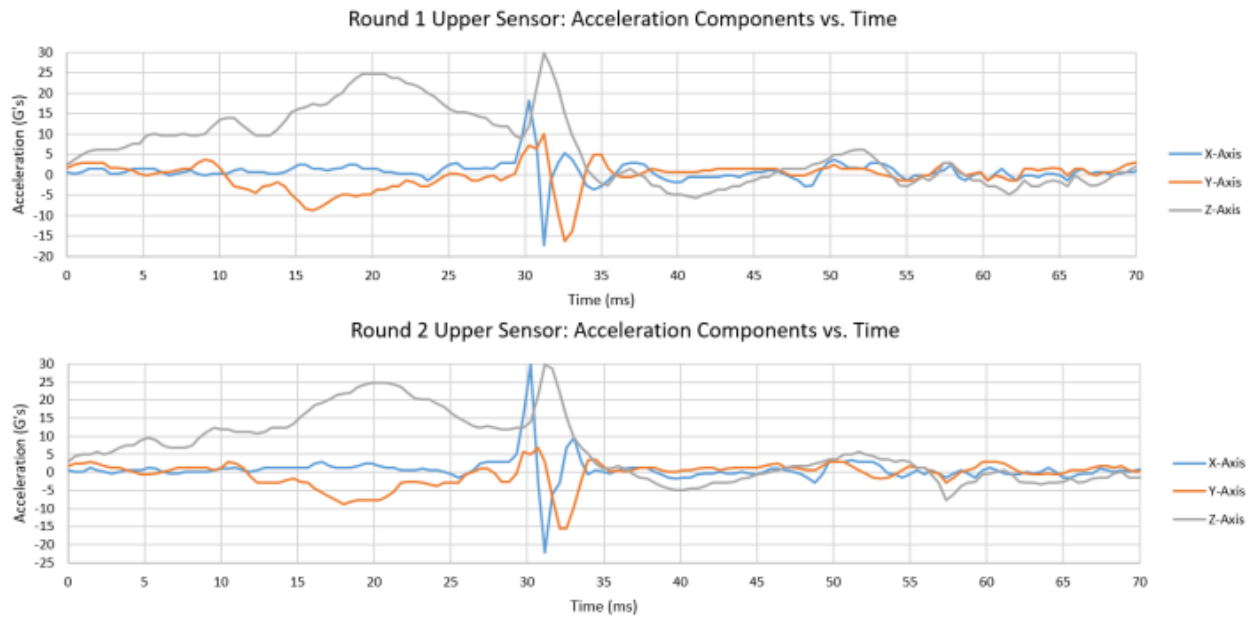
Figure 47: Pilot study upper sensor acceleration measurements for human model with aluminum plate.

The upper segment also experienced accelerations in both rounds that yielded consistent graphical wave forms. The impact in each round lasted approximately 36 ms. Both graphs then showed prolonged negative z-axis values followed by a positive inflection, consistent with round 2 of the wood plank model. The aluminum plate experienced elastic deflection that lead to a small "whiplash" event. The instantaneous vector magnitudes for both rounds were calculated and graphed for further analysis, see Figure 48.
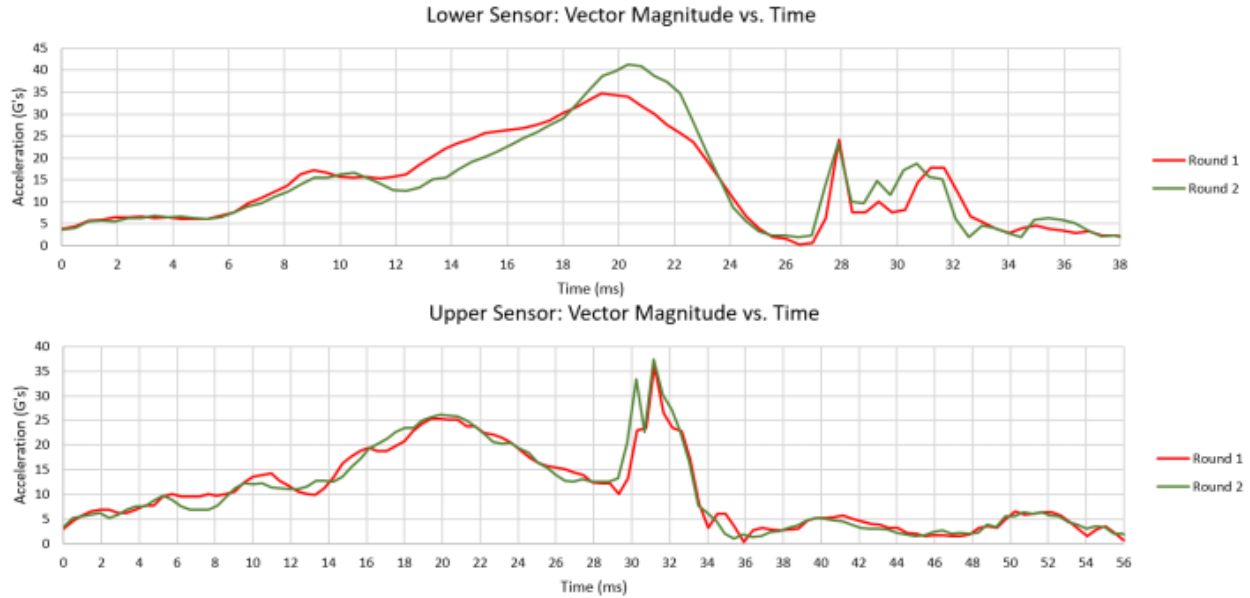
Figure 48: Pilot study vector magnitudes for both sensors during human model with aluminum plate testing.

The average time for the lower segment to reach zero velocity and total rebound was 19 ms and 38 ms, respectively. The resulting average accelerations were 15.5 G's and 14.1 G's for the respective time intervals. The average rebound coefficient was 0.80. The pre-rebound impact time and acceleration were comparable to the unprotected pedestrian configuration results, which supported the consistency of the testbed. The additional rigidity to the system was visible through the total impact values. The total time was longer because of an extended rebound period, and the experienced acceleration was higher because the upper segment could not fold over the wooden grill and hold on.

The average times for the upper segment to reach zero velocity and total rebound were 22 ms and 55 ms, respectively. The resulting average accelerations were 13.6 G's and 10.8 G's

for the respective time intervals. The average rebound coefficient was 1.00. Impact times and experienced accelerations for both segments are provided in Table 7 and in the Appendix.

Table 7: Pilot study human model with aluminum plate results.

| | Round | Impact Time (ms) | | Rebound Coefficient | Average G's | | Peak G's |
		V->0	Total		V->0	Total	Excluding Tape
Lower Segment	1	18.9	36.9	0.79	15.6	14.1	34.8
	2	19.9	38.3	0.80	15.3	14.0	41.2
Upper Segment	1	21.7	54.1	1.01	13.6	10.9	25.3
	2	22.2	56.4	0.99	13.6	10.6	26.1

The added aluminum plate reduced the difference between segment pre-rebound and total impact times by 5.6 ms and 12 ms compared to the human model only test. This placed the segment impact times to within approximately 2.5 ms of each other before the rebound. The impact experience between segments was beginning to normalize. Just like the wood plank, the addition of the aluminum plate increased the rebound coefficient indicating a larger change in velocity than the sole human model. The peak accelerations were also significantly larger indicating the requirement of an impact absorbing element.

4.2.4 Human Model with Aluminum Plate and PORON Pad

A new 6061 aluminum plate with identical dimensions was placed with the impact absorbing pad for this configuration. The two materials were located at the same height as the previous test setup. Straps were placed across the plate in the same location to fix the protective materials to the human model. Figure 49 shows the model setup.
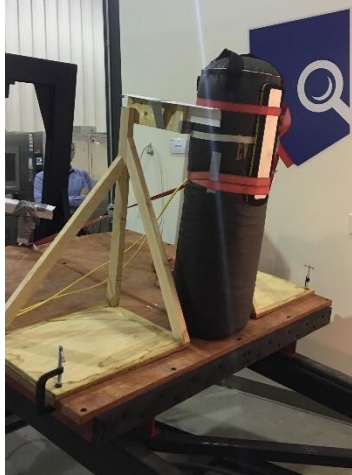
Figure 49: Pilot study human model with aluminum and PORON configuration setup.

Two rounds of testing were completed with this configuration. The lower sensor readings are graphically displayed in Figure 50.
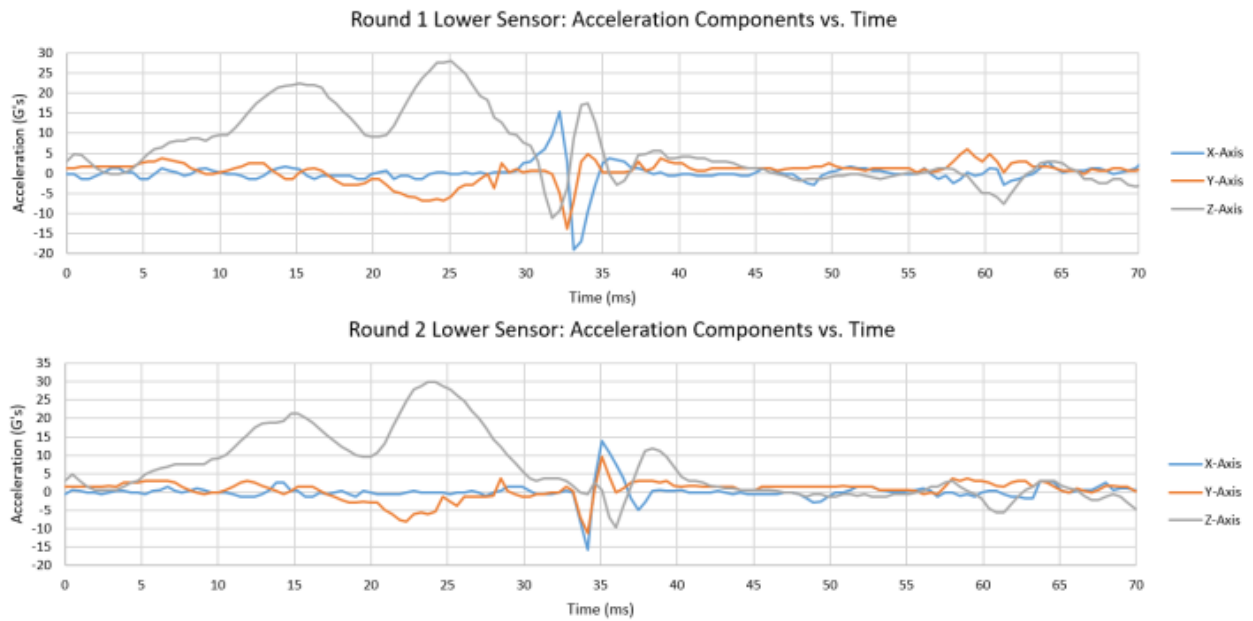
Figure 50: Pilot study lower sensor acceleration measurements for human model with aluminum plate and PORON pad.

Data from the two rounds displayed a comparable waveform. Both z-axis components demonstrated a dual peak curve followed by noise from the tape. Rounds 1 and 2 both reached zero velocity in 24 ms. After the noise a shallow slope of z-axis values decreased to 0 G's by 46 ms in round 1 and 44 ms in round 2. Compared to the aluminum plate model, the addition of the impact absorbing pad altered the z-axis waveform, increased the total impact time, and decreased peak instantaneous accelerations. The upper segment also displayed consistent results and improved impact attenuation, see Figure 51.
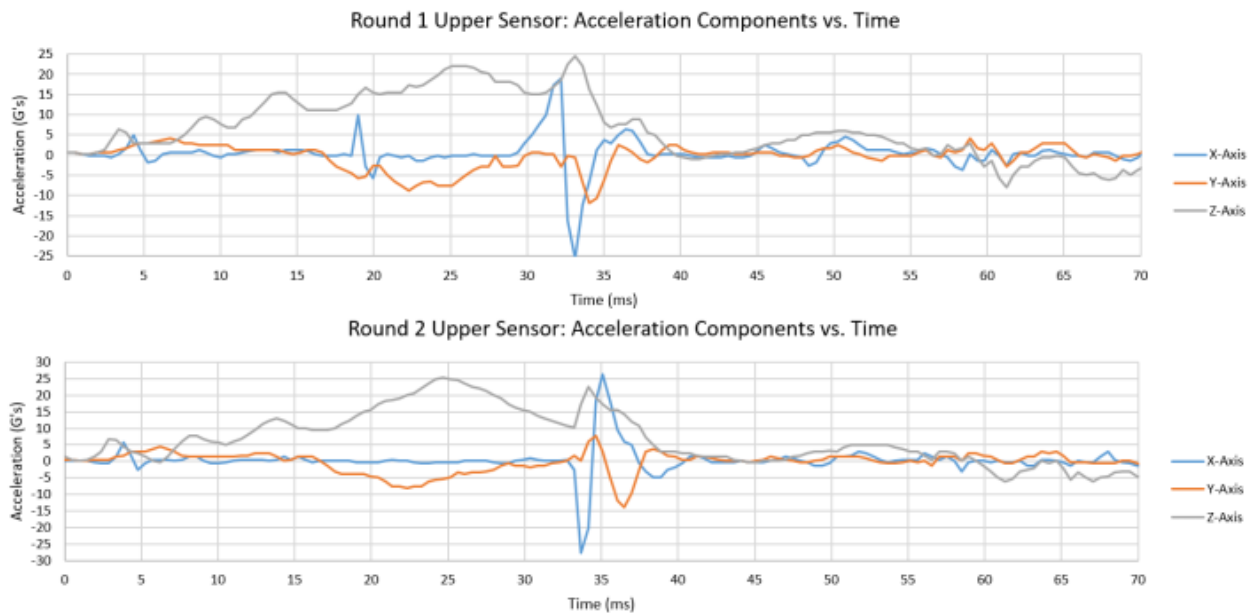
Figure 51: Pilot study upper sensor acceleration measurements for human model with aluminum plate and PORON pad.

The upper sensor's graphical waveform also exhibited key differences from the aluminum plate only configuration. The most significant was the absence of negative z-axis values after the tape snapped. This indicated the aluminum plate experienced decreased

deflection and the pad altered the transmitted forces during impact. The instantaneous vector

magnitudes were calculated for both segments and are graphically displayed below.
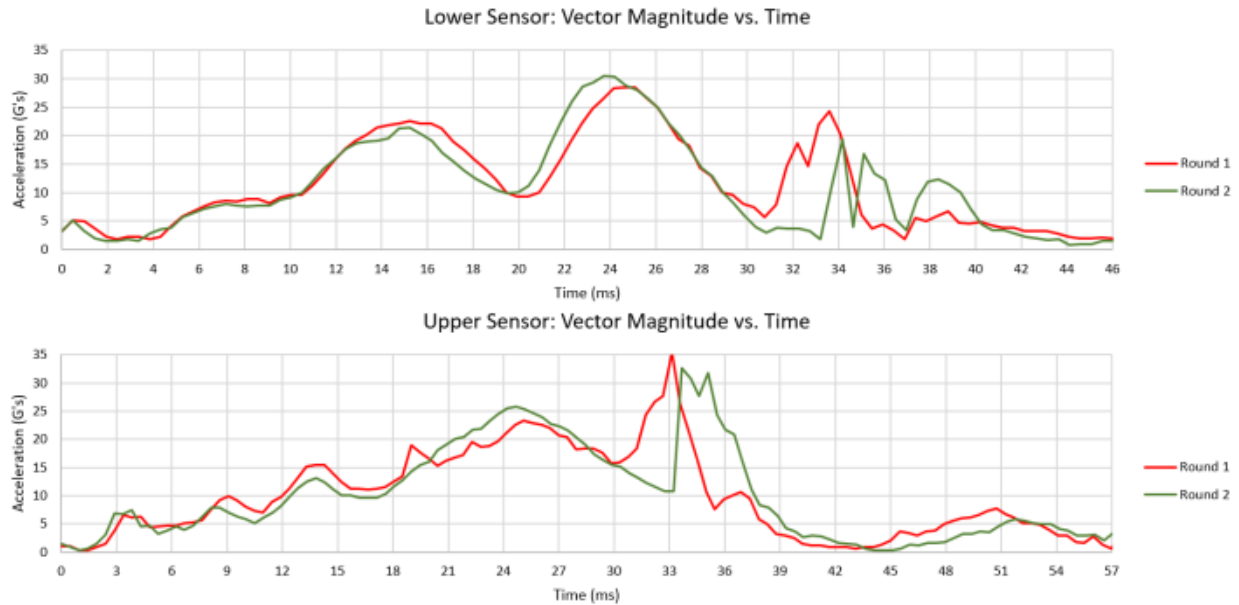
Figure 52: Pilot study vector magnitudes for both sensors during human model with aluminum plate and PORON pad testing.

The average times for the lower segment to reach zero velocity and total impact were

24 ms and 45 ms, respectively. These impact times were 4.8 ms and 7.7 ms longer than the

previous test. The resulting average accelerations were 12.5 G's and 11.3 G's for the two

respective time intervals. Addition of the pad decreased the calculated acceleration for each

time interval by approximately 3 G's. The average rebound coefficient was 0.71.

Upper sensor measurements were similar with 24 ms to zero velocity and 54 ms for

total impact. The total impact time for each segment only differed by 8.8 ms, lower than any

prior test. Accelerations were also similar at 12.4 G's and 10.5 G's for each time interval

respectively. The average rebound coefficient was 0.90. The accelerations experienced by both

sensors were within 1 G for each time interval while remaining below 13 G's. This was significantly lower than the aluminum model and displayed further normalization between segments. The impact times and acceleration levels for both segments are provided in Table 8 and in the Appendix.

Table 8: Pilot study human model with aluminum plate and PORON pad results.

	Round	Impact Time (ms)		Rebound Coefficient	Average G's		Peak G's
		V->0	Total		V->0	Total	Excluding Tape
Lower Segment	1	24.2	46.5	0.75	12.5	11.3	28.5
	2	24.2	44.1	0.67	12.6	11.3	30.5
Upper Segment	1	24.1	54.1	0.89	12.4	10.4	23.4
	2	24.2	54.2	0.92	12.3	10.5	25.8

Compared to previous testing, addition of the impact absorbing pad to the aluminum plate has resulted in the most favorable results. The average acceleration levels have been normalized between segments and are below the lower segment results for the human only and human model with aluminum plate models. The remaining area of improvement was to decrease the peak acceleration.

4.2.5 Human Model with ScarabSpine and Viper Pro Pad

The final pilot study test was completed using the developed ScarabSpine and Viper Pro pad. Proper alignment of the protective equipment placed the center of the ScarabSpine at the upper edge of the grill. A picture of the setup is provided in Figure 53.

Figure 53: Pilot study human model with ScarabSpine and Viper Pro configuration setup.

As before, the model was released from the starting position and the impact accelerations were recorded. After the first round the ScarabSpine was closely inspected for plastic deformation. No visible damage was apparent, and the model was reset for round 2. Lower segment acceleration measurements for both rounds are graphically displayed in Figure 54.
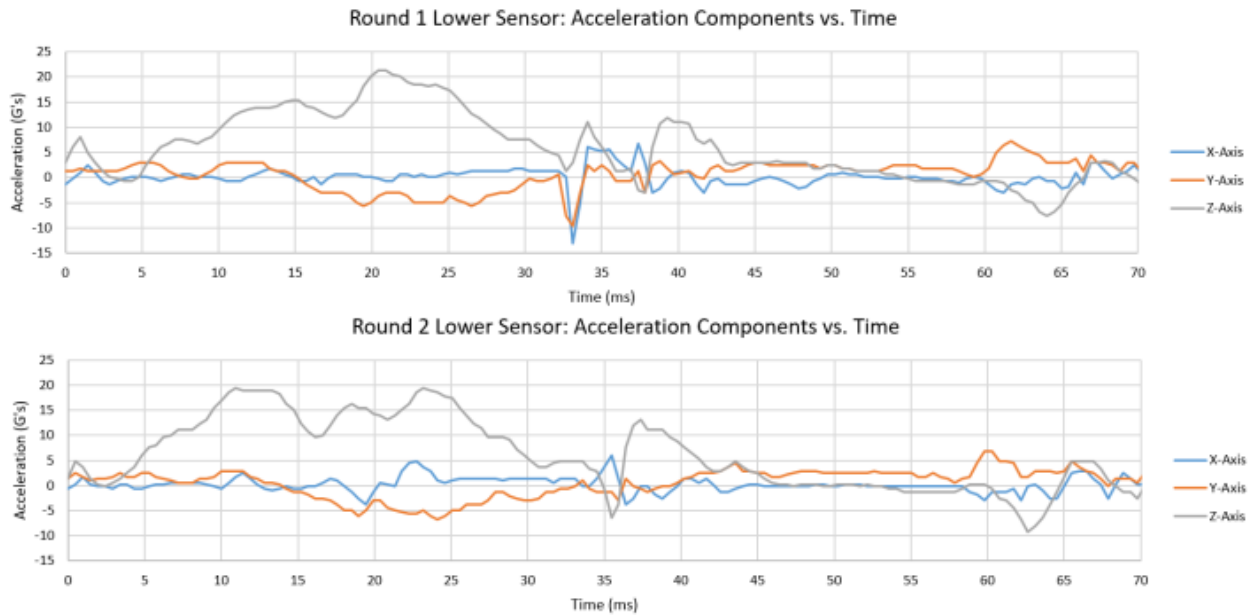
Figure 54: Pilot study lower sensor acceleration measurements for human model with ScarabSpine and Viper Pro pad.

The lower segment results displayed similar wave forms with minor variations. Both rounds resembled a double peak curve in the z-axis within the first 30 ms. This was similar to the aluminum plate and PORON pad model but with a decrease in peak acceleration by approximately 10 G's. After 30 ms, round 1 showed the expected tape snapping noise, which was not as apparent in round 2. This was explained through analyzing the video footage. It was observed that the tape in round 2 released from the fixture earlier than all other tests. The upper sensor data captured this event and is shown in Figure 55.
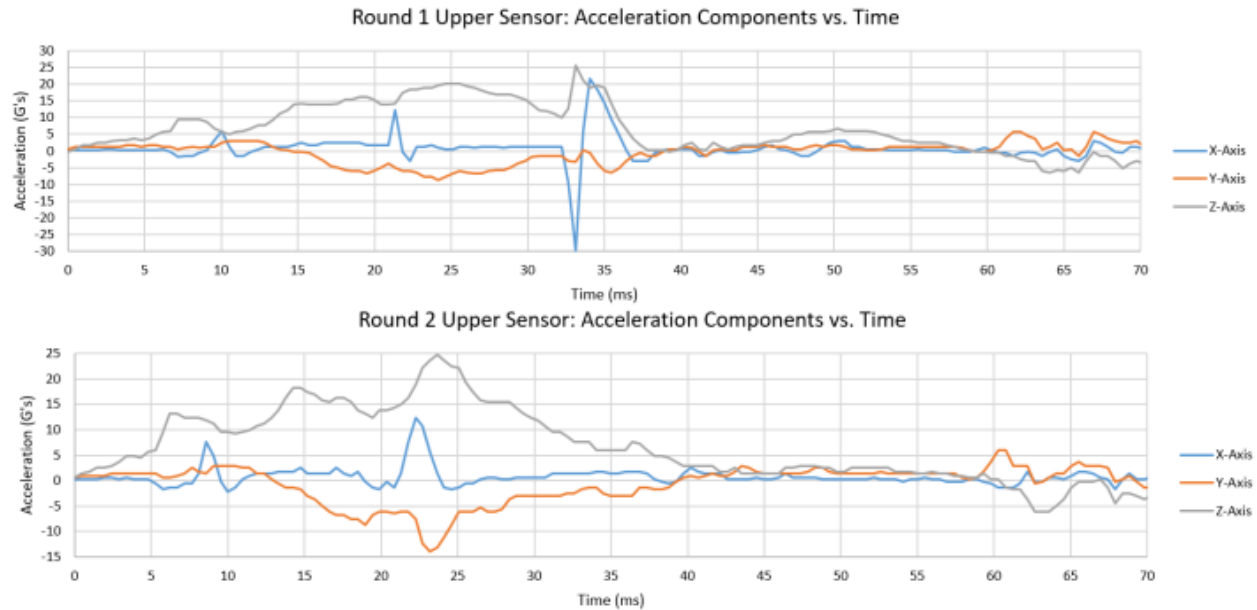
Figure 55: Pilot study upper sensor acceleration measurements for human model with ScarabSpine and Viper Pro pad.

The graphs above show interference of the tape shifting from 34 ms in round 1 to 23 ms in round 2. Snapping at an earlier time decreased the influence of this event on the accelerometers because it required less energy to release the tape from the fixture. Despite the different response between rounds, the data sets were accepted due to the risk of damaging the material properties of the Viper Pro from excessive impacts. Vector magnitudes for each segment were calculated and are displayed in Figure 56.
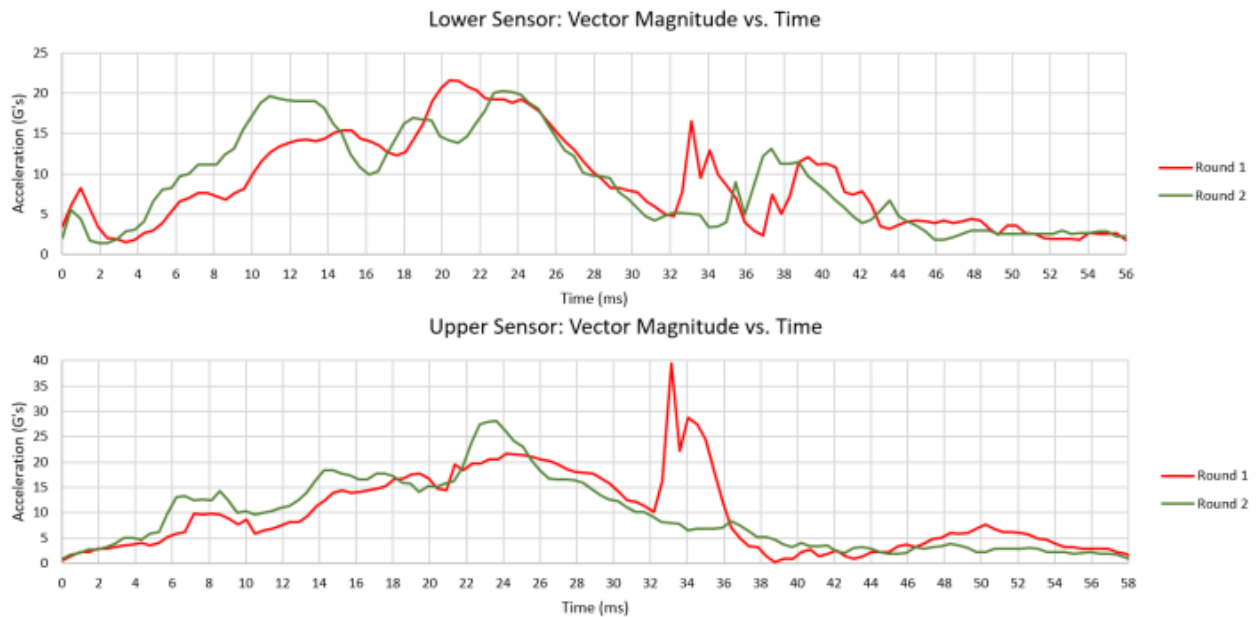
Figure 56: Pilot study vector magnitudes for both sensors during human model with ScarabSpine and Viper Pro pad testing.

The average impact times for the lower segment to reach zero velocity and total rebound were 24 ms and 51 ms, respectively. The average accelerations for these two time intervals were 12.2 G's and 9.7 G's, respectively. The resulting average rebound coefficient was calculated as 0.65. These lower segment results displayed longer impact times and lower acceleration than the previous test configuration. The upper segment experienced similar results.

The upper segment average impact times were 25 ms and 58 ms for the zero velocity and total rebound periods. Average accelerations were calculated to be 12.1 G's and 9.4 G's for each time interval, respectively. Finally, the average rebound coefficient was calculated as 0.86. Impact times and acceleration levels for both segments are provided in Table 9 and in the Appendix.

Table 9: Pilot study human model with ScarabSpine and Viper Pro results.

| | Round | Impact Time (ms) | | Rebound Coefficient | Average G's | | Peak G's |
		V->0	Total		V->0	Total	Excluding Tape
Lower Segment	1	25.1	54.5	0.67	11.8	9.1	21.6
	2	23.7	46.4	0.63	12.5	10.3	20.3
Upper Segment	1	26.1	58.3	0.92	11.3	9.6	21.6
	2	23.7	58.4	0.80	12.8	9.2	28.1

The upper and lower segments experienced nearly identical accelerations and closer impact times than any other test. The ScarabSpine and Viper Pro pad configuration displayed the ability to normalize upper and lower segment impact reactions while minimizing deflection and acceleration. Figure 57 shows the device preventing the hyperextension that was identified in Figure 38.

Figure 57: Pilot study demonstration of ScarabSpine and Viper Pro hyperextension prevention.

Results from the pilot study produced the necessary coefficient restitution values to continue with the next experimental phase. The physical demonstration also increased confidence in the device's capability to withstand the final 20 mph drop test.

4.3 Drop Testing

4.3.1 Human Model Only

      The first full scale drop test was conducted with only the punching bag. Accelerations during the impact event were recorded and video footage captured using the same method from the pilot study. Lower segment acceleration measurements are graphically displayed below.
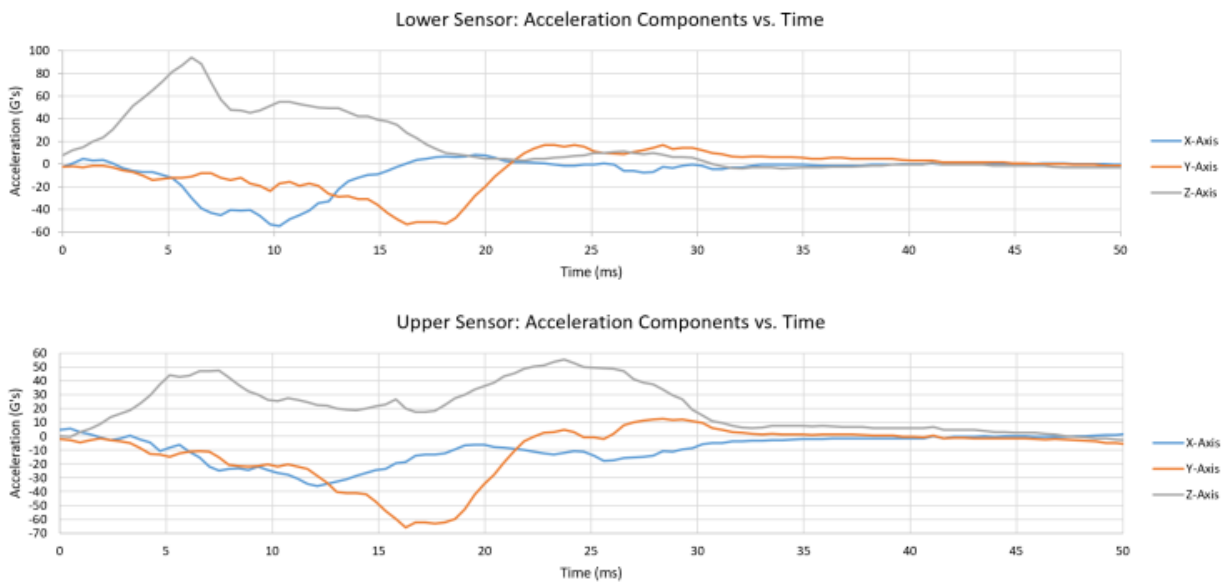
Figure 58: Drop test acceleration measurements for both sensors on human model.

      The sensors were aligned with the z-axis in the direction of impact. Test results revealed significant measurements recorded in the x and y axis due to the under constrained drop test method. The impact time end criteria remained depended on the z-axis, but the vector magnitude was calculated to account for all directions. The resulting total impact times for lower and upper segments were 31 ms and 47 ms, respectively. The vector magnitude calculations are graphically illustrated in Figure 59.
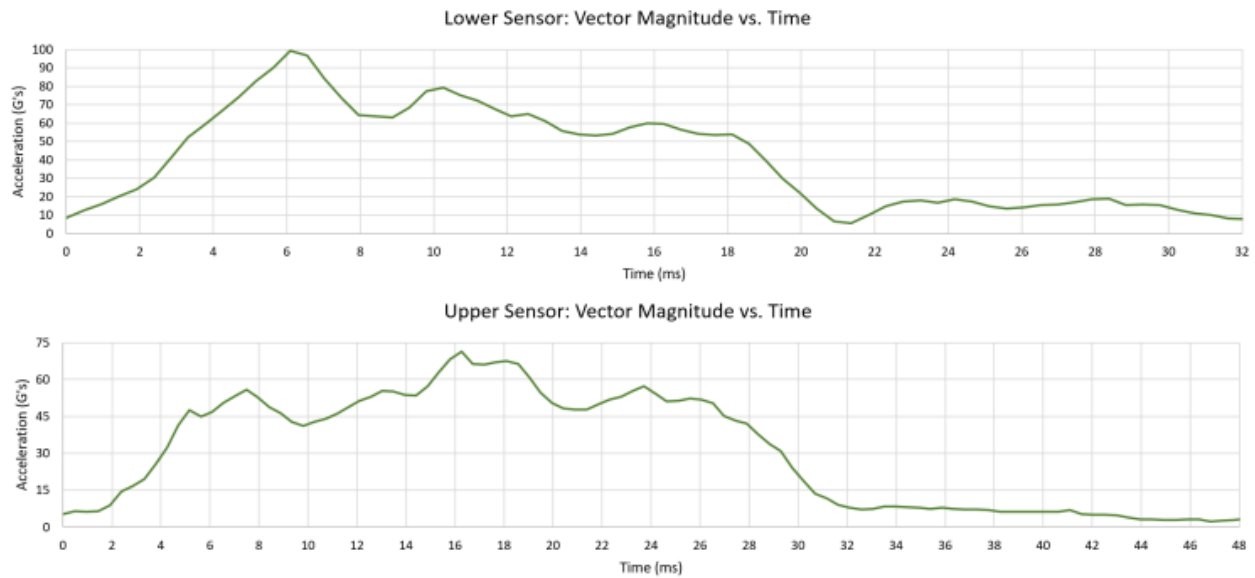
Figure 59: Drop test vector magnitudes for both sensors during human model testing.

The lower segment data were particularly important for this drop because they represented the acceleration an unprotected person would undergo during direct impact. Throughout the research and design phases the pedestrian was theorized to reach 20 mph in 15 ms yielding an average acceleration of 60.8 G's. The actual recorded data showed this expected change in velocity to occur 15.3 ms after the point of impact and measured an average acceleration of 59.7 G's. Direct comparison between the measured and theoretical accelerations resulted in a percent error of 1.8%. The testing and data collection methods were highly supported by this outcome.

The average measured acceleration for the lower segment's total impact was 42.4 G's. A theoretical acceleration was also calculated using the impact time and acting coefficient of restitution from the pilot study. This theoretical acceleration was 42.5 G's revealing a difference of 0.1%.

Upper segment measurements resulted in an average acceleration of 44.9 G's to reach a change in speed of 20 mph. The total impact time resulted in an average measured acceleration of 31.4 G's, due to the lack of support and extended impact time. A theoretical acceleration was calculated to be 31.0 G's. The resulting difference was 1.1%. Despite the upper segment experiencing a desirably low acceleration, its deflection was extremely high. The top of the bag traveled all the way to the ground 7.75 inches below the impacting face, see Figure 60.
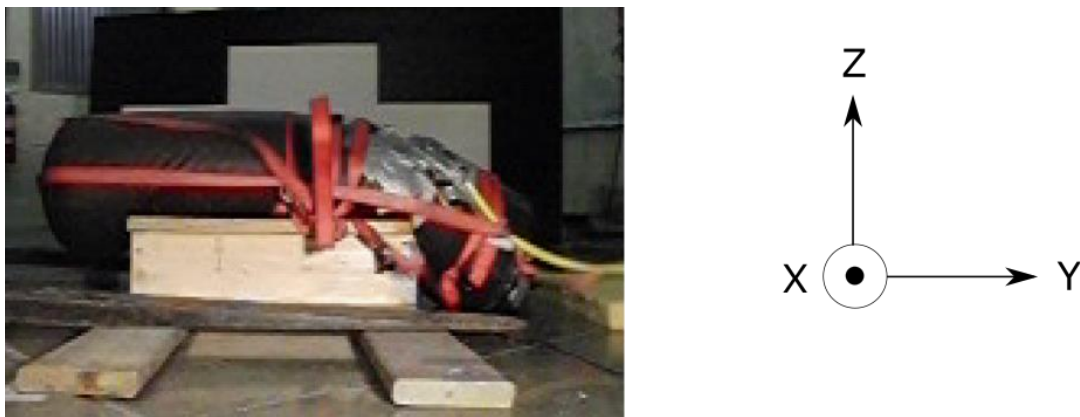
Figure 60: Drop test with bag only impact deflection.

An additional metric for comparing drops was the length of time peak accelerations exceeded 60 G's and 85 G's. It was previously identified that the critical chest acceleration level for the TIC was 60 G's for a time interval no longer than 3 ms [2]. This acceleration level was intended for the area of support provided by a vehicle's seat belt and would significantly reduce the probability of severe injury. It was also identified by the TTI that the absolute maximum peak interval for a pedestrian was 85 G's for 3 ms [3]. The length of time each segment experienced accelerations larger than 85 G's is provided in Table 10. Additionally, the lower segment experienced 60+ G's for 9.3 ms and the upper segment for 3.7 ms.

Table 10: Drop test human model only results.

Segment	Impact Time (ms) V->0	Impact Time (ms) Total	Average G's V->0	Average G's Total	Peak G's	Maximum Peak Interval (ms)	Hyperextension (in)
Lower	15.3	30.7	59.7	42.4	99.3	0.9	N/A
Upper	20.0	47.3	44.9	31.4	71.3	N/A	7.75+

The peak acceleration experienced by the lower segment equated to a force of 1,990 lb. This was comparable to a mean peak force of 2,050 ± 337 lb found during research for lateral impact of the same region at 20 mph [25]. This literature also displayed a total impact time approximately 14 ms longer than measured for the lower segment. The maximum peak interval remained below 3 ms for both segments but the 60+ G's interval for the lower segment lasted longer than 3 ms and the upper hyperextension was extreme.

4.3.2 Human Model with Aluminum Plate

The aluminum was placed on the human model and dropped from the same height. Recorded measurements from all axis for both sensors are graphed in Figure 61. The lower segment y-axis and z-axis data demonstrated a similar wave form to the human model only testing. On the other hand, the x-axis was inverted indicating the bag was slightly rolled across the y-z plane in the opposite direction upon impact. Despite this difference the results were comparable due to the decision to calculate the vector magnitudes.
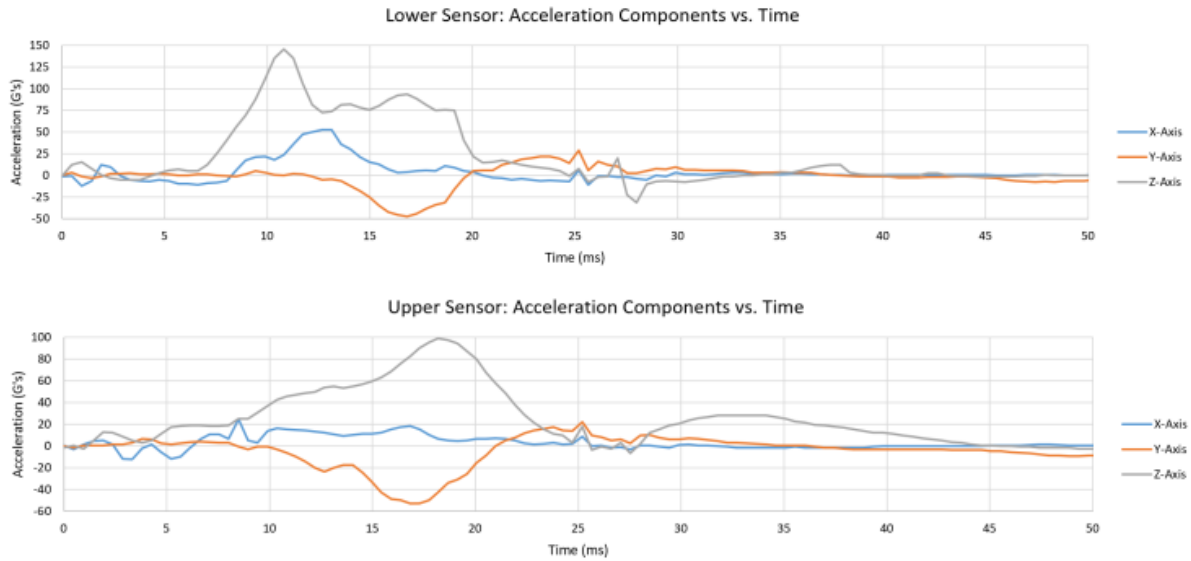
Figure 61: Drop test acceleration measurements for both sensors on human model with aluminum plate.

Total impact time for the lower segment was 33.2 ms, approximately 2.5 ms longer than the previous test. The upper segment's total impact time was 44.6 ms. This shorter impact indicated the presence of an object adding rigidity to the system. The vector magnitudes for both segments were graphed to further analyze the impact scenario, see Figure 62.
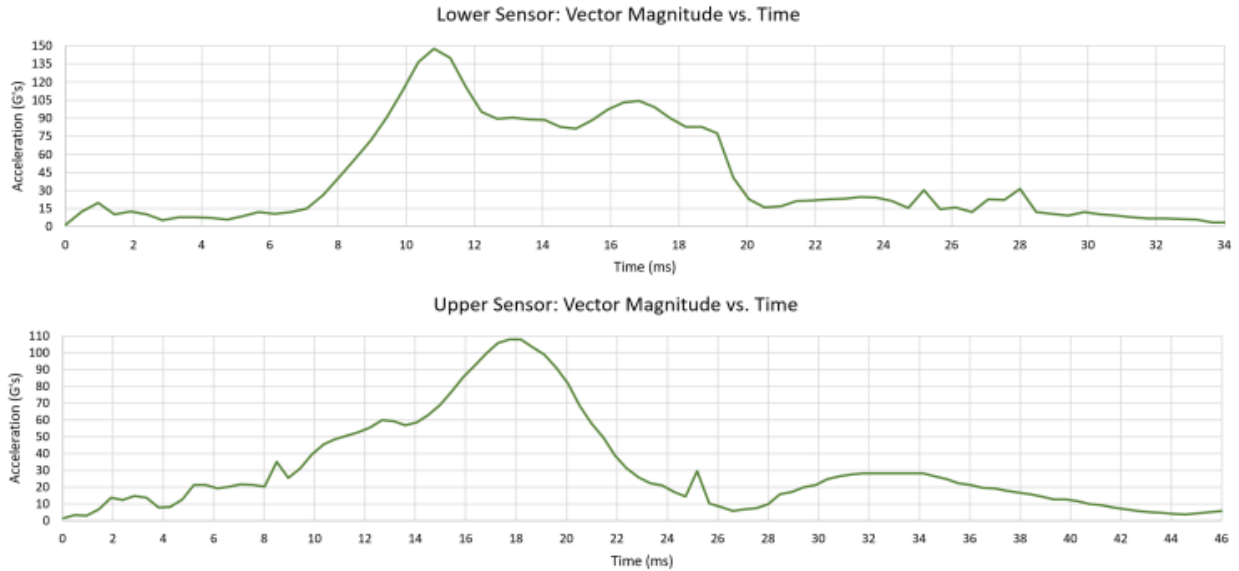
Figure 62: Drop test vector magnitudes for both sensors during human model with aluminum plate testing.

The average acceleration for the lower and upper segments during the initial 20 mph change in speed was 55.6 G's and 46.4 G's, respectively. As compared to the previous test, the lower segment acceleration decreased and the upper segment acceleration increased. The upper sensor's increase was expected because of the added rigid plate.

The lower segment's total impact average acceleration was 42.4 G's with a theoretical percent difference of 13.7%. Upper sensor average acceleration was 32.1 G's with a theoretical difference of 21.5%, see Table 11. The large percent difference was attributed to plastic deformation of the aluminum plate. Upon impact the metal experienced a significant amount of deflection, which extended the impact time. During pilot study testing the aluminum plate did not bend and resulted in a coefficient of restitution that did not accurately represent a deformation scenario. In support of this observation, the coefficient of restitution from the bag

only model was used to calculate a theoretical acceleration for the upper segment's total

impact time period. The resulting percent difference was reduced to 2.5%.

Table 11: Drop test human model with aluminum plate results.

Segment	Impact Time (ms)		Average G's		Peak G's	Maximum Peak Interval (ms)	Hyperextension (in)
	V->0	Total	V->0	Total			
Lower	16.4	33.2	55.6	42.4	148	4.6	N/A
Upper	20.1	44.6	46.4	32.1	108	3.7	5.5

The segment average accelerations for the total impact time remained consistent when

compared to the previous test. The lower segment experienced similar accelerations during

both tests and the aluminum plate test had a higher upper segment acceleration. The largest

discrepancy in acceleration occurred at the peak acceleration. The lower segment experienced

a peak acceleration level 1.5 times larger than the solitary human model test. The maximum

peak time interval for both segments also exceeded the allowable 3 ms limit. The upper

segment deflection also displayed significant difference. The addition of the aluminum plate

reduced the top of the bag to deflecting approximately 5.5 inches. This dynamic deflection

resulted in plastic deformation of the aluminum plate by bending the top end 1.25 inches

below flat, see Figure 63.
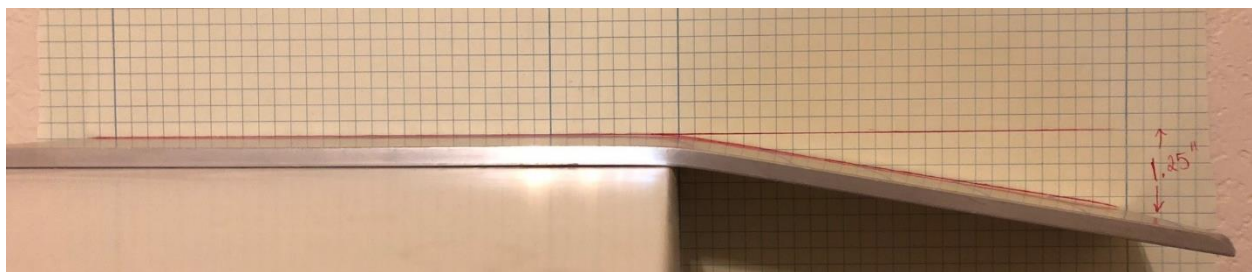
Figure 63: Drop test deformation to aluminum plate.

4.3.3 Human Model with Aluminum Plate and PORON Pad

The third drop test added the impact absorbing pad to an identical aluminum plate from the previous test. This model was expected to demonstrate how a protective pad would directly alter the same impact scenario. The graphs below display the raw data for all axis and both sensors.
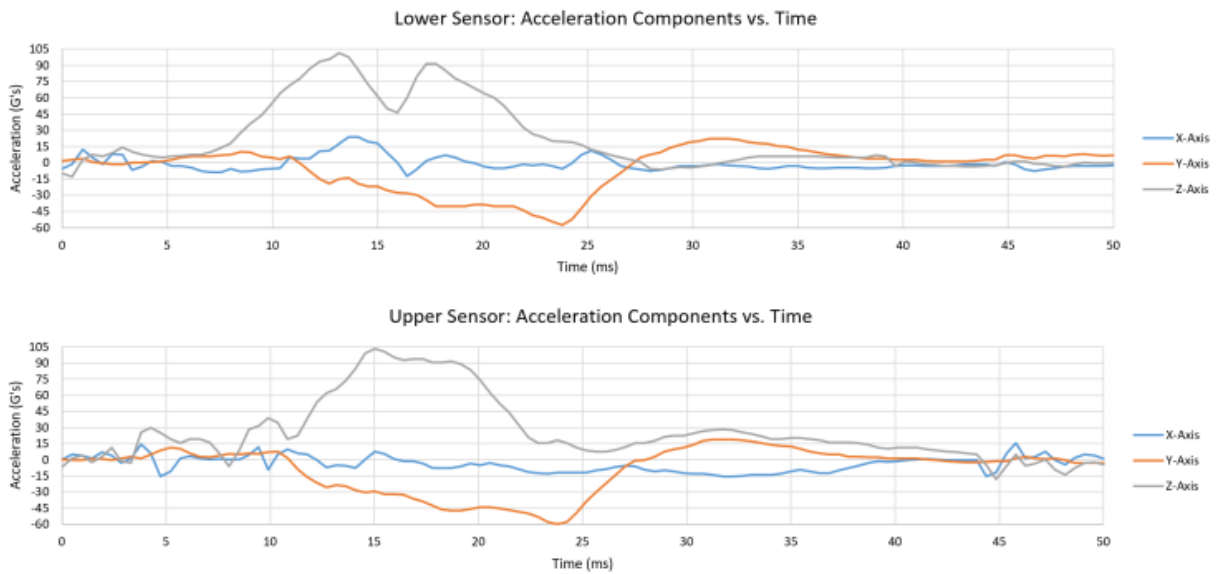
Figure 64: Drop test acceleration measurements for both sensors on human model with aluminum plate and PORON pad.

The lower sensor displays immediate improvement by decreasing the peak acceleration in the z-axis to approximately 104 G's, compared to 148 G's in the previous test. The total impact time for this segment was 39.6 ms, 6.4 ms longer than without the pad. Upper sensor total impact time was 47.2 ms. The longer time could indicate the pad's capability to attenuate forces through increasing the impact time. Lower and upper segment vector magnitude accelerations were graphed for additional analysis, see Figure 65.
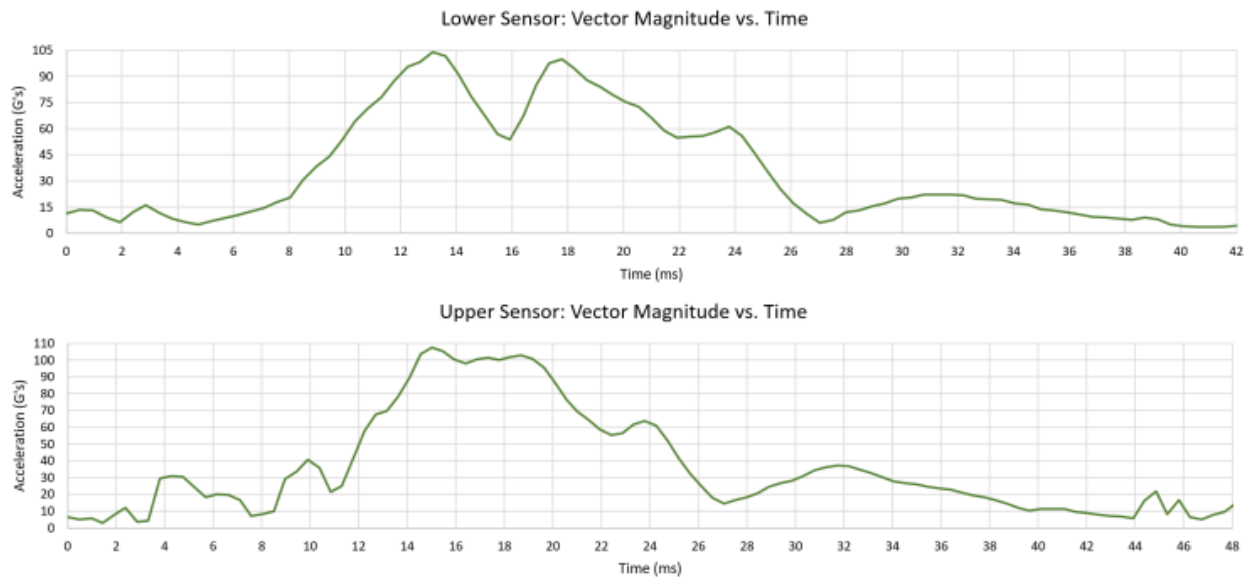
Figure 65: Drop test vector magnitudes for both sensors during human model with aluminum plate and PORON pad testing.

The average accelerations for the lower and upper segments to change speed by 20 mph were 48.5 G's and 47.0 G's, respectively. The lower segment experienced significantly smaller accelerations for this event than in the previous test, a decrease of 7.1 G's, while the upper segment only slightly increased by 0.6 G's. The decrease in lower segment acceleration could also be a direct result of adding the force attenuating material.

Average accelerations from the total impact time further supported the pad's capabilities. The lower segment average acceleration was 38 G's with a difference of 3.4% from the theoretical calculation. Upper segment average acceleration was 36.7 G's with a theoretical difference of 0%. The most significant comparison for this test was the similarity between upper and lower segment accelerations. The segments experienced similar accelerations due to the added rigidity to the system, while the impact absorbing pad enabled the acceleration to remain relatively low. However, the total impact times for both segments were not the same,

which indicated a deflection within the system, see Table 12. The measured impact time to

reach 20 mph was recorded as the same time for each segment due to the data capture

resolution of 0.46 ms.

Table 12: Drop test human model with aluminum plate and PORON pad results.

Segment	Impact Time (ms)		Average G's		Peak G's	Maximum Peak Interval (ms)	Hyperextension (in)
	V->0	Total	V->0	Total			
Lower	19.2	39.6	48.5	38.0	104	2.3	N/A
Upper	19.2	47.2	47.0	36.7	107	6.0	3

The maximum peak time interval showed considerable improvement by adding the

PORON pad. However, the upper segment still exceeded the allowable 3 ms. Video footage of

the drop also showed a dynamic deflection at the top of the plate of approximately 3 inches

below the impacting plane. Further examination of the aluminum plate revealed plastic

deformation of 0.75 inches from its original flat shape, Figure 66. The aluminum plate and

PORON pad configuration demonstrated appreciable reduction of the model's acceleration but

failed to limit the dynamic extension of the upper segment to within the set range.

Figure 66: Drop test deformation to aluminum plate with PORON pad.

4.3.4 Human Model with ScarabSpine and Viper Pro Pad

The final drop scenario tested the capabilities of the ScarabSpine and Viper Pro pad. The model was dropped three consecutive times to monitor material degradation of the absorbing pad and metallic structure. The lower segment acceleration graphs for each round are displayed in Figure 67.
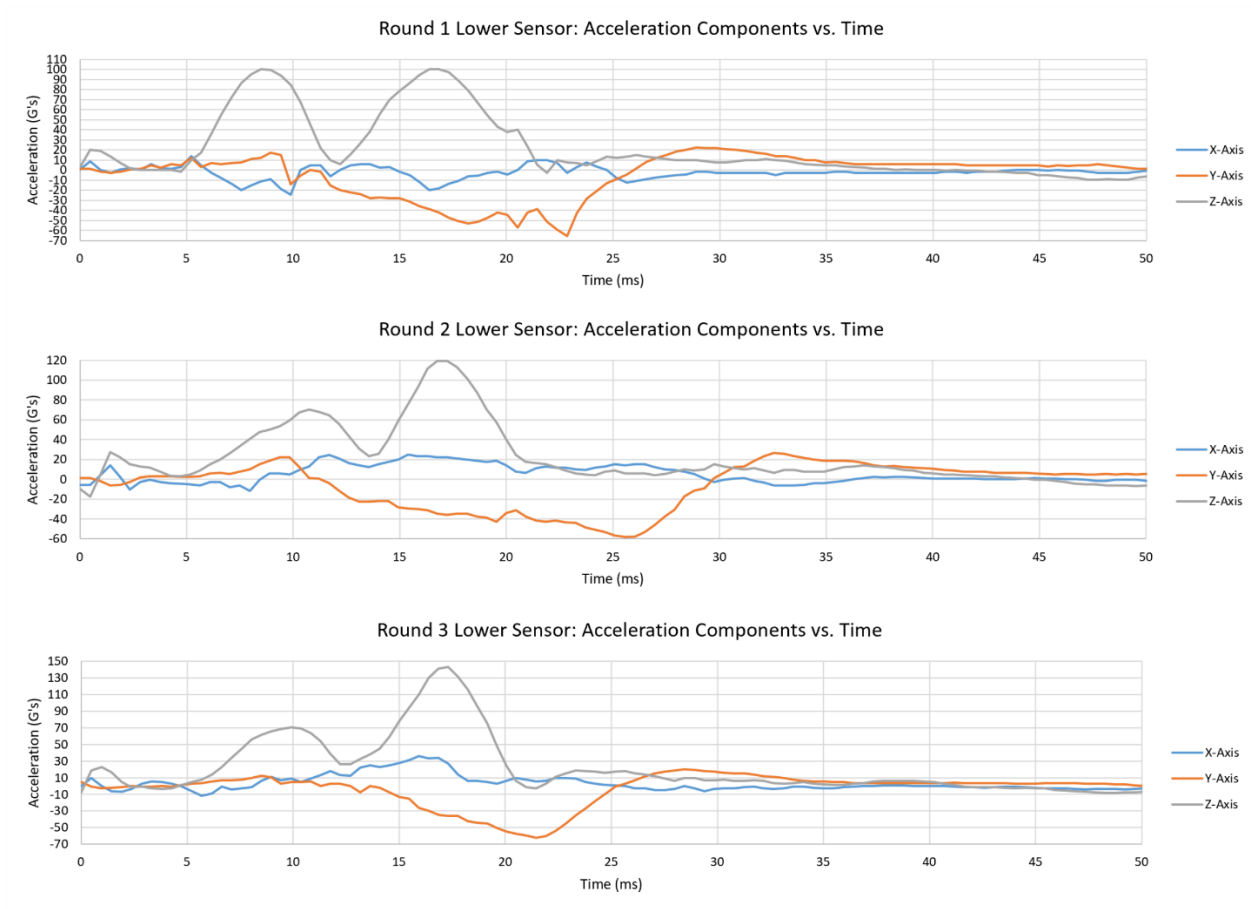
Figure 67: Drop test lower sensor acceleration measurements for human model with ScarabSpine and Viper Pro pad.

The first round showed very similar accelerations and impact times for the lower segment compared to the previous model. Total impact times for the three rounds were

38.2 ms, 44.3 ms, and 41.6 ms, respectively. Round 1 recorded the shortest impact duration while maintaining lower peak acceleration values in the z-axis. The maximum z-axis acceleration was 100 G's while rounds 2 and 3 recorded peaks of 120 G's and 143 G's. This consistent increase of approximately 20 G's could be an indication that the absorbing pad's performance decreased after each impact. The upper sensor measurements were also analyzed to determine the ScarabSpine's performance, see Figure 68.
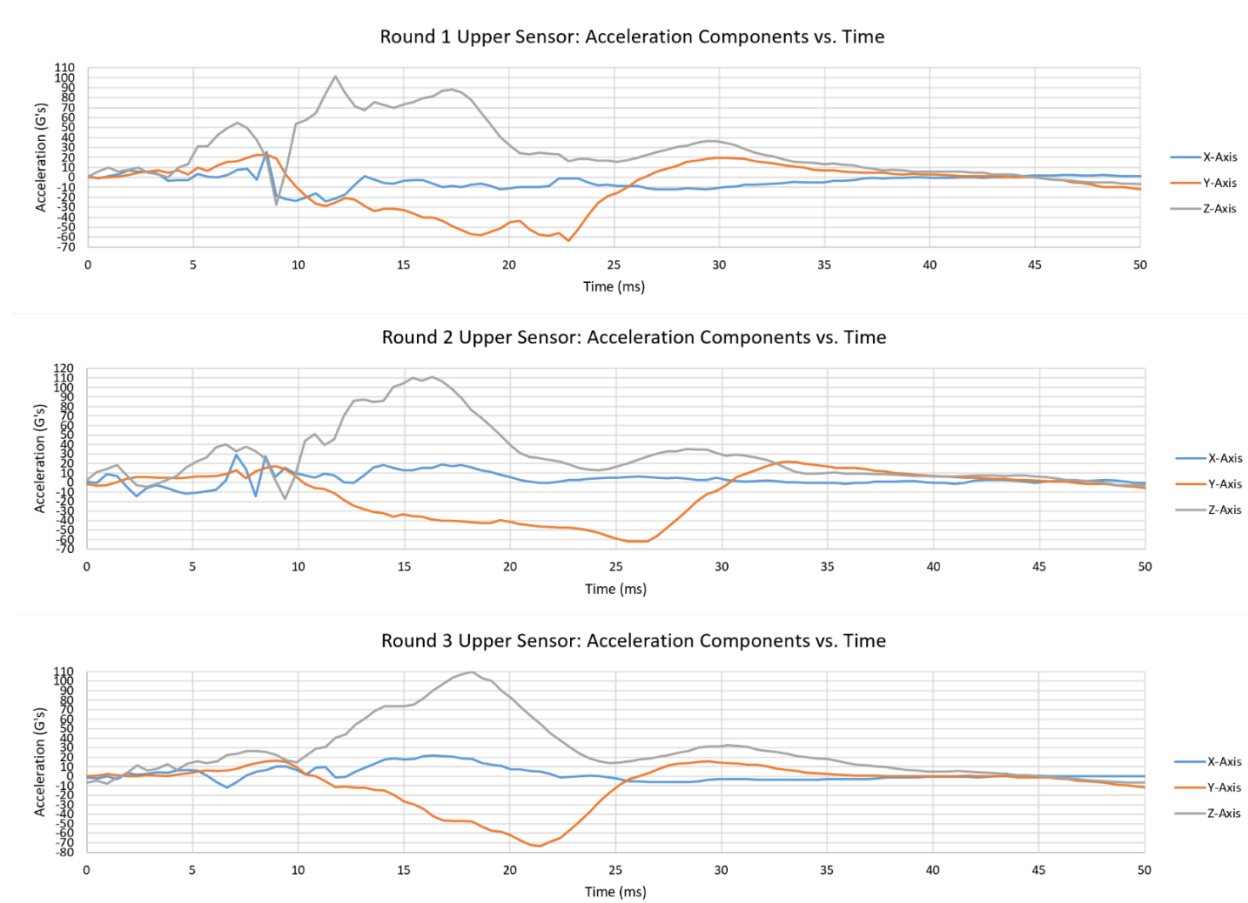
Figure 68: Drop test upper sensor acceleration measurements for human model with ScarabSpine and Viper Pro pad.

The upper segment total impact times for all three rounds were 44.4 ms, 47.2 ms, and 45.0 ms, respectively. Round 1 revealed an impact duration difference of 6.2 ms between upper and lower segments. This was a smaller difference than the three previous configurations and supported the applied rigidity of the ScarabSpine to the system. Rounds 2 and 3 had longer impact time differences indicating additional deflection by the ScarabSpine.

Video footage of the first drop revealed a dynamic deflection of approximately 1.5 inches at the top of the ScarabSpine, see Figure 69. After the test the ScarabSpine was measured to extend approximately 0.55 inches past a flat position. The result was plastic deformation to the ScarabSpine that allowed it to bend an additional 0.35 inches past the original 0.2 inches from static testing.

(a)   (b)
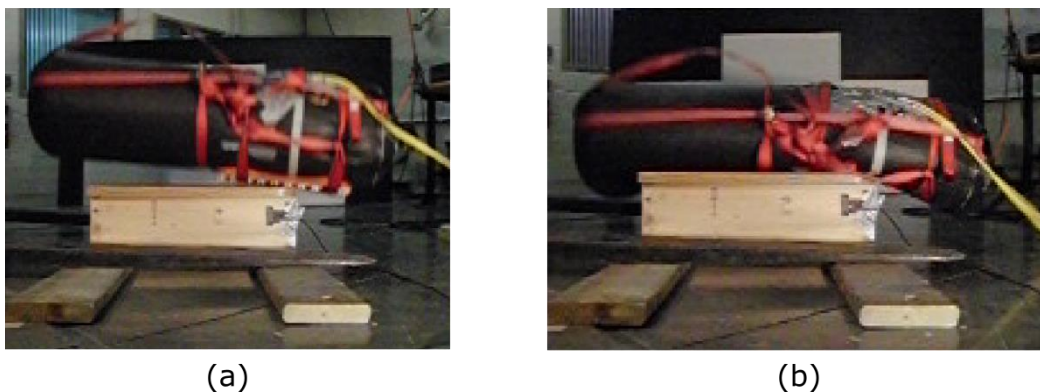
Figure 69: ScarabSpine and Viper Pro drop test footage (a) at moment of impact and (b) at maximum deflection.

Round 2 and 3 displayed larger dynamic deflections than round 1. Their maximum deflections were similar to the aluminum plate and PORON pad model and resulted in static deflection measurements of approximately 1 inch and 1.5 inches, respectively. Visual inspection of the ScarabSpine showed deformation to multiple components, see Figure 70.
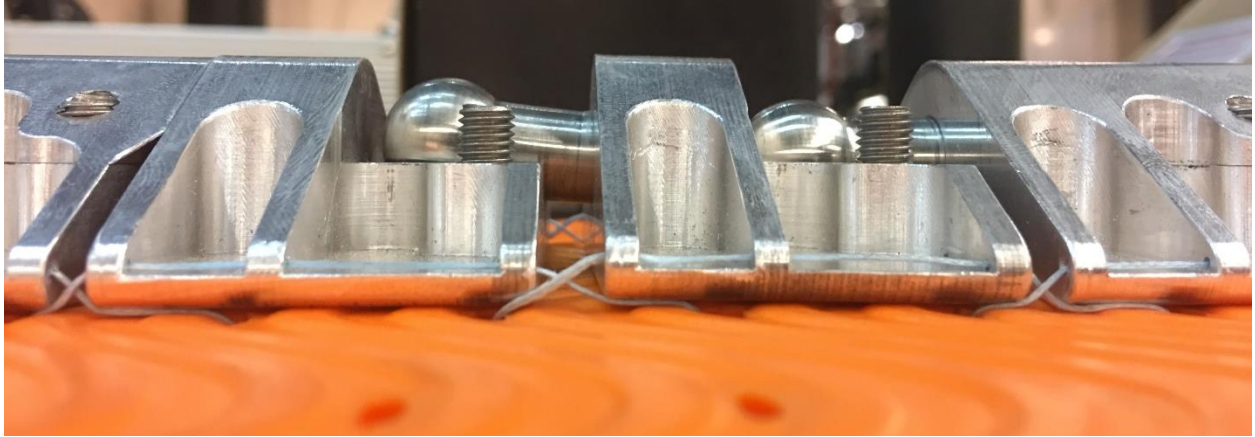
Figure 70: ScarabSpine deformation after Round 2.

The modes of failure included bent stainless steel ball studs, deformed aluminum edges due to compression, and separation between joints through slippage by the ball stud shaft. After round 3 there were a total of two bent ball studs, four deformed edges, and four separated joints with a maximum gap of 0.05 inches. The increased deformation from consecutive tests lead to decreasing average accelerations. The vector magnitudes for all rounds and both segments are provided in Figure 71.
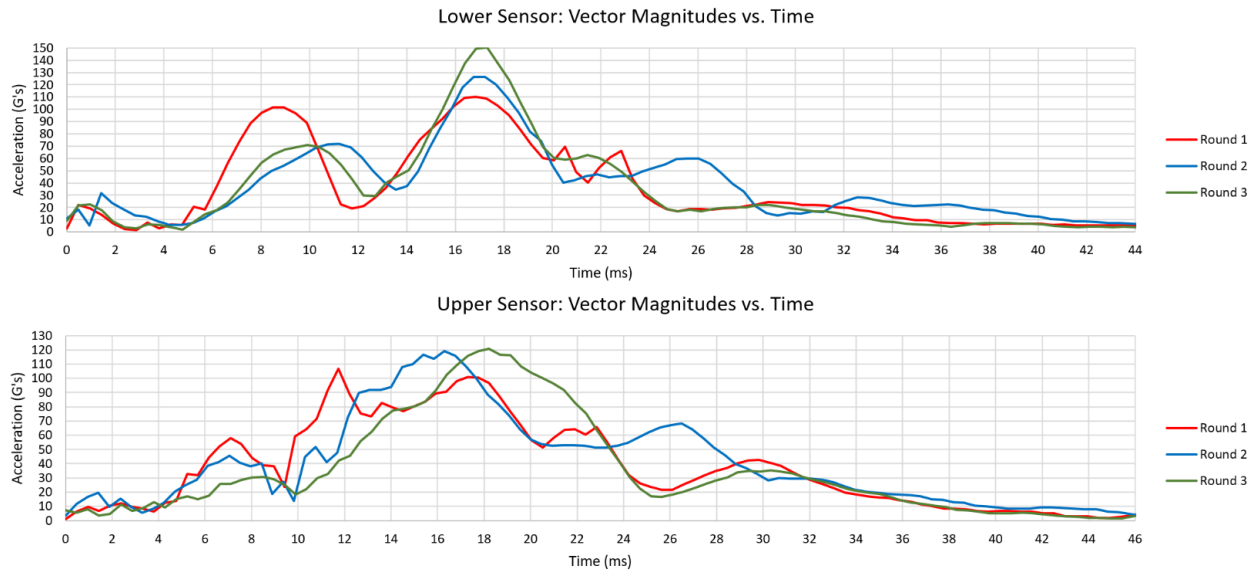
Figure 71: Drop test vector magnitudes for both sensors during human model with ScarabSpine and Viper Pro pad testing.

Initial comparison between drops was conducted by calculating the average acceleration each segment experienced during the initial change speed of 20 mph. In round 1 the lower and upper segments underwent average accelerations of 51.4 G's and 52.0 G's, respectively, over a 17.8 ms duration. The lower segment acceleration was approximately 3 G's higher than the previous model, but the difference between the two segments was much smaller. This indicated the segments were absorbing the impact energy at the same rate, due to the added rigidity, without elevating the accelerations to bare impact scenario levels.

Calculations for round 2 resulted in average accelerations of 48.8 G's and 51.4 G's for lower and upper segments, respectively. The difference between the values increased because of the larger deflection. Round 3 continued this trend with accelerations of 49.9 G's and 47.4 G's for lower and upper segments.

116

Average accelerations for the total impact were also calculated for both segments. The lower segment accelerations for each round were 39.7 G's, 38.2 G's, and 36.5 G's, respectively. Theoretical calculations based off pilot study data and the impact duration revealed a percent difference of 1.0%, 12.5%, and 1.1% for each respective round. Upper segment average accelerations were 38.8 G's, 39.6 G's, and 36.3 G's for each round. The calculated differences were 1.6%, 10.3%, and 3.8%, respectively. Results are tabulated below in Table 13. The increased percent error developed in round 2 was attributed to the angle of impact. During the drop the model tilted forward and impacted the grill model at a larger angle than any other drops.

Table 13: Drop test human model with ScarabSpine and D3O pad results.

Round	Segment	Impact Time (ms)		Average G's		Peak G's	Maximum Peak Interval (ms)	Hyperextension (in)
		V->0	Total	V->0	Total			
1	Lower	17.8	38.2	51.4	39.7	110	2.8	N/A
	Upper	17.8	44.4	52.0	38.8	107	2.8	1.5
2	Lower	18.1	44.3	48.8	38.2	127	2.8	N/A
	Upper	17.7	47.2	51.4	39.6	119	5.5	2.0
3	Lower	17.8	41.6	49.9	36.5	150	3.7	N/A
	Upper	19.6	45.0	47.4	36.3	121	5.5	2.5

The results from round 1 demonstrated acceleration levels similar to the aluminum and PORON pad model while minimizing deflection during impact. The device also showed considerable improvement by keeping the maximum peak time interval below the 3 ms limit for both segments in round 1. Compared to the unprotected human model, the ScarabSpine and Viper Pro configuration normalized the acceleration experienced by both segments, significantly reduced acceleration levels for both time periods, and minimized the dynamic hyperextension. The added device reduced the acceleration difference between segments to

approximately 0.6 G's and 0.9 G's for each time interval. The lower segment acceleration levels

were decreased by approximately 8.3 G's for the initial impact and by 2.7 G's for the total

impact time. Finally, the deflection was decreased to 1.5 inches from the original 7.75 inches.

The combination of decreased segment acceleration and minimal dynamic deflection supports

the application of the ScarabSpine and force attenuating pad as a protective measure during

high impact scenarios.

5 Future Work

The everyday high energy scenario of a vehicular collision has well documented support

for the need of a new protective measure for unprotected persons. This first work produced an

innovative basic design that showed potential through a limited testing criteria. Additional

testing of the ScarabSpine and the Viper Pro pad with a certified 50th percentile male model

would more accurately represent a real-world impact scenario. Design optimization could also

result in a lighter weight more user friendly construction. It was also mentioned during

development that a full coverage device would be ideal, therefore future research would

include extending the ScarabSpine to protect the cervical spine and coccyx regions. Finally, the

application of the ScarabSpine's specialized joints should be explored for the protection of

other body regions.

6 Conclusion

This master's thesis set out to design, analyze, develop, and test a high-energy trauma prevention safety device for unprotected persons. A review of literary works supported the need for such a device during LTV-to-pedestrian collisions. Further research defined a critical impact scenario between pedestrians and light pickup trucks approaching from the rear at 20 mph. This collision speed was found to generate accelerations to a person's torso that exceeded the allowable range defined by the NHTSA and cause spinal hyperextension. Existing devices and patents were examined to insure a unique design that would satisfy safety specifications while remaining functional and ergonomic.

The resulting design was a metallic biomimetic structure combined with an advanced force attenuating material. The impact absorbing pad was selected for its documented superior properties to minimize transmitted forces. The metallic component prevented hyperextension of the spine and gave the design novelty. The ScarabSpine was the focus during the analysis stage.

Analytical methods ranged from simplified beam calculations to finite element software. Hand calculations were an initial tool that supported the ScarabSpine's geometry and material properties. FEA was a comprehensive method that accounted for additional complexities in the ScarabSpine design. Both tools provided results that supported the device's ability to withstand the applied forces during the impact scenario. Analysis of the design provided sufficient evidence of its theoretical strength and lead to the development of a physical model.

Fabrication of a prototype was critical to support a real-world application. The metallic structure was fully manufactured to within the specifications set during the design phase. A testing procedure was then created and executed through physical experimental analysis.

Experimental impact testing was conducted with a mock human model in two stages. Stage 1 consisted of a pilot study to confirm the selected data collection method and provided a deeper understanding of the impact biomechanics. Full scale drop testing was completed in stage 2. The results from the ScarabSpine and Viper Pro pad configuration displayed superior impact protection capabilities by minimizing segment acceleration, maximizing impact time, and reducing upper segment hyperextension. Developed average accelerations including and excluding the rebound were decreased by 8.3 G's (14%) and 2.7 G's (6%), respectively. The device normalized the impact times across the model and increased the pre-rebound and total durations by approximately 2.4 ms (16%) and 7.5 ms (24%), respectively. Experienced peak accelerations for both segments remained within the allowable 3 ms time interval at 2.8 ms. Finally, the upper segment dynamic hyperextension was reduced by 6.25 inches (81%) from an initial unprotected deflection of 7.75 inches to a minimal 1.5 inches. These experimental results supported the developed device in preventing high-energy trauma by minimizing hyperextension of the human spine and reducing experienced average accelerations during impact. Therefore, the developed theory was confirmed supporting the application of an impact absorbing material in combination with a biomimetic metallic structure to protect pedestrians subjected to a forward projecting collision with a large vehicle approaching from the rear at 20 mph.

7 Appendix A

7.1 Center of Mass for the 50th Percentile Male

Anthropometric data used for the pedestrian is tabulated below. The body was assumed to be symmetrical allowing the arms, hands and legs segments to be summed.

Table A. 11: Body segment weights for 50th percentile male [5].

Body Segment Number	Body Segment	Weight (lb)
0	Lower Torso (Pelvis)	22.05
1	Middle Torso (Lumbar)	24.14
2	Upper Torso (Chest)	40.97
3	Upper Arms	9.84
4	Lower Arms	6.12
5	Hands	2.30
6	Neck	3.97
7	Head	10.91
8	Upper Legs	37.26
9	Lower Legs	15.22
10	Feet	4.54
	Total	**177.32**

The center of mass for each segment was calculated using the lower torso segment (pelvis) as the origin. Table A.2 provides the mass center of each segment with respect to the pelvis in the vertical direction (z-axis).

Table A. 12: Body segment mass center with respect to the pelvis [5].

Body Segment	Location (in)
Lower Torso (Pelvis)	0.000
Middle Torso (Lumbar)	8.100
Upper Torso (Chest)	16.098
Upper Arms	13.482
Lower Arms	0.450
Hands	-8.850
Neck	22.398
Head	28.746
Upper Legs	-10.518
Lower Legs	-27.312
Feet	-37.704

The center of mass for the entire body was then calculated at approximately 2.2 inches above the pelvis, using Equation B.1. To find the mass center relative to the ground, it was assumed that the eyes were located at the mass center of the pedestrian's head. The standing eye height of the 50th percentile male was 64.7 inches [5]. The center of mass was then calculated by subtracting the standing eye height by the head center of mass and adding 2.2 inches. This resulted in a total body center of gravity at approximately 38 inches above the ground.

Table A. 13: Hybrid III 50th percentile male segment weights [6].

Body Segment	Weight (lb)
Head	10.0
Neck	3.4
Upper Torso	37.9
Lower Torso	50.8
Upper Arms	8.8
Lower Arms and Hands	10.0
Upper Legs	26.4
Lower Legs and Feet	25.0
Total Weight	172.3

Table A. 14: Hybrid III 50th percentile male lengths [6].

Dimension Description	Specification (in)
Stature	69.0
Head Circumference	23.5
Head Breadth	6.1
Head Depth	8.0
Erect Sitting Height	34.8
Shoulder to Elbow Length	13.3
Back of Elbow to Wrist Pivot Length	11.7
Buttock to Knee Length	23.3
Knee Pivot Height	19.5

Table A. 15: Aluminum and stainless steel material properties [7] [8] [9] [10] [11] [47].

	6061-T6	7075-T651	304 SS
Density (lb/in^3)	0.0975	0.102	0.29
Hardness (Rockwell)	B-60	B-87	B-76
Yield Strength (psi)	35,000	56,000	30,000
Ultimate Tensile Strength (psi)	45,000	83,000	97,000
Tensile Yield Strength (psi)	40,000	73,000	59,500
Modulus of Elasticity (ksi)	10,000	10,400	29,000
Poisson's Ratio	0.33	0.33	0.29
Machinability (%)	50	70	-
Shear Modulus (ksi)	3,770	3,900	12,500
Shear Strength (psi)	30,000	48,000	72,750

Table A. 6: Analysis of pilot study human model only.

	HS Video Range for V->0 (ms)	Impact Time (ms)		Integrated ΔV (in/s)		Rebound Coefficient	Avg. Acceleration (G's)		Peak Acceleration (G's)	
		To V=0	Total	To V=0	Total		To V=0	Total	Pre-Snap	Total Range
Lower Sensor	Round 1	19.0 to 21.4	19.91	31.32	112	160	0.43	14.6	13.1	28.0	28.0
	Round 2	16.7 to 19.0	18.00	30.34	115	164	0.43	16.4	13.8	28.4	28.4
Upper Sensor	Round 1	26.2 to 28.6	27.01	59.88	113	182	0.61	10.8	7.9	19.6	33.2
	Round 2	26.2 to 28.6	27.47	60.88	114	182	0.60	10.6	7.7	20.5	26.7

Table A. 7: Analysis of pilot study human model with wood plank.

	HS Video Range for V->0 (ms)	Impact Time (ms)		Integrated ΔV (in/s)		Rebound Coefficient	Avg. Acceleration (G's)		Peak Acceleration (G's)	
		To V=0	Total	To V=0	Total		To V=0	Total	Pre-Snap	Total Range
Lower Sensor	Round 1	21.4 to 23.8	23.70	33.14	114	170	0.49	12.5	13.1	32.2	32.2
	Round 2	23.8 to 26.2	25.61	35.48	117	171	0.47	11.9	12.4	31.4	31.4
Upper Sensor	Round 1	28.6 to 31.0	29.32	63.12	115	199	0.73	10.1	8.1	19.0	40.3
	Round 2	26.2 to 28.6	28.42	68.78	115	244	1.13	10.5	9.2	22.9	38.1

Table A. 8: Analysis of pilot study human model with aluminum plate.

	HS Video Range for V->0 (ms)	Impact Time (ms)		Integrated ΔV (in/s)		Rebound Coefficient	Avg. Acceleration (G's)		Peak Acceleration (G's)	
		To V=0	Total	To V=0	Total		To V=0	Total	Pre-Snap	Total Range
Lower Sensor	Round 1	19.0 to 21.4	18.93	36.88	113	203	0.79	15.6	14.1	34.8	34.8
	Round 2	19.0 to 21.4	19.88	38.28	115	207	0.80	15.3	14.0	41.2	41.2
Upper Sensor	Round 1	21.4 to 23.8	21.74	54.07	114	229	1.01	13.6	10.9	25.3	36.0
	Round 2	21.4 to 23.8	22.21	56.40	116	231	0.99	13.6	10.6	26.1	37.3

Table A. 9: Analysis of pilot study human model with aluminum plate and PORON XRD pad.

		HS Video Range for V->0 (ms)	Impact Time (ms)		Integrated ΔV (in/s)		Rebound Coefficient	Avg. Acceleration (G's)		Peak Acceleration (G's)	
			To V=0	Total	To V=0	Total		To V=0	Total	Pre-Snap	Total Range
Lower Sensor	Round 1	21.4 to 26.2	24.16	46.45	116	203	0.75	12.5	11.3	28.5	28.5
	Round 2	21.4 to 26.2	24.20	44.12	117	194	0.67	12.6	11.3	30.5	30.5
Upper Sensor	Round 1	26.2 to 28.6	24.11	54.07	115	219	0.89	12.4	10.4	23.4	35.4
	Round 2	26.2 to 28.6	24.16	54.16	114	219	0.92	12.3	10.5	25.8	32.6

Table A. 10: Analysis of pilot study human model with ScarabSpine and Viper Pro pad.

		HS Video Range for V->0 (ms)	Impact Time (ms)		Integrated ΔV (in/s)		Rebound Coefficient	Avg. Acceleration (G's)		Peak Acceleration (G's)	
			To V=0	Total	To V=0	Total		To V=0	Total	Pre-Snap	Total Range
Lower Sensor	Round 1	23.8 to 26.2	25.11	54.51	115	191	0.67	11.8	9.1	21.6	21.6
	Round 2	23.8 to 26.2	23.65	46.40	114	185	0.63	12.5	10.3	N/A	20.3
Upper Sensor	Round 1	26.2 to 28.6	26.05	58.33	113	218	0.92	11.3	9.6	21.6	39.5
	Round 2	23.8 to 26.2	23.65	58.36	116	209	0.80	12.8	9.2	N/A	28.1

8 Appendix B

8.1 Full Body Center of Gravity Relative to the Pelvis

The 50th percentile male's center of gravity was first calculated with respect to the pelvis

center. Tables A.1 and A.2 provided each segment location relative to the pelvis and individual

segment weights. These values were applied to Equation B.1 to calculate the center of gravity.

$$Z_{cg} = \frac{\sum_{i=0} Z_i w_i}{w}$$

Equation B. 1

Where:
Z_{cg} = Full body center of gravity relative to the pelvis center (in)
i = The individual body segment number
Z_i = The body segment weight center (in)
w_i = The body segment weight (lb)
w = Total weight of the body (lb)

The sum of each segment multiplied by its weight was divided by the total body weight

to find the center of gravity with respect to the center of the pelvis. The full body center of

gravity was calculated to be 2.2 inches above the center of the pelvis.

8.2 Total Distributed Impact Force

This general calculation of force neglected the coefficient of restitution for the human

body and assumed the pedestrian underwent a constant acceleration. It also assumed that the

person's body was a single mass that traveled from 0 to 20 mph in 15 milliseconds. First, the

pedestrian's acceleration was calculated with Equation B.2.

$$a = \frac{V_f - V_i}{t}$$ Equation B. 2

Where:
a = The calculated average acceleration (ft/s^2)
V_f = Final velocity (ft/s)
V_i = Initial velocity (ft/s)
t = Impact time (s)

The result was an acceleration of 1,955 (ft/s^2). The force was then calculated using

Newton's second law of motion Equation B.3.

$$F = ma$$ Equation B. 3

Where:
F = Impact force (lb)
m = Total mass of the pedestrian (slugs)
a = Average acceleration of the pedestrian (ft/s^2)

A total mass of 5.51 slugs was calculated using the total weight of a 50th percentile male

in Table A.1. This mass multiplied by the acceleration from Equation B.2 equaled a force of

10,772 lb.

8.3 Final Velocity of Pedestrian Post Rebound

Calculating the velocities of colliding objects began with the conservation of energy and

momentum. Neglecting the mass of the vehicle, equating the vehicle's initial and final

velocities, and limiting the collision to one dimension drastically simplified the problem. The

equation became dependent on only the relative velocities [55].

$$C_R = \frac{v_p - v_t}{u_t - u_p}$$ Equation B. 4

Where:
C_R = Coefficient of restitution
v_p = Final velocity of the pedestrian (mph)
v_t = Final velocity of the truck (mph)
u_p = Initial velocity of the pedestrian (mph)

u_t = Initial velocity of the truck (mph)

Assuming a restitution coefficient of 0.20 and inputting 20, 20, and 0 for initial truck velocity, final truck velocity and initial pedestrian velocity, respectively, resulted in a final pedestrian velocity of 24 mph.

8.4 Coefficient of Restitution Calculation

Calculating the coefficient of restitution of an object bouncing off a fixed surface was given in Equation B.5 [55].

$$C_R = \frac{v}{u}$$

Equation B. 5

Where:
C_R = Coefficient of restitution
v = Final velocity of the object
u = Initial velocity of the object

A final velocity of 3.8 mph divided by the initial 20 mph equaled a restitution coefficient of 0.19.

8.5 Drop Test Height

The kinematic equation below was used to calculate the drop height required to reach a velocity of 20 mph, neglecting air drag. The resulting height was 160 inches above the target.

$$v_f^2 = v_i^2 + 2gd \rightarrow d = \frac{v_f^2 - v_i^2}{2g}$$

Equation B. 6

Where:
v_f = Impact velocity of 20 mph (352 in/s)
v_i = Initial drop velocity of 0 mph
g = Gravity of 386.2 in/s^2

8.6 Maximum Deflection and Impact Force on an 8 Inch Cantilever Beam

(a)   (b)
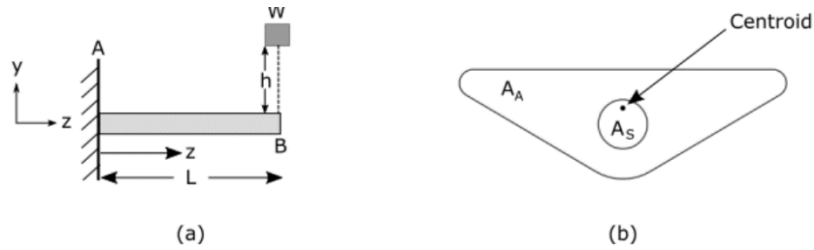
Initial equations were potential energy of a falling mass and the strain energy stored in a beam [52].

$$Potential\ Energy = W(h + \delta_{max})$$
Equation B. 7

$$U = \int \frac{EI_T}{2} (\frac{d^2v}{dz^2})^2 dz$$
Equation B. 8

Where:
W = Weight force of the falling object (lb)
h = Initial height of the falling object (in)
δ_{max} = Maximum deflection occurring at B (in)
U = Strain Energy (in-lb)
EI_T = Total flexural rigidity of the beam (lb-in^2)
v = Deflection in the y direction (in)
z = Position along the beam in the z direction (in)

Through the principle of conservation of energy, Equation B.7 was equal to Equation B.8 yielding the equation below [52].

$$\int \frac{EI_T}{2} (\frac{d^2v}{dz^2})^2 dz = W(h + \delta_{max})$$
Equation B. 9

The left side of Equation B.9 was simplified using the equations for the deflection and slope of a cantilever beam supporting a concentrated load (P) at the end [52]. The following two equations found the deflection along the beam and the deflection at the end of the beam. The only new variable was L, which was the total length of the beam in inches.

$$v = -\frac{Pz^2}{6EI_T}(3L - z)$$ Equation B. 10

$$\delta_{max} = \frac{PL^3}{3EI_T}$$ Equation B. 11

Equation B.11 was manipulated to isolate P and then placed into Equation B.10 to form the following equation.

$$v = -\frac{\delta_{max}z^2}{2L^3}(3L - z)$$ Equation B. 12

Taking two derivatives of Equation B.12 resulted in Equation B.13, which was then substituted back into Equation B.8.

$$\frac{d^2v}{dz^2} = -\frac{3\delta_{max}}{L^2} + \frac{3\delta_{max}z}{L^3}$$ Equation B. 13

The following equation expressed the strain energy of the beam with respect to its maximum deflection.

$$U = \frac{EI_T}{2}\int_0^L \left(-\frac{3\delta_{max}}{L^2} + \frac{3\delta_{max}z}{L^3}\right)^2 dx = \frac{3EI_T\delta_{max}^2}{2L^3}$$ Equation B. 14

Finally, this simplified expression for the strain energy of the beam was substituted into the left side of Equation B.9. The resulting quadratic equation below was solved to find the positive root for δ_{max}.

$$\delta_{max} = \frac{\sqrt{6hEI_TL^3W + L^6W^2} + L^3W}{3EI_T}$$ Equation B. 15

The final unknowns, before calculating the maximum deflection, were the total flexural

rigidity of the beam and the falling object's weight. The following equation expressed the

flexural rigidity of a composite beam with a constant cross-sectional area [52].

$$EI_T = E_A I_A + E_S I_S$$
Equation B. 16

Where:
E_A = Modulus of Elasticity for 7075-T6 aluminum alloy (psi)
I_A = Moment of Inertia for cross-section of aluminum about the assembly's centroid (in^4)
E_S = Modulus of Elasticity for stainless steel (psi)
I_S = Moment of Inertia for cross-section of stainless steel about the assembly's centroid (in^4)

The weight was calculated by equating the resulting bending moment at the cantilever

beam's fixed face during a uniform load and a point load at B. The maximum bending for a

uniform load and point load are shown below, respectively [52].

$$M_{max} = -\frac{L^2 q}{2}$$
Equation B. 17

$$M_{max} = -PL$$
Equation B. 18

Where:
q = Intensity of distributed load (lb/in)

Isolating P, which was equivalent to the object's weight, resulted in the equation below.

$$W = P = \frac{Lq}{2}$$
Equation B. 19

The following values were used to calculate the weight of the falling object, the beam's

flexural rigidity, and the maximum deflection at point B.

1. q = (41 lb/8 in) = 5.125 lb/in
2. L = 8 in
3. E_A = 1.04x10^7 psi
4. I_A = 0.1108 in^4
5. E_S = 2.901x10^7 psi

6. I_S = 0.0048 in^4
7. h = 160 in

The resulting values were a weight of 20.5 lb, total flexural rigidity of 1.292×10^6 lb-in^2, and

maximum deflection of 0.934 inches. In addition, the maximum impact force with respect to

δ_{max} was calculated by solving for P in Equation B.11 and found to be 7,070 lb.

8.7 Maximum Shear Stress in a Circular Cross Section

Calculation of the maximum shear stress experienced in a solid circular shaft was

completed using a simplified formula from the *Mechanics of Materials (7th Edition)* textbook

[52]. Equation B.20 expresses the maximum shear stress as a result of the maximum impact

force and cross-sectional radius.

$$\tau_{max} = \frac{4V}{3\pi r^2} \hspace{4cm} \text{Equation B. 20}$$

Where:

τ_{max} = Maximum shear stress (psi)

V = Maximum impact force of 7,070 lb

r = Radius of 0.225 in

The resulting shear stress in a 0.45 inch shaft is 59,271 psi. This stress exceeds the

ultimate shear strength of 7075 aluminum, but not the 72,750 psi ultimate shear strength of

304 stainless steel. This result supports the use of 304 stainless as the ball stud material.

8.8 Rebound Coefficient

Manipulation of the equation for the coefficient of restitution resulted in a scalar form

referred to as the rebound coefficient. As a result of the speed being directionless, the

coefficient could be greater than 1.

$$R_C = \frac{\Delta S - S_i}{S_i} \qquad\qquad \text{Equation B. 21}$$

Where:
R_C = Rebound Coefficient
ΔS = Change in Speed (mph)
S_i = Initial Speed (mph)

8.9 Cantilever Beam Deflections for Different Cross-Sections

The maximum deflection of a cantilever beam of identical length, applied force, and

material becomes solely dependent on the cross-section's moment of inertia, shown in

Equation B.11. The moment of inertia for a rectangle and isosceles triangle of equivalent height

(h) and width (b) were provided by the *Mechanics of Materials (7th Edition)* textbook [52].
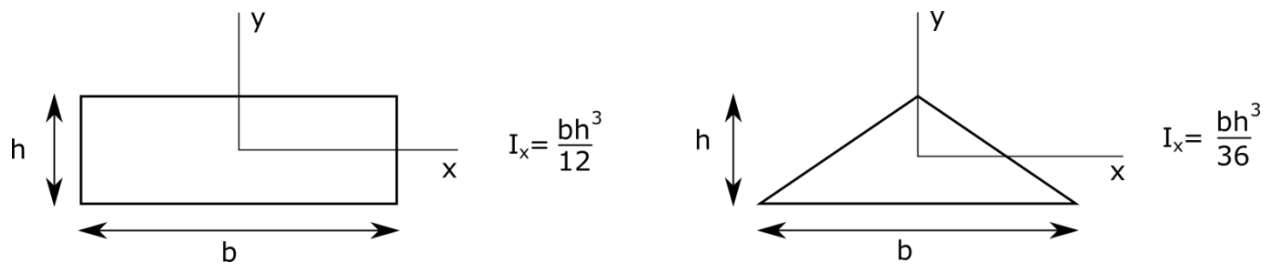
The equations from the figure above shows that the moment of inertia for the rectangle

is three times that of the triangle. Applying this relationship to Equation B.11, the triangle will

result in a maximum deflection three times larger than that of the rectangle. With the selection

of rigid materials minimizing the deflection range, the cross-sectional area impacted the weight

of the ScarabSpine column more than the deflection.

9 Appendix C

9.1 Arduino Mega Code

```
/*
 * Impact Testing Data Collection
 * Sensors: Two high-G accelerometers (+-200gs), one low-G breakout board to record human model orientation
 *       High-G1 and breakout board on lower section, High-G2 on upper section
 * Flow: 1. Initialize breakout board sensors (delay 100ms)
 *       2. Read breakout board and serial print acceleration(x,y,z), gyro(x,y,z), orientation(roll,pitch,heading), and time(ms)
 *       3. Take 6 readings from high-G1 and high-G2. Serial print averages x1, y1, z1, x2, y2, z2, and elapsed time(ms). Delay 1000ms
 *       4. Wait for button to indicate release. Then flash LED, print orientation for 100ms into release, and wait for impact trigger level.
 *       5. Turn LED on, take 200 sample array on high-g sensors, print to serial, and turn LED off.
 */

#include <Wire.h>
#include <Adafruit_Sensor.h>
#include <Adafruit_LSM303_U.h>
#include <Adafruit_L3GD20_U.h>
#include <Adafruit_10DOF.h>

Adafruit_L3GD20_Unified gyro   = Adafruit_L3GD20_Unified(20);       // For I2C wiring
/* Assign a unique ID to the sensors */
Adafruit_10DOF                dof   = Adafruit_10DOF();
Adafruit_LSM303_Accel_Unified accel = Adafruit_LSM303_Accel_Unified(30301);
Adafruit_LSM303_Mag_Unified   mag   = Adafruit_LSM303_Mag_Unified(30302);

// Make sure these two variables are correct for your setup
int scale = 200; // 200 (±200g) for ADXL377
const int sampleSize = 100;  // For initial average read

const int xAxis = A0;
const int yAxis = A1;
const int zAxis = A2;
const int xAxis2 = A8;
const int yAxis2 = A9;
const int zAxis2 = A10;

int AvgRawData[6];              // For initial average read

int rawX;
int rawY;
int rawZ;
int rawX2;
int rawY2;
int rawZ2;
float XhighG,  YhighG,  ZhighG,  X2highG,  Y2highG,  Z2highG; // Scaled values for each axis
float preXhighG, preYhighG, preZhighG, preX2highG, preY2highG, preZ2highG;
const int upperTrig = 3;   //gs
```

```
const int lowerTrig = -3;   //gs
int printPause;
boolean printed = false;

int n = 0;
float myArrayX[200];
float myArrayY[200];
float myArrayZ[200];
float myArrayX2[200];
float myArrayY2[200];
float myArrayZ2[200];
float myArrayT[200];

//unsigned long microBegin;
unsigned long preMicroTime;
unsigned long microTime;
unsigned long milliTime;
unsigned long releaseTime;
unsigned long releaseCheck;
unsigned long startTime;
unsigned long endTime = 150000; //Microseconds
unsigned long timeCheck;
boolean Release = false;
boolean impact = false;

// Light and Button
const int buttonPin = 2;
const int buttonPower = 11;
const int ledPin = 12;
int buttonState = 0;
boolean ledOff = false;

// defines for setting and clearing register bits
#ifndef cbi
#define cbi(sfr, bit) (_SFR_BYTE(sfr) &= ~_BV(bit))
#endif
#ifndef sbi
#define sbi(sfr, bit) (_SFR_BYTE(sfr) |= _BV(bit))
#endif

void initSensors()
{
  if (!gyro.begin(GYRO_RANGE_2000DPS))
```

```
  {
    Serial.println(F("No L3GD20 detected ... Check wiring!"));
    while (1);
  }
  // Initialise the accelerometer
  if(!accel.begin())
  {
    // There was a problem detecting the ADXL345 ... check your connections
    Serial.println(F("No LSM303 detected ... Check wiring!"));
    while(1);
  }
  if(!mag.begin())
  {
    /* There was a problem detecting the LSM303 ... check your connections */
    Serial.println(F("No LSM303 detected ... Check wiring!"));
    while(1);
  }
}

void setup()
{
  pinMode(ledPin, OUTPUT);
  pinMode(buttonPower, OUTPUT);
  pinMode(buttonPin, INPUT);
  digitalWrite(buttonPower, HIGH);

  // set prescale to 16 for increasing analogRead to ~77KHz from previously 9.6KHz
  sbi(ADCSRA,ADPS2) ;
  cbi(ADCSRA,ADPS1) ;
  cbi(ADCSRA,ADPS0) ;

  TWBR = ((F_CPU /400000l) - 16) / 2; // Change the i2c clock to 400KHz
  analogReference(EXTERNAL);          //  Reference 3V for high-G sensors
  // Initialize serial communication at 250000 baud
  Serial.begin(250000);
  /* Initialise the sensors */
  initSensors();
  delay(100);

  sensors_event_t accel_event;
  sensors_event_t mag_event;
  sensors_event_t gyro_event;
  sensors_vec_t orientation;
```

```
milliTime = millis();
// Read the sensors
accel.getEvent(&accel_event);
mag.getEvent(&mag_event);
gyro.getEvent(&gyro_event);

/* Use the new fusionGetOrientation function to merge accel(m/s^2)/mag data. Also get gyro(deg/s) */
if (dof.fusionGetOrientation(&accel_event, &mag_event, &orientation))
{
  Serial.print(F("ACCEL: ")); Serial.print(accel_event.acceleration.x); Serial.print(F(", "));
  Serial.print(accel_event.acceleration.y); Serial.print(F(", "));
  Serial.print(accel_event.acceleration.z); Serial.print(F(", "));
  Serial.print(F("GYRO: ")); Serial.print(gyro_event.gyro.x); Serial.print(F(", "));
  Serial.print(gyro_event.gyro.y); Serial.print(F(", "));
  Serial.print(gyro_event.gyro.z); Serial.print(F(", "));
  /* 'orientation' should have valid .roll and .pitch fields */
  Serial.print(F("Orientation: ")); Serial.print(orientation.roll); Serial.print(F(", "));
  Serial.print(orientation.pitch); Serial.print(F(", "));
  Serial.print(orientation.heading); Serial.print(F(", "));
  Serial.print(F("Time: ")); Serial.println(milliTime);
}

int startAvgRead = millis();
ReadAxes(AvgRawData);
int endAvgRead = millis();
int AvgTime = endAvgRead - startAvgRead;
int AvgRawX = AvgRawData[0];
int AvgRawY = AvgRawData[1];
int AvgRawZ = AvgRawData[2];
int AvgRawX2 = AvgRawData[3];
int AvgRawY2 = AvgRawData[4];
int AvgRawZ2 = AvgRawData[5];
XhighG = mapf(AvgRawX, 0, 1023, -scale, scale);
YhighG = mapf(AvgRawY, 0, 1023, -scale, scale);
ZhighG = mapf(AvgRawZ, 0, 1023, -scale, scale);
X2highG = mapf(AvgRawX2, 0, 1023, -scale, scale);
Y2highG = mapf(AvgRawY2, 0, 1023, -scale, scale);
Z2highG = mapf(AvgRawZ2, 0, 1023, -scale, scale);
Serial.print(F("HighG1: ")); Serial.print(XhighG); Serial.print(F(", "));
Serial.print(YhighG); Serial.print(F(", "));
Serial.print(ZhighG); Serial.print(F(", "));
Serial.print(F("HighG2: ")); Serial.print(X2highG); Serial.print(F(", "));
```

```
    Serial.print(Y2highG); Serial.print(F(", "));
    Serial.print(Z2highG); Serial.print(F(", "));
    Serial.print(F("Read Time: ")); Serial.print(AvgTime); Serial.println(F("ms"));
    delay(1000);
    releaseTime = millis();
}


// Read, scale, and print accelerometer data
void loop()
{
  while(Release == false)
  {
    releaseTime = millis();
    buttonState = digitalRead(buttonPin);
    if(buttonState == HIGH)
    {
      digitalWrite(ledPin, HIGH);
      Serial.print(F("Release Time: ")); Serial.println(releaseTime);
      releaseCheck = millis();
      Release = true;
    }
  }

  while(Release == true && releaseCheck-releaseTime <= 100)
  {
    sensors_event_t accel_event;
    sensors_event_t gyro_event;

    milliTime = millis();
    // Read the sensors
    accel.getEvent(&accel_event);
    gyro.getEvent(&gyro_event);

    Serial.print(F("ACCEL: ")); Serial.print(accel_event.acceleration.x); Serial.print(F(", "));
    Serial.print(accel_event.acceleration.y); Serial.print(F(", "));
    Serial.print(accel_event.acceleration.z); Serial.print(F(", "));
    Serial.print(F("GYRO: ")); Serial.print(gyro_event.gyro.x); Serial.print(F(", "));
    Serial.print(gyro_event.gyro.y); Serial.print(F(", "));
    Serial.print(gyro_event.gyro.z); Serial.print(F(", "));
    Serial.print(F("TIME: ")); Serial.println(milliTime);
    releaseCheck = millis();
  }
```

```cpp
if(Release == true && ledOff == false)
{
  digitalWrite(ledPin, LOW);
  ledOff = true;
}

// Get raw accelerometer data for each axis
microTime = micros();
rawX = analogRead(xAxis);
rawY = analogRead(yAxis);
rawZ = analogRead(zAxis);
rawX2 = analogRead(xAxis2);
rawY2 = analogRead(yAxis2);
rawZ2 = analogRead(zAxis2);

XhighG = mapf(rawX, 0, 1023, -scale, scale);
YhighG = mapf(rawY, 0, 1023, -scale, scale);
ZhighG = mapf(rawZ, 0, 1023, -scale, scale);
X2highG = mapf(rawX2, 0, 1023, -scale, scale);
Y2highG = mapf(rawY2, 0, 1023, -scale, scale);
Z2highG = mapf(rawZ2, 0, 1023, -scale, scale);

if((impact == false && ZhighG >= upperTrig || impact == false && ZhighG <= lowerTrig || impact == false && Z2highG >= upperTrig || impact == false && Z2highG <= lowerTrig)
{
  digitalWrite(ledPin, HIGH);
  startTime = microTime;
  timeCheck = startTime;
  impact = true;
}
else if(impact == false)
{
  preMicroTime = microTime;
  preXhighG = XhighG;
  preYhighG = YhighG;
  preZhighG = ZhighG;
  preX2highG = X2highG;
  preY2highG = Y2highG;
  preZ2highG = Z2highG;
}

if(impact == true && timeCheck-startTime <= endTime && n < 200)
{
  myArrayX[n] = XhighG;
```

```
      myArrayY[n] = YhighG;
      myArrayZ[n] = ZhighG;
      myArrayX2[n] = X2highG;
      myArrayY2[n] = Y2highG;
      myArrayZ2[n] = Z2highG;
      myArrayT[n] = microTime;
      n = n+1;
    }
    timeCheck = micros();

    if(impact == true && printed == false && timeCheck-startTime > endTime)
    {
      // Print out scaled X,Y,Z accelerometer readings
      Serial.print(preXhighG); Serial.print(F(", "));
      Serial.print(preYhighG); Serial.print(F(", "));
      Serial.print(preZhighG); Serial.print(F(", "));
      Serial.print(preX2highG); Serial.print(F(", "));
      Serial.print(preY2highG); Serial.print(F(", "));
      Serial.print(preZ2highG); Serial.print(F(", "));
      Serial.println(preMicroTime);

      for(int i=0;i<n;i++)
      {
        Serial.print(myArrayX[i]); Serial.print(F(", "));
        Serial.print(myArrayY[i]); Serial.print(F(", "));
        Serial.print(myArrayZ[i]); Serial.print(F(", "));
        Serial.print(myArrayX2[i]); Serial.print(F(", "));
        Serial.print(myArrayY2[i]); Serial.print(F(", "));
        Serial.print(myArrayZ2[i]); Serial.print(F(", "));
        Serial.println(myArrayT[i]);
      }
      printed = true;
      digitalWrite(ledPin, LOW);
    }
}

// Same functionality as Arduino's standard map function, except using floats
float mapf(float x, float in_min, float in_max, float out_min, float out_max)
{
  return (x - in_min) * (out_max - out_min) / (in_max - in_min) + out_min;
}
```

```cpp
// Read "sampleSize" samples and report the average
int ReadAxes(int pAvgRawData[])
{
  unsigned int readingX = 0;
  unsigned int readingY = 0;
  unsigned int readingZ = 0;
  unsigned int readingX2 = 0;
  unsigned int readingY2 = 0;
  unsigned int readingZ2 = 0;

  for (int i = 0; i < sampleSize; i++)
  {
    readingX += analogRead(xAxis);
    readingY += analogRead(yAxis);
    readingZ += analogRead(zAxis);
    readingX2 += analogRead(xAxis2);
    readingY2 += analogRead(yAxis2);
    readingZ2 += analogRead(zAxis2);
    delay(1);
  }
  pAvgRawData[0] = readingX/sampleSize;
  pAvgRawData[1] = readingY/sampleSize;
  pAvgRawData[2] = readingZ/sampleSize;
  pAvgRawData[3] = readingX2/sampleSize;
  pAvgRawData[4] = readingY2/sampleSize;
  pAvgRawData[5] = readingZ2/sampleSize;
}
```

9.2 Arduino Mega Specifications [56]

Schematic: arduino-mega2560-schematic.pdf

Summary

Microcontroller	ATmega2560
Operating Voltage	5V
Input Voltage (recommended)	7-12V
Input Voltage (limits)	6-20V
Digital I/O Pins	54 (of which 14 provide PWM output)
Analog Input Pins	16
DC Current per I/O Pin	40 mA
DC Current for 3.3V Pin	50 mA
Flash Memory	256 KB of which 8 KB used by bootloader
SRAM	8 KB
EEPROM	4 KB
Clock Speed	16 MHz

Power

The Arduino Mega can be powered via the USB connection or with an external power supply. The power source is selected automatically.

External (non-USB) power can come either from an AC-to-DC adapter (wall-wart) or battery. The adapter can be connected by plugging a 2.1mm center-positive plug into the board's power jack. Leads from a battery can be inserted in the Gnd and Vin pin headers of the POWER connector.

The board can operate on an external supply of 6 to 20 volts. If supplied with less than 7V, however, the 5V pin may supply less than five volts and the board may be unstable. If using more than 12V, the voltage regulator may overheat and damage the board. The recommended range is 7 to 12 volts.

The Mega2560 differs from all preceding boards in that it does not use the FTDI USB-to-serial driver chip. Instead, it features the Atmega8U2 programmed as a USB-to-serial converter.

9.3 Adafruit 10 DOF Breakout Board Specifications [57]

Introduction
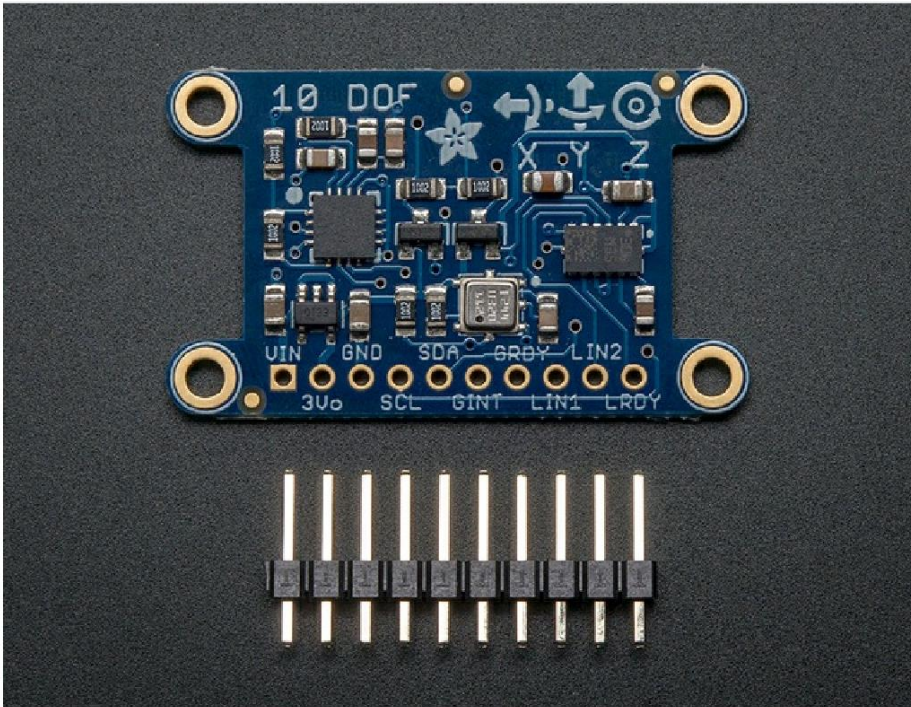
Please note that there is a small cosmetic error on the first revision of these boards (shown above). The straight X arrow for the accelerometer should be pointing in the opposite direction, towards the right. This will be fixed in the net run of these boards.

Adafruit's 10DOF (10 Degrees of Freedom) breakout board allows you to capture ten (err, eleven!) distinct types of motion or orientation related data.

After testing a lot of combinations of sensors, we settled on the following devices that we think offer the best results and the least amount of hassle:

- **LSM303DLHC** - a **3-axis accelerometer** (up to +/-16g) and a **3-axis magnetometer** (up to +/-8.1 gauss) on a single die
- **L3GD20** - a **3-axis gyroscope** (up to +/-2000 dps)
- **BMP180** - A **barometric pressure sensor** (300..1100 hPa) that can be used to calculate altitude, with an additional on-board **temperature sensor**

LSM303DLHC

Ultra compact high performance e-compass 3D accelerometer and 3D magnetometer module

Preliminary data

Features

- 3 magnetic field channels and 3 acceleration channels
- From ±1.3 to ±8.1 gauss magnetic field full-scale
- ±2g/±4g/±8g/±16g selectable full-scale
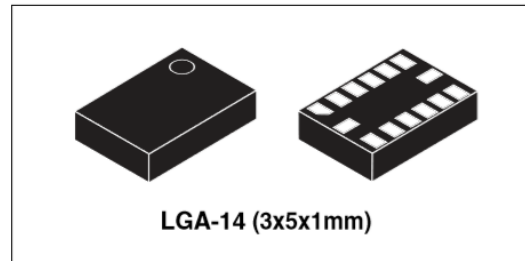- 16 bit data output
- I^2C serial interface
- Analog supply voltage 2.16 V to 3.6 V
- Power-down mode/ low-power mode
- 2 independent programmable interrupt generators for free-fall and motion detection
- Embedded temperature sensor
- Embedded FIFO
- 6D/4D orientation detection
- ECOPACK® RoHS and "Green" compliant

Applications

- Compensated compass
- Map rotation
- Position detection
- Motion-activated functions
- Free-fall detection
- Click/double click recognition
- Pedometer
- Intelligent power-saving for handheld devices
- Display orientation
- Gaming and virtual reality input devices
- Impact recognition and logging
- Vibration monitoring and compensation

LGA-14 (3x5x1mm)

Description

The LSM303DLHC is a system-in-package featuring a 3D digital linear acceleration sensor and a 3D digital magnetic sensor.

LSM303DLHC has linear acceleration full-scales of ±2*g* / ±4*g* / ±8*g* / ±16*g* and a magnetic field full-scale of ±1.3 / ±1.9 / ±2.5 / ±4.0 / ±4.7 / ±5.6 / ±8.1 gauss. All full-scales available are fully selectable by the user.

LSM303DLHC includes an I^2C serial bus interface that supports standard and fast mode 100 kHz and 400kHz. The system can be configured to generate interrupt signals by inertial wake-up/free-fall events as well as by the position of the device itself. Thresholds and timing of interrupt generators are programmable by the end user on the fly. Magnetic and accelerometer parts can be enabled or put into power-down mode separately.

The LSM303DLHC is available in a plastic land grid array package (LGA) and is guaranteed to operate over an extended temperature range from -40 °C to +85 °C.

Table 1.   Device summary

Part number	Temperature range [°C]	Package	Packing
LSM303DLHC	-40 to +85	LGA-14	Tray
LSM303DLHCTR	-40 to +85	LGA-14	Tape and reel

April 2011

Doc ID 018771 Rev 1

1/42

This is preliminary information on a new product now in development or undergoing evaluation. Details are subject to change without notice.

www.st.com

L3GD20

MEMS motion sensor: three-axis digital output gyroscope

Features

- Three selectable full scales (250/500/2000 dps)
- I^2C/SPI digital output interface
- 16 bit-rate value data output
- 8-bit temperature data output
- Two digital output lines (interrupt and data ready)
- Integrated low- and high-pass filters with user-selectable bandwidth
- Wide supply voltage: 2.4 V to 3.6 V
- Low voltage-compatible IOs (1.8 V)
- Embedded power-down and sleep mode
- Embedded temperature sensor
- Embedded FIFO
- High shock survivability
- Extended operating temperature range (-40 °C to +85 °C)
- ECOPACK® RoHS and "Green" compliant

Applications

- Gaming and virtual reality input devices
- Motion control with MMI (man-machine interface)
- GPS navigation systems
- Appliances and robotics

LGA-16 (4x4x1 mm)
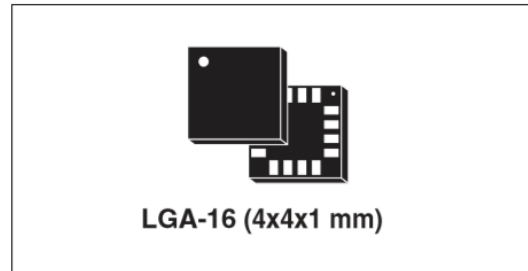
Description

The L3GD20 is a low-power three-axis angular rate sensor.

It includes a sensing element and an IC interface capable of providing the measured angular rate to the external world through a digital interface (I^2C/SPI).

The sensing element is manufactured using a dedicated micro-machining process developed by STMicroelectronics to produce inertial sensors and actuators on silicon wafers.

The IC interface is manufactured using a CMOS process that allows a high level of integration to design a dedicated circuit which is trimmed to better match the sensing element characteristics.

The L3GD20 has a full scale of ±250/±500/ ±2000 dps and is capable of measuring rates with a user-selectable bandwidth.

The L3GD20 is available in a plastic land grid array (LGA) package and can operate within a temperature range of -40 °C to +85 °C.

Table 1. Device summary

Order code	Temperature range (°C)	Package	Packing
L3GD20	-40 to +85	LGA-16 (4x4x1 mm)	Tray
L3GD20TR	-40 to +85	LGA-16 (4x4x1 mm)	Tape and reel

1. Electrical characteristics

If not stated otherwise, the given values are ±3-Sigma values over temperature/voltage range in the given operation mode. All values represent the new parts specification; additional solder drift is shown separately.

Table 1: Operating conditions, output signal and mechanical characteristics

Parameter	Symbol	Condition	Min	Typ	Max	Units
Operating temperature	T_A	operational	-40		+85	°C
		full accuracy	0		+65	
Supply voltage	V_{DD}	ripple max. 50mVpp	1.8	2.5	3.6	V
			1.62	2.5	3.6	
Supply current @ 1 sample / sec. 25°C	I_{DDLOW}	ultra low power mode		3		µA
	I_{DDSTD}	standard mode		5		µA
	I_{DDHR}	high resolution mode		7		µA
	I_{DDUHR}	Ultra high res. mode		12		µA
	I_{DDAR}	Advanced res. mode		32		µA
Peak current	I_{peak}	during conversion		650	1000	µA
Standby current	I_{DDSBM}	@ 25°C		0.1	4^1	µA
Relative accuracy pressure V_{DD} = 3.3V		950 . . . 1050 hPa @ 25 °C		±0.12		hPa
				±1.0		m
		700 ... 900hPa 25 . . . 40 °C		±0.12		hPa
				±1.0		m
Absolute accuracy pressure V_{DD} = 3.3V		300 . . . 1100 hPa 0 . . . +65 °C	-4.0	-1.0*	+2.0	hPa
		300 . . . 1100 hPa -20 . . . 0 °C	-6.0	-1.0*	+4.5	hPa
Resolution of output data		pressure		0.01		hPa
		temperature		0.1		°C
Noise in pressure		see table on page 12-13				
Absolute accuracy temperature V_{DD} = 3.3V		@ 25 °C	-1.5	±0.5	+1.5	°C
		0 . . . +65 °C	-2.0	±1.0	+2.0	°C

ANALOG DEVICES

Small, Low Power, 3-Axis ±200 *g* Accelerometer

Data Sheet

ADXL377

FEATURES

3-axis sensing
Small, low profile package
  3 mm × 3 mm × 1.45 mm LFCSP
Low power: 300 μA (typical)
Single-supply operation: 1.8 V to 3.6 V
10,000 *g* shock survival
Excellent temperature stability
Bandwidth adjustment with a single capacitor per axis
RoHS/WEEE and lead-free compliant

APPLICATIONS

Concussion and head trauma detection
High force event detection

GENERAL DESCRIPTION

The ADXL377 is a small, thin, low power, complete 3-axis accelerometer with signal conditioned voltage outputs. The ADXL377 measures acceleration resulting from motion, shock, or vibration with a typical full-scale range of ±200 *g*.

The user selects the bandwidth of the accelerometer using the C_X, C_Y, and C_Z capacitors at the X_{OUT}, Y_{OUT}, and Z_{OUT} pins. Bandwidths can be selected to suit the application, with a range of 0.5 Hz to 1300 Hz for the x-axis and y-axis and a range of 0.5 Hz to 1000 Hz for the z-axis.

The ADXL377 is available in a small, low profile, 3 mm × 3 mm × 1.45 mm, 16-lead lead frame chip scale package (LFCSP_LQ).
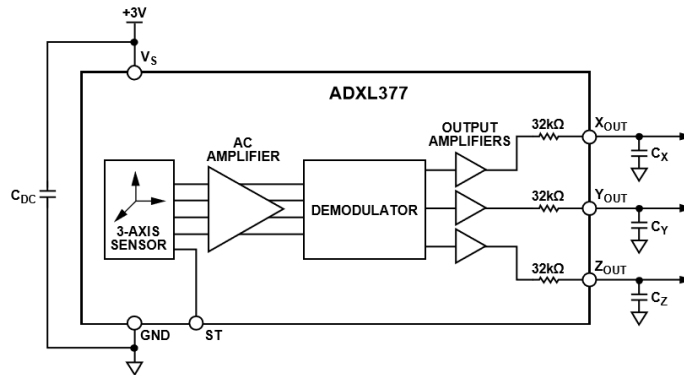
FUNCTIONAL BLOCK DIAGRAM

Figure 1.

SPECIFICATIONS

T_A = 25°C, V_S = 3 V, C_X = C_Y = C_Z = 0.1 μF, acceleration = 0 g, unless otherwise noted. All minimum and maximum specifications are guaranteed. Typical specifications are not guaranteed.

Table 1.

Parameter	Test Conditions/Comments	Min	Typ	Max	Unit
SENSOR INPUT	Each axis				
Measurement Range			±200		g
Nonlinearity	% of full scale up to 180 g		±0.5		%
Cross-Axis Sensitivity[1]			±1.4		%
SENSITIVITY, RATIOMETRIC[2]	Each axis				
Sensitivity at X_{OUT}, Y_{OUT}, and Z_{OUT}	V_S = 3 V	5.8	6.5	7.2	mV/g
Sensitivity Change Due to Temperature[3]	V_S = 3 V		±0.02		%/°C
ZERO g BIAS LEVEL, RATIOMETRIC					
Zero g Voltage	V_S = 3 V, T_A = 25°C	1.4	1.5	1.6	V
Zero g Offset vs. Temperature					
X-Axis and Y-Axis			±12		mg/°C
Z-Axis			±30		mg/°C
NOISE PERFORMANCE					
Noise Density					
X_{OUT} and Y_{OUT}			2.7		mg/√Hz
Z_{OUT}			4.3		mg/√Hz
FREQUENCY RESPONSE[4]					
Bandwidth[5]	No external filter				
X_{OUT} and Y_{OUT}			1300		Hz
Z_{OUT}			1000		Hz
R_{FILT} Tolerance			32 ± 15%		kΩ
Sensor Resonant Frequency			16.5		kHz
SELF-TEST[6]					
Logic Input Low			0.6		V
Logic Input High			2.4		V
ST Actuation Current			60		μA
Output Change	Self-test, 0 to 1				
At X_{OUT}			−6.5		mV
At Y_{OUT}			6.5		mV
At Z_{OUT}			11.5		mV
OUTPUT AMPLIFIER	No load				
Output Swing Low			0.1		V
Output Swing High			2.8		V
POWER SUPPLY					
Operating Voltage Range[7]		1.8	3.0	3.6	V
Supply Current	V_S = 3 V		300		μA
Turn-On Time[8]	No external filter		1		ms
OPERATING TEMPERATURE RANGE		−40		+85	°C

[1] Defined as coupling between any two axes.
[2] Sensitivity is essentially ratiometric to V_S.
[3] Defined as the output change from ambient temperature to maximum temperature or from ambient temperature to minimum temperature.
[4] Actual frequency response controlled by user-supplied external filter capacitors (C_X, C_Y, and C_Z).
[5] Bandwidth with external capacitors = $1/(2\pi \times 32 \text{ k}\Omega \times C_X)$.
[6] Self-test response changes cubically with V_S.
[7] Tested at 3.0 V and guaranteed by design only (not tested) to work over the full voltage range from 1.8 V to 3.6 V.
[8] Turn-on time is dependent on C_X, C_Y, and C_Z and is approximately 160 × (C_X or C_Y or C_Z) + 1, where C_X, C_Y, and C_Z are in μF and the resulting turn-on time is in ms.

10 References

[1]   Alliance of Automobile Manufacturers, "Cars Move America," 2016.

[2]   M. Kleinberger, E. Sun, R. Eppinger , S. Kuppa and R. Saul, "Development of Improved Injury Criteria for the Assessment of Advanced Automotive Restraint Systems," National Highway Traffic Safety Administration, 1998.

[3]   S. N. Narkhede, "Analysis of Pedestrian Collision with a Pickup Truck," Wichita State University, Wichita, 2007.

[4]   K.-U. Schmitt, P. F. Niederer, M. H. Muser and F. Walz, Trauma Biomechanics - Accidental Injury in Traffic and Sports, Heidelberg Dordrecht London New York: Springer, 2010.

[5]   R. L. Huston, Principles of Biomechanics, Boca Raton, FL: Taylor & Francis Group , 2009.

[6]   National Highway Traffic Safety Administration, "Hybrid III 50th Percentile Male," U.S. Department of Transportation, [Online]. Available: http://www.nhtsa.gov/Research/Vehicle+Research+&+Testing+(VRTC)/Hybrid+III+50th+Percentile+Male. [Accessed July 2016].

[7]   Aerospace Specification Metals Inc., "AISI Type 304 Stainless Steel," MatWeb, LLC, [Online]. Available: http://asm.matweb.com/search/SpecificMaterial.asp?bassnum=MQ304A. [Accessed 2016].

[8]   Aerospace Specification Metals Inc., "Aluminum 7075-T6; 7075-T651," MatWeb, LLC, [Online]. Available: http://asm.matweb.com/search/SpecificMaterial.asp?bassnum=ma7075t6. [Accessed 2016].

[9]   Aerospace Specification Metals Inc., "Aluminum 6061-T6; 6061-T651," MatWeb, LLC, [Online]. Available: http://asm.matweb.com/search/SpecificMaterial.asp?bassnum=MA6061t6. [Accessed 2016].

[10]   McMaster-Carr, "Hard High-Strength 7075 Aluminum," McMaster-Carr, 2016. [Online]. Available: http://www.mcmaster.com/#9055k21/=13vbalb. [Accessed 2016].

[11]   McMaster-Carr, "Multipurpose 304/304L Stainless Steel Rod," McMaster-Carr, 2016. [Online]. Available: http://www.mcmaster.com/#89535k11/=13vb1tu. [Accessed 2016].

[12]   Hovding, "How It Works," 2016. [Online]. Available: http://www.hovding.com/how-hovding-works. [Accessed July 2016].

[13]   Helite Moto, "Technology," 2016. [Online]. Available: http://www.helitemoto.com/pages.php?pageid=5. [Accessed July 2016].

[14] P. Venkatraman and D. Tyler, "A Critical Review of Impact Resistant Materials Using in Sportswear Clothing," Manchester Metropolitan University, Manchester, UK , 2012.

[15] Moditech Rescue Solutions, "Pedestrian Protection Airbag," May 2012. [Online]. Available: http://moditech.com/en/pedestrian-protection-airbag. [Accessed July 2016].

[16] National Center for Statistics and Analysis, "Bicyclists and Other Cyclists: 2013 Data," National Highway Traffic Safety Administration, Washington, DC, 2015.

[17] National Center for Statistics and Analysis, "Pedestrians: 2013 Data," National Highway Traffic Safety Administration, Washington, DC, 2015.

[18] K. Mizuno and J. Kajzer, "Compatibility Problems in Frontal, Side, Single Car Collisions and Car-to-Pedestrian Accidents in Japan," *Accident Analysis and Prevention 31,* pp. 381-391, 1999.

[19] B. S. Roudsari, C. N. Mock, R. Kaufman, D. Grossman, B. Y. Henary and J. Crandall, "Pedestrian Crashes: Higher Injury Severity and Mortality Rate for Light Truck Vehicles Compared with Passenger Vehicles," *Injury Prevention,* vol. 10, pp. 154-158, 2004.

[20] B. C. Tefft, "Impact Speed and a Pedestrian's Risk of Severe Injury or Death," AAA Foundation for Traffic Safety, Washinton, DC, 2001.

[21] M. Stone and J. Broughton, "Getting Off Your Bike: Cycling Accidents in Great Britain in 1990-1999," *Accident Analysis and Prevention 35,* pp. 549-556, 2003.

[22] C. Simms and D. Wood, Pedestrian and Cyclist Impact: A Biomechanical Perspective, Springer Dordrecht Heidelberg London New York: Springer, 2009.

[23] National Association of Emergency Medical Technicians (U.S.). Pre-Hospital Trauma Life Support Committee.; American College of Surgeons. Committee on Trauma, "Kinematics of Trauma," in *PHTLS: Prehospital Trauma Life Support*, St. Louis, MO, Elsevier Mosby, 2007, pp. 43-85.

[24] C. R. '. Bass, K. A. Rafaels, R. S. Salzar, M. Carboni, R. W. Kent, M. D. Lloyd, S. Lucas, K. Meyerhoff, C. Planchak, A. Damon and G. T. Bass, "Thoracic and Lumbar Spinal Impact Tolerance," *Accident Analysis and Prevention 40,* pp. 487-495, November 2008.

[25] N. A. Vavalle, D. P. Moreno, A. C. Rhyne, J. D. Stitzel and F. S. Gayzik, "Lateral Impact Validation of a Geometrically Accurate Full Body Finite Element Model for Blunt Injury Prediction," *Annal of Biomedical Engineering,* vol. 41, pp. 497-512, March 2013.

[26] G. Zhang, L. Cao, J. Hu and K. H. Yang, "A Field Data Analysis of Risk Factors Affecting the Injury Risks in Vehicle-to-Pedestrian Crashes," *Annals of Advances in Automotive Medicine,* November 2008.

[27] A. ". B. Chidester and R. A. Isenberg, "Final Report - The Pedestrian Crash Data Study," National Highway Traffic Safety Administration, 2001.

[28] R. Fredriksson, P.-O. Bylund and M. Oman, "Fatal Vehicle-to-Bicyclist Crashes in Sweden - an In-Depth Study of Injuries and Vehicle Sources," *Annals of Advances in Automotive Medicine,* vol. 56, pp. 25-30, October 2012.

[29] Y. Han, J. Yang, K. Mizuno and Y. Matsui, "Effects of Vehicle Impact Velocity, Vehicle Front-End Shapes on Pedestrian Injury Risk," *Traffic Injury Prevention,* vol. 13, pp. 507-518, Semptember 2012.

[30] F. A. Pintar, N. Yoganandan, M. H. Hines, M. R. Maltese, J. McFadden, R. Saul, R. Eppinger, N. Khaewpong and M. Kleinberger, "Chestband Analysis of Human Tolerance to Side Impact," *Stapp Car Crash J.,* pp. 41:63-74, 1997.

[31] J. M. Cavanaugh, T. J. Walilko, A. Malhotra, Y. Zhu and A. I. King, "Biomechanical Response and Injury Tolerance of the Thorax in Twelve Sled Side Impacts," SAE, 1990.

[32] R. Stalnaker, C. Tarriere, A. Fayon, G. Walfisch, M. Balthazard, J. Masset, C. Got and A. Patel, "Modification of Part 572 Dummy for Lateral Impact According to Biomechanical Data," *Stapp Car Crash J.,* pp. 23:843-872, 1979.

[33] Y. Liu, "Impact Experimental Analysis and Computer Simulation," University of Louisville, Louisville, 2006.

[34] J. Ding, P. Tracey, W. Li, G. Peng, P. G. Whitten and G. G. Wallace, "Review on Shear Thickening Fluids and Applications," *Textiles and Light Industrial Science and Technology (TLIST),* vol. 2, no. 4, pp. 161-173, 2013.

[35] J. Ma, "Back Protection Concept Design Research," Chalmers University of Technology, Goteborg, 2012.

[36] J. Berns, "Spinal and Back Protection System". United States of America Patent US 6687920 B2, 10 February 2004.

[37] L. Dainese, "Back Protector, in Particular for Motorcyclists". United States of America Patent US 6852087 B1, 8 February 2005.

[38] G. Mazzarolo, "Freely Jointed Arrangement for Protecting the Back Against Bumps". United States of America Patent US 7329230 B2, 12 February 2008.

[39] L. R. Bowlus, H. M. Bowlus and J. B. Szender, "Wearable Spinal Protective Apparatus". United States of America Patent US 8074294 B2, 13 December 2011.

[40] G. Reay, "Flexible Protective Armor". United States of America Patent US 2012/0198594 A1, 9 August 2012.

[41] D3O Lab, "How D3O Technology Works," D3O Lab, [Online]. Available: http://www.d3o.com/materials/how-d3o-technology-works/. [Accessed June 2016].

[42] D3O Lab, LLC, "D3O TV," [Online]. Available: http://www.d3o.com/d3o-videos/.

[43] G. D. Piero and G. Pampolini, "On the Rate-Dependent Properties of Open-Cell Polyurethane Foams," *Technische Mechanik,* pp. 74-84, 2010.

[44] Rogers Corporation, "Embrace The Power," 2011. [Online]. Available: http://www.xrd.tech/howitworks/index.aspx.

[45] SATRA Technology Centre, "Motorcylce Protection," SATRA Technology Centre, 2014. [Online]. Available: http://www.satrappeguide.com/EN1621.php. [Accessed August 2016].

[46] C. Elliott, "Viper Pro," D3O Lab, 2017. [Online]. Available: https://www.d3o.com/products/viper-pro/. [Accessed 2017].

[47] MatWeb Material Property Data, "304 Stainless Steel (UNS S30400); Annealed and Cold Worked Bar, 5/8" (16 mm) Diameter," MatWeb, LLC., [Online]. Available: http://www.matweb.com/search/DataSheet.aspx?MatGUID=fd16d11a61f8402c86ea74d2252c1385. [Accessed 2018].

[48] American Academy of Orthopaedic Surgeons, "Spine Basics," American Academy of Orthopaedic Surgeons, December 2013. [Online]. Available: http://orthoinfo.aaos.org/topic.cfm?topic=A00575.

[49] R. K., "webBikeWorld," webWorld International, LLC, January 2016. [Online]. Available: http://www.webbikeworld.com/r5/helite-adventure-airbag-jacket-review/. [Accessed 14 March 2017].

[50] M. M. Panjabi, J. N. Hausfeld and A. A. White, "A Biomechanical Study of the Ligamentous Stability of the Thoracic Spine in Man," *Acta Orthopaedica Scandinavica,* vol. 52, no. 3, pp. 315-326, 1981.

[51] D. Morita, Y. Yukawa, H. Nakashima, K. Ito, G. Yoshida, M. Machino, S. Kanbara, T. Iwase and F. Kato, "Range of Motion of Thoracic Spine in Sagittal Plane," *Ueropean Spine Journal,* vol. 23, no. 3, pp. 673-678, Mar 2014.

[52] J. M. Gere and B. J. Goodno, Mechanics of Materials, Seventh Edition ed., Toronto: Cengage Learning, 2009.

[53] E. Oberg, F. D. Jones, H. L. Horton and H. H. Ryffel, Machinery's Handbook 26th Edition, New York: Industrial Press Inc., 2000.

[54] Packaging Compliance Labs, LLC, *4334 Brockton Dr. SE Suite E, Kentwood, MI 49512.*

[55] Wikipedia, "Coefficient of Restitution," Wikimedia Foundation, Inc., July 2016. [Online]. Available: https://en.wikipedia.org/wiki/Coefficient_of_restitution.

[56]   RobotShop Inc., "Arduino Mega 2560 Datasheet," 2018. [Online]. Available: https://www.robotshop.com/media/files/pdf/arduinomega2560datasheet.pdf. [Accessed 2018].

[57]   K. Townsend, "Adafruit 10-DOF IMU Breakout," 22 August 2018. [Online]. Available: https://cdn-learn.adafruit.com/downloads/pdf/adafruit-10-dof-imu-breakout-lsm303-l3gd20-bmp180.pdf. [Accessed 2018].

[58]   Analog Devices Inc., "Data Sheet ADXL377," September 2018. [Online]. Available: https://www.analog.com/media/en/technical-documentation/data-sheets/adxl377.pdf. [Accessed 2018].

[59]   R. Watanabe, T. Katsuhara, H. Miyazaki, Y. Kitagawa and T. Yasuki, "Research of the Relationship of Pedestrian Injury to Collision Speed, Car-type, Impact Location and Pedestrian Sizes using Human FE model (THUMS Version 4)," *Stapp Car Crash Journal,* vol. 56, pp. 269-321, October 2012.

[60]   P. Schroeder and M. Wilbur, "2012 National survey of bicyclist and pedestrian attitudes and behavior, volume 2: Findings report," National Highway Traffic Safety Administration, Washington, DC, 2013, October.

[61]   C. K. Simms and D. P. Wood, "Pedestrian Risk from Cars and Sport Utility Vehicles - A Comparative Analytical Study," *Proc. IMechE Vol. 220 Part D: J. Automobile Engineering,* pp. 1085-1100, 2006.

[62]   M. F. Ballestros, P. C. Dischinger and P. Langenberg, "Pedestrian injuries and vehicle type in Maryland, 1995–1999," *Accident Analysis and Prevention 36,* pp. 73-81, 2004.

[63]   D. C. Viano and C. S. Parenteau, "Analysis of Head Impacts Causing Neck Compression Injury," *Traffic Injury Prevention,* vol. 9, no. 2, pp. 144-152, 2008.

[64]   H. Gray, Anatomy of the Human Body, 20 ed., Philadelphia: Lea & Febiger, 1918.

[65]   Midway Machine Technologies, *555 North State Street, Zeeland, MI 49464.*